SAPIENZA
UNIVERSITÀ DI ROMA

3D microstructures for active and soft matter studies

Scuola di dottorato Vito Volterra

Dottorato di Ricerca in Fisica – XXXIII Ciclo

Candidate

Viridiana Carmona Sosa
ID number 1798062

Thesis Advisor

Prof. Roberto Di Leonardo

A thesis submitted in partial fulfillment of the requirements
for the degree of Doctor of Philosophy in Physics
10 June 2021

Thesis defended on the 6th of July 2021
in front of a Board of Examiners composed by:

Prof. Stefano Lupi (chairman)

Prof. Dario Gerace

Prof. Miriam Vitiello

3D microstructures for active and soft matter studies
Ph.D. thesis. Sapienza – University of Rome
ISBN: 000000000-0
© 2021 Viridiana Carmona Sosa. All rights reserved

This thesis has been typeset by LaTeX and the Sapthesis class.

Version: July 21, 2021

Author's email: viridiana.carmonasosa@uniroma1.it

a Don Mago, Reina
y a mis padres

Acknowledgments

First and foremost, I would like to express my gratitude to my advisor Prof. Roberto Di Leonardo for his confidence in me and giving me the opportunity to conduct my own research. I am also indebted my thesis referees: Professors Matteo Pierno, and Peter Galajda for their suggestions and encouragement.

During my PhD I have the opportunity of work with all my labmates. I would like to thank Silvio Bianchi, I learned a lot from him during the two months internship before the first year of my graduate work. I want to thank to Dario Dell'Arciprete, in the first months in Rome he helped me a lot given my zero italian. I thank to Claudio Maggi, Filippo Saglimbeni, and Giacomo Frangipane, Francesco Brasili, Nicola Pellicciotta, Helena Massana. I greatly benefited from the discussions I had with Prof. Ornella Ursini, I feel very grateful for all the time she dedicated to me each time I had some difficulties understanding the chemistry of part of my research.

In addition, I would like to thank to my parents Francisco and Inés, my sister Huri and my brother Francisco for all the love and support throughout my career. My nephew Miguelito has been an inspiration to me since he appeared in my life, he makes me want to be a better human being. I am particularly grateful with Rafael Díaz, since he moved to Rome and we met at Fiumicino Airport we have not stop talking, I am indebted with you for supporting me during my worst moments (y son precisamente esos besos los que reafirman que el vino es vino, el agua es agua, y que el prosciutto es prosciutto y es más rico con melón y compartido contigo). To my best friend and labmate, Stefano Ferretti I want to thank him for all the conversations we had before, during and after laboratory hours, for all the precious italian words he taught me. I would like to my friend living in Florence, Tania and Santiago. To my friends of the PhD: Fabrizio, Giovanni, José, Angelo, Silvia, and Rodrigo. I want to thank Ash, Gui, Masry, Judith, Álvaro, Daniel, Celia, Lupe, David, Rosa.

Abstract

Microfabrication techniques have opened up new ways to study the dynamics of microsystems expanding the range of applications in microengineering and cell biology. Among three-dimensional microfabrication techniques, two-photon polymerization enjoys a unique set of characteristics that make it appealing for designing complex structures of arbitrary form. During the last decades, two-photon polymerization has evolved from the first structure fabricated with this technique, a coil with a diameter of 7 μm and a total length of approximately 34 μm (by Maruo *et al.*), to generate sophisticated systems like remotely driven micromachines. In the present thesis, we address two main applications of microfabrication.

On the first line of research, the design and fabrication of efficient and self-powered micro-robots have been a very active research topic. Motile micro-organisms like *E. coli* may provide an optimal solution to generate propulsion in artificial microsystems. It has been demonstrated that microstructures can be transported when released on a layer of swarming bacteria, suspended in a bacterial bath, or covered by surface adhering bacteria. Although it is possible to obtain a net movement in the mentioned cases, the displacement is stochastic and self-propulsion characteristics are hard to reproduce. In this thesis, we investigate possible design strategies for bio-hybrid micro shuttles having a defined number of propelling units that self-assemble onto precisely defined locations. One of the biggest issues involved in the optimization design process of the microshuttles is an irreversible adhesion of structures in the substrate, which often is caused by Van der Waals attraction. To overcome this problem we use different stabilization methods with unsuccessful results. Looking for a less invasive and biocompatible strategy we investigate the possibility of changing the sign of Van der Walls forces turning them from attractive to repulsive. To this aim, we develop a method that demonstrates to reduce the adhesion observed before. So, the final design aims at minimizing friction and adhesion with the substrate while optimizing propulsion speed and self-assembly efficiency. Finally, using a mutated strain of *E. coli* the microshuttle can be remotely controlled by dynamic structured light patterns for reaching an optimal control of the motion of the structures.

In a different direction of microfabrication applications, 3D microstructures can also offer new opportunities to address more fundamental problems in the soft matter dynamic. On this second line of research, we have designed and used complex 3D microstructures to investigate the Brownian dynamics and hydrodynamics of propeller shaped particles, as well as to probe effective interactions in colloidal systems, like critical Casimir forces.

In the dynamics of microhelices we use optical tweezers to study the mechanic and hydrodynamic properties of micro-fabricated helices suspended in a fluid. For the case of rigid helices, we track Brownian fluctuations around mean values with a high precision and over a long observation time. Through the statistical analysis of fluctuations in translational and rotational coordinates, we recover the full mobility matrix of the micro-helix including the off diagonal terms related with roto-translational coupling. Exploiting the high degree of spatial control provided by optical trapping, we can systematically study the effect of a nearby wall on the roto-translational coupling, and conclude that a rotating helical propeller moves

faster near a no-slip boundary. We also study the relaxation dynamics of deformable micro-helices stretched by optical traps. We find that hydrodynamic drag only weakly depends on elongation resulting in an exponential relaxation to equilibrium.

In connection with the versatility of microfabrication by two-photon polymerization, we find the study of interaction in colloidal systems. At macroscopic scales, thermal fluctuations of a physical property on a system are typically negligible, but at the micrometer and nanometer scales instead, fluctuations become generally relevant and they give rise to novel and intriguing phenomena such as critical Casimir effect. Critical Casimir forces are induced between colloidal objects suspended in a critical binary mixture undergoing strong thermal fluctuations. So far, most of the experiments and proposed models consider the interaction between simple geometrical objects such as two spheres, or a single sphere and a plate. In the last part of this thesis, we propose a novel 3D printed microprobes consisting of the main body and two handles that can be optically trapped to directly measure effective forces and torques between colloidal objects with non spherical shapes.

The organization of this thesis is as follows. Chapter 1 gives a general introduction to the physical phenomenon behind the 3D microfabrication technique employed in our experiments, two-photon polymerization. We describe the differences between two phenomena: single-photon absorption and two-photon absorption, and explain the effectiveness of using two-photon polymerization for reaching a resolution of 100 nanometers in microfabrication. Then we present an experimental characterization of the voxel size of our custom-built two-photon polymerization set-up. We explain the sample preparation steps for microfabrication as well as the development of an innovative low-refractive index layer for eliminating irreversible adhesion of SU-8 microstructures.

Chapter 2 provides a general introduction to *E. coli* motility, the propulsion mechanism of these bacteria, and the circular trajectory developed by the microorganism when swimming near a rigid boundary. Besides, we briefly explain the possibility of using synthetic biology to obtain light driven strains of *E. coli* by the expression of Proteorhodopsin on the bacteria membrane.

In Chapter 3 we combine two-photon polymerization technique and genetically modified bacteria to create a biohybrid microshuttle. We start with a basic microshuttle design whose propulsion is obtained from four *E. coli* bacteria. After integrating ramps in another microshuttle model for minimizing the circular trajectory showed in the microstructure trajectory, we make major changes in the distribution of microchambers inside the last model named catamaran microshuttle. Exploiting the ability of a mutated strain of *E. coli* expressing proteorhodopsin, we successfully control the microrobot steering by illuminating our sample with green light patterns.

In Chapter 4 we design and use 3D microhelices from two different materials to investigate, through optical tweezers, Brownian dynamics, and hydrodynamics of this kind of chiral particles. Through the statistical analysis of fluctuations in translational and rotational coordinates we study the roto-translational coupling element from the mobility matrix of the micro-helix. Besides, we conclude that a rotating helical propeller moves faster near a no-slip boundary. For the case of a deformable micro=helix, we find that hydrodynamic drag only depends on its elongation.

Finally, Chapter 5 presents the design for a microprobe to measure critical Casimir forces using holographic optical tweezers. We show a characterization experiment for a micro-cube with two handles, concluding that a third handle will improve the stability of a microprobe inside the sample.

Contents

Part I

3D Microfabrication by Two-Photon Polymerization

Chapter 1

Microfabrication by two-photon polymerization

The work presented on this chapter was influenced by previous work from Gaszton Vizsnyiczai. Discussions with Ornella Ursini allowed a succesful generation of the low-refractive index layer in section 1.2.3.

1.1 Introduction to two-photon polymerization

Microfabrication techniques have enormously developed during the last decades, while we can trace back to 1954 their beginnings in the integrated circuit industry, nowadays these techniques have offered a number of new possibilities for the study of biological, chemical, and physical processes at the micron scale. Among the different microfabrication techniques, the most important ones are photolithography, soft lithography, film deposition, etching, and bonding. Photolithography is used to transfer a user-generated shape onto a material through the selective exposure of a light sensitive polymer. Soft lithography encompasses three different techniques which are all based on the generation and utilization of the mold of a microstructure out of polydimethylsiloxane (PDMS). Film deposition consists of the formation of micron-thick films on the surface of a substrate. Etching selectively removes materials from the surface of the microdevice by either chemical of physical processes. Finally, bonding adheres substrates together with or without the use of intermediary layers [19].

Recently, there has been a tremendous progress in another group of techniques closely related with photolithography, which allows fabrication of three-dimensional microstructures, this newest methods are known as laser-based direct-writing techniques. Due to the implementation of a laser beam and depending on its characteristics as the excitation wavelength and regardless of the laser output type (if it is continuous or pulsed), lasers can be employed to activate several chemical and physical processes.

The physical phenomenon behind the functionality of direct laser writing (DLW) is photon absorption [93]. While one of the earliest single-photon DLW works consisted in manufacturing optical waveguides in silica-titania glass sol-gel films[78], in 1997 it was first demonstrated the use of DLW by multi-photon polymerization

in the work of Maruo *et al.* [74] by the fabrication of several microstructures using a photosensible resin. For the purpose of this thesis the theory of two-photon absorption will be explained with a semi-classical approach based on reference [9], nevertheless the extrapolation to three or more photons can be easily done.

When light interacts with matter, the most common scenario is that the energy of a single photon is resonant with an energy difference between an occupied electronic state and a higher electronic state. Nevertheless, it was in 1930 when Marie Göppert-Mayer predicted in her doctoral thesis that, if the energies of two photons collectively match the energy gap between two electronic states in a material then it is possible for light to be absorbed. Unfortunately, due to the required high intensity source for providing an experimental realization, this kind of phenomena was not demonstrated until the invention of the laser. The first experimental verification of her theory was realized by Werner Kaiser when two-photon-excited fluorescence was detected in a europium-doped crystal[57].

In the case of single-photon absorption, the material has a linear response to the applied optical field, which means that the polarization P induced by the applied field can be written as:

$$P(\omega) = \epsilon_0 \chi(\omega) E(\omega) \tag{1.1}$$

where ω and E are the frequency and magnitude of the optical field, respectively, while ϵ_0 is the vacuum permittivity, and χ is the linear susceptibility of the material. The absorption coefficient α is then proportional to the imaginary part of the susceptibility:

$$\alpha(\omega) = \frac{\omega}{cn} \chi_{im}(\omega) \tag{1.2}$$

where n is the refractive index of the medium. The complete amount of light absorbed by a medium is proportional to the product of the medium's absorption coefficient and the light intensity, which in turn is proportional to the magnitude squared of the electric field, therefore the light absorbed is proportional to $|E|^2 \chi_{im}(\omega)$.

The medium response to a single or several applied fields it is not necessarily linear, so a more general expression for the Eq. (1.1) can be written as:

$$\boldsymbol{P} = \epsilon_0 \left(\chi^{(1)} \boldsymbol{E} + \chi^{(2)} \boldsymbol{E} \cdot \boldsymbol{E} + \chi^{(3)} \boldsymbol{E} \cdot \boldsymbol{E} \cdot \boldsymbol{E} + \cdots \right) \tag{1.3}$$

where, $\chi^{(n)}$ is the nth-order susceptibility, with $\chi^{(1)}$ being the linear susceptibility from Eq. (1.1), while the polarization and the electric fields are all considered to be vectors. Then, we can rewrite Eq. (1.3) as follows:

$$\boldsymbol{P} = \boldsymbol{P}^{(1)} + \boldsymbol{P}^{(2)} + \boldsymbol{P}^{(3)} + \cdots \tag{1.4}$$

where

$$\boldsymbol{P}^{(1)} = \epsilon_0 \chi^{(1)} \boldsymbol{E} \tag{1.5}$$

$$\boldsymbol{P}^{(2)} = \epsilon_0 \chi^{(2)} \boldsymbol{E} \cdot \boldsymbol{E} \tag{1.6}$$

$$\boldsymbol{P}^{(3)} = \epsilon_0 \chi^{(3)} \boldsymbol{E} \cdot \boldsymbol{E} \cdot \boldsymbol{E} \tag{1.7}$$

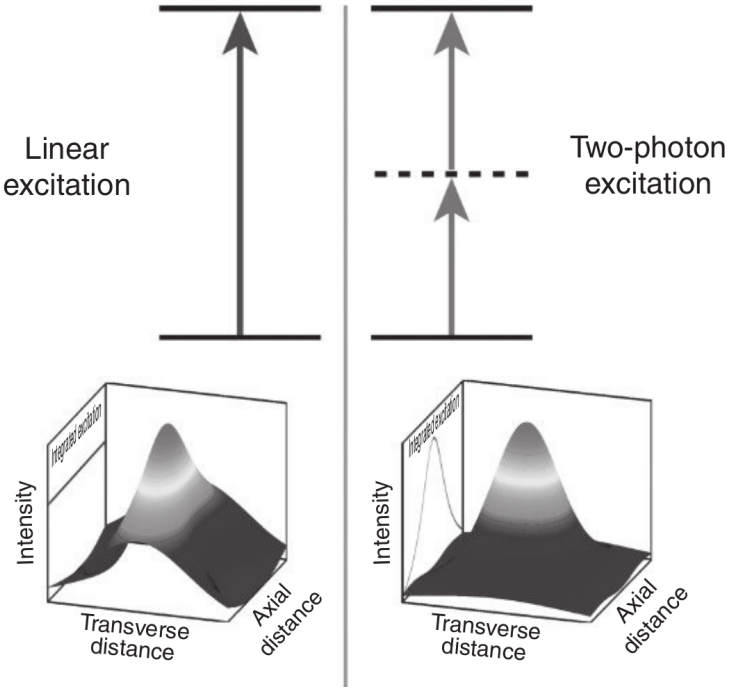

Figure 1.1. Linear and nonlinear absorption Top: Schemes of the energy-levels. Lineal excitation on the left and two-photon excitation to the right. Bottom: Spatial intensity profiles in the center of the beam for both cases. The profile of stimulated molecules integrated in the transverse direction is presented at the left of each 3D plot. From [9].

and so on. $\boldsymbol{P}^{(n)}$ is known as the n^{th}-order polarization.

Considering Eqs. (1.1) and (1.1), we notice that the rate of linear absorption of a medium is proportional to $\boldsymbol{E} \cdot \boldsymbol{P}^{(1)}$. In the case of absorbing two-photons, the process must depend on the square of the intensity, and therefore the rate of this process is proportional to $\boldsymbol{E} \cdot \boldsymbol{P}^{(3)}$, which involves four optical fields. Basically, the expression for the rate of n-photon absorption will be proportional to $\boldsymbol{E} \cdot \boldsymbol{P}^{(2n-1)}$, which means that multiphoton absorption depends only on nonlinear susceptibilities (or polarization) of odd order.

While the probability of observing an n-photon absorption process as the result of the addition photons of n different frequencies (nondegenerate process) is non-zero, the vast majority of multiphoton fabrication processes use photons of the same frequency (degenerate process). Moreover, in fabrication techniques, degenerate multiphoton absorption employs a single laser beam.

From Figure 1.1 we notice that in the case of a two-photon absorption phenomenon there is the null existence of a energetic state to be resonant with the individual photons. Instead, the process follows a more complicated path: the first photon causes a transition to a virtual state, which has a significantly short lifetime due to the fact that it is composed of a combination of the far-off-resonance states of the atom or molecule, thus the second transition typically must occur within roughly 1 fs of the initial transition. So, two-photon absorption will be observed if both photons are in the same place at the same time.

The nonlinear intensity dependence of multiphoton absorption is of main im-

portance for microfabrication because this phenomenon allows absorption to be tightly confined in three dimensions if the excitation source is focused into a small volume. For understanding this confinement, we start considering linear absorption: the number of molecules addressed in a plane perpendicular to the direction of propagation of a light beam is proportional to the area of the beam; but the intensity in the same transverse plane is inversely proportional to the area; because the total population of excited molecules is proportional to the product of the intensity and the number of molecules, in the limit of weak absorption the same number of molecules are excited in each transverse plane of the beam (Figure 1.1, bottom left). In the case of two-photon absorption the number of molecules excited in a transverse plane is proportional to the number of molecules (linear in area) multiplied by the square of the intensity (inversely proportional to area squared). Thus, the number of excited molecules is inversely proportional to the area of the beam and, likewise, proportional to the transverse spatial intensity profile (Figure 1.1, bottom right). Under appropriate intensity conditions, it is therefore possible to confine excitation to within the focal region of the light beam [9].

Due to a virtual state dependency in the transition for two-photon absorption, this process is relatively inefficient, besides, given an incoherent light source it is highly challenging to produce it. Hence, the experimental demonstration of two-photon absorption was achieved after the laser had been invented [57]. Nevertheless, even after this experiment, this process was not ideal for practical applications in areas such as lithography and imaging, as the intensities required were still so high that most samples would be damaged.

Fortunately this situation changed when lasers with picosecond and subpicosend pulse lengths were finally available. The peak intensities of ultrafast pulses can be remarkably high, but the duty cycle is typically on the order of 10^{-4} to 10^{-6} (or even smaller), in this way high squared intensities can be achieved at low average powers without damaging the material. The first famous application of two-photon absorption was performing 3D fluorescence microscopy[31]. The recognition that other photophysical and photochemical processes could also be localized using two-photon absorption led to accelerating the use of this phenomenon in 3D microfabrication, originating two-photon polymerization (TPP).

The photoresists for TPP include negative-tone and positive-tone photoresists. In the case of negative photoresists, two-photon absorption generates the crossslinking of polymer chains through radical polymerization, in this way the exposed region becomes insoluble to the developing solvent and the structure is written directly in the sample. Contrarily, for positive photoresist, two-photon absorption produces polymeric chains breaking by means of photoacid degradation making the exposed region soluble to the developing solvent, hence the inverse structure is written in the sample [38]. The most common photoresists for TPP are negative photoresists incorporating acrylic oligomers or epoxy resins. Their fundamental materials contain photoinitiators employed for radical generation, monomers that compose the main skeleton of micro or nanostructures and crosslinkers providing the final microstructure with a resistance to development solvents.

The first photoresist used for TPP was SCR500, a commercially available resin composed of urethane acrylate monomers and oligomers in addition to photoinitiators, which is transparent to an infrared laser allowing it to penetrate deeply [74].

Nevertheless, we use another commercial photoresist: SU-8, a negative, epoxy-based materials widely employed for high-aspect ratio microstructures fabrication. Once the laser power reaches the threshold of polymerization, the long molecular chains in SU-8 begin to crosslink producing a final microstructure that can resist to be developed by commonly used solvents.

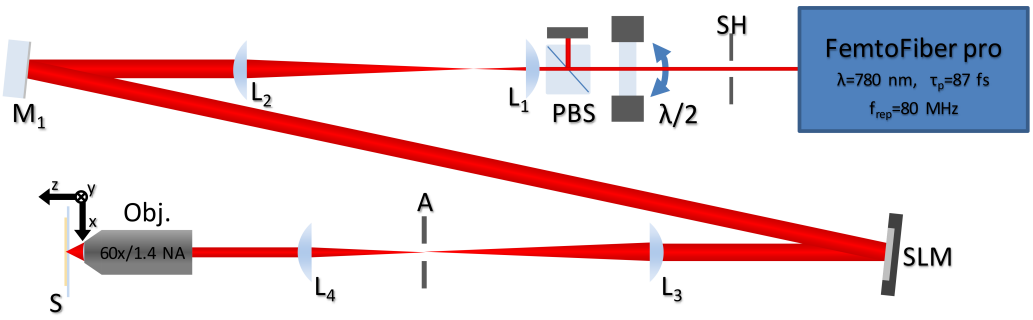

Figure 1.2. TPP optical set-up Schematic layout of our custom built two-photon polymerization set-up. Figure taken from [113].

Our custom built two-photon polymerization set-up is illustrated in Figure 1.2. A near-infrared femtosecond fiber laser beam (FemtoFiber pro NIR, TOPTICA Photonics AG) with a center wavelength of 780 nm, a pulse width of 87 fs,a repetition rate of 80 MHz, and 160 mW optical power is used for TPP. Exposure during fabrication is toggled by an optical shutter (SH). We set the fabrication laser power by a rotateable half-wave plate followed by a polarizing beam splitter cube (PBS). Lenses L_1 and L_2 expand the laser beam which is then reflected onto a holographic spatial light modulator (SLM) (X10468-02, Hamamatsu Photonics). At the same time, by means of lenses L_3 and L_4, the SLM is in 4f conjugation to the back focal plane of a high numerical aperture oil immersion objective (Nikon Plan Apo Lambda 60x 1.4). The SLM allows to generate multiple fabrication foci as well as impose wavefront correction on the fabrication beam. The zero and high diffraction order are blocked in the focal plane of L_3 by a thin wire and by an adjustable rectangular aperture (A). During fabrication the high NA focus of the laser is scanned inside a photoresist layer (S) carried on a microscope coverglass. The photoresist scanning in three dimensions is done by a 3-axis piezo translation stage (P563.3CD, Physik Instrumente (PI) GmbH & Co. KG) controlled through a NI-DAQ DA card.

1.2 Characterization and optimization of the two-photon polymerization process

1.2.1 Experimental characterization of voxel size for TPP

While the fabrication of simple thick 3-D structures (with dimensions of the order of 100 of microns) does not require full knowledge of the minimum polymerized volume in the photoresist, in the case of smaller and more complex micro and nanostructures

it is fundamental to characterize the resolution of two photon polymerization process, given by the dimensions of a voxel (volumetric pixel), term given to the smallest unit of solidified polymer that forms at the focal point of the light during two-photon polymerization.

One of the first experimental studies on this aspect is the work of Sun *et al.* from 2003 [103] where they report the importance of very basic parameters in the size and shape of volume elements in the microfabrication process, such as laser beam polarization, numerical aperture (NA) and exposure time. Part of their experimental results are shown on Figure 1.3, where scanning electron microscopy (SEM) images from single voxels generated with different NAs are presented. They demonstrated the importance of NA, which change redistributes the photon energy at the focal volume.

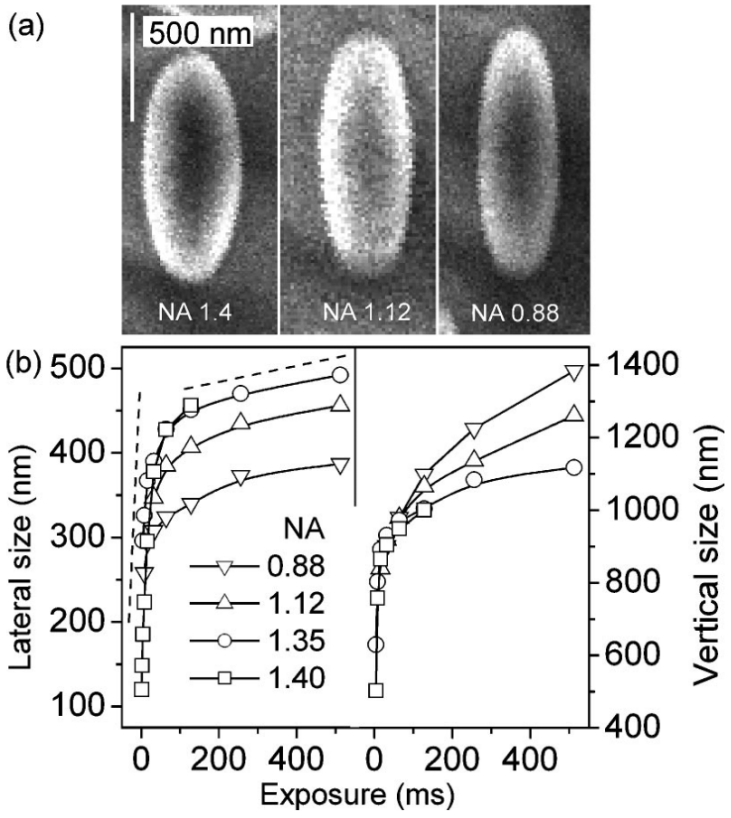

Figure 1.3. Influence of NA in voxel dimensions. (a) SEM pictures from side-view voxels produced with the same focal spot laser beam. (b)Plot of lateral and longitudinal voxel size depending on the exposure time for different NAs. From [103].

In the present thesis we chose a different method for developing a voxel size calibration. Instead of studying single voxels as in [103], we measured scanned lines. Using SU-8 2015, first we fabricated a scaffold composed of small pillars with a height and diameter of 8 μm and 1 μm, respectively; the separation between each pillar was 5 μm, in the space among pillars and at a height of 6 μm a simple line was fabricated by scanning 13 different speeds. We follow this procedure for 11 laser powers, two identical arrays of pillars and lines are shown in figure 1.4, from

these images we can appreciate that line fabrication depends on the laser intensity threshold for the photoresist. For example, the upper group of pillars in figure 1.4(a) corresponds to a laser power of 1 μm and we observed that only the scaffold was fabricated, in contrast, at the other end, in the group corresponding to 10 μm, the whole array of lines reached the threshold of polymerization.

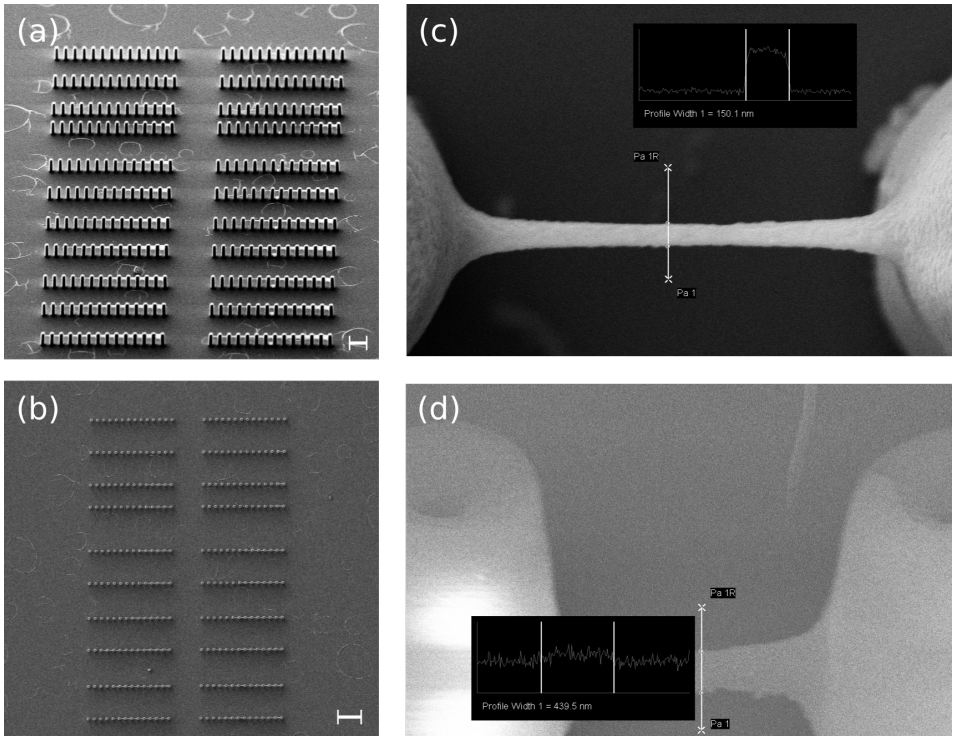

Figure 1.4. SEM image of two identical groups of pillars and scanned lines.(a) Tilted view. The scale bar is 10 μm.(b)Top view. The scale bar is 20 μm.(c) Measure of the line width for a laser power and scanning speed of 2.5 mW and 6 $\mu m/s$, respectively.(d) Tilted measure of the line height for the same line.

After measuring width and height of the lines from SEM images (shown in Figure 1.5) and considering an inclination error related with the microscopy technique, we obtained the values for lateral and longitudinal voxel size. Using this data, we developed a model for predicting the voxel size as a function of laser power and scanning speed.

The rate of density of radicals produced by the femtosecond laser pulses in the photoresist, is a function of the square of the beam intensity:

$$\frac{\partial \rho}{\partial t} = \alpha \cdot I^2(x, y, z), \tag{1.8}$$

where $I(x, y, z)$ is the laser beam intensity. Because the microfabrication calibration was done by moving the laser beam only on the x-axis to generate a line, we can substitute the x coordinate by $x - vt$ (where v is the scanning speed), and then integrate:

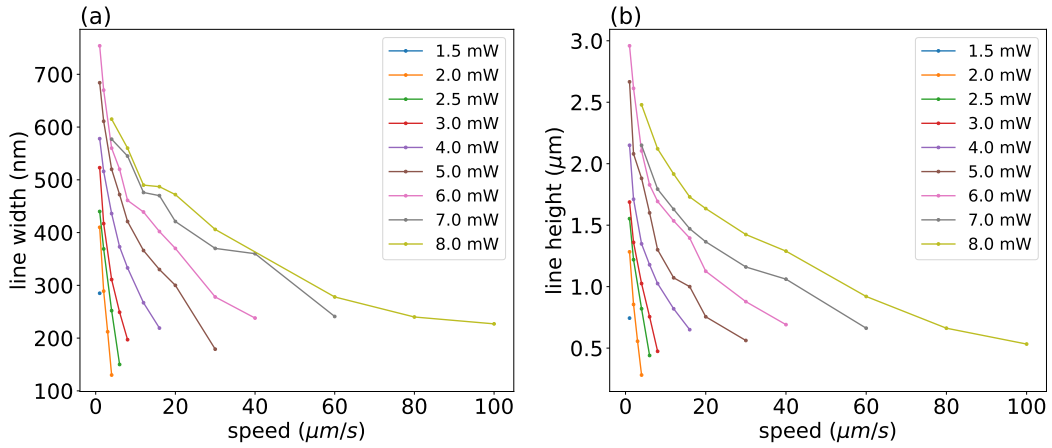

Figure 1.5. Voxel size values obtained by SEM microscopy.(a) Direct measurements for the line width for different values of scanning speeds and laser powers.(b) Value of the height for all the lines.

$$\int_{-\infty}^{\infty} \dot{\rho} dt = \frac{\alpha}{v} \int_{-\infty}^{\infty} I^2(x - vt, y, z) d(tv)$$
$$= \frac{\alpha}{v} \int_{-\infty}^{\infty} I^2(x - x'y, z) dx' \tag{1.9}$$

but, assuming that we use a Gaussian laser beam, the intensity distribution can be expressed with the following expression[89]:

$$I(x, y, z) = I_0 \left(\frac{W_0}{W(z)} \right)^2 \mathrm{e}^{\frac{-2(x^2+y^2)}{W^2(z)}} \tag{1.10}$$

where I_0, $W(z)$, and W_0 are the beam intensity at the central axis in the focus plane, the beam width, and the radius of the focused beam spot, respectively. So, the integral in Eq. (1.9) can be written as:

$$\int_{-\infty}^{\infty} I^2(x - x', y, z) dx' = I_0^2 \left(\frac{W_0}{W(z)} \right)^4 \mathrm{e}^{\frac{-4y^2}{W^2(z)}} \underbrace{\int_{-\infty}^{\infty} \mathrm{e}^{\frac{-4(x-x')^2}{W^2(z)}} dx'}_{\text{Gaussian Integral}} \tag{1.11}$$
$$= I_0^2 \left(\frac{W_0}{W(z)} \right)^4 \mathrm{e}^{\frac{-4y^2}{W^2(z)}} \sqrt{\frac{\pi W^2(z)}{4}} \tag{1.12}$$
$$= \sqrt{\pi} I_0^2 \frac{W_0^4}{2W^3(z)} \mathrm{e}^{\frac{-4y^2}{W^2(z)}} \tag{1.13}$$

so, introducing Eq. (1.13) in Eq. (1.9), and considering $z = 0$, we obtain:

$$\rho = \frac{\alpha}{v}\frac{I_0^2\sqrt{\pi}W_0}{2}\mathrm{e}^{\frac{-(2a)^2}{W_0^2}} \tag{1.14}$$

where $2a$ corresponds to the lateral size of the voxel $\Delta x = \Delta y$, then, because the laser power[89] can be written as $\mathbf{P} = \frac{1}{2}I_0\left(\pi W_0^2\right)$, and multiplying for some constants, we can rearrange the terms such that:

$$\mathrm{e}^{\frac{(\Delta x)^2}{W_0^2}} = \frac{\beta\mathbf{P}^2}{v\rho^*} \tag{1.15}$$

from which we find the expression for the lateral size of the voxel:

$$(\Delta x)^2 = W_0^2\ln\left(\frac{\mathbf{P}^2}{v}\right) - W_0^2\ln\left(\frac{\rho^*}{\beta}\right) \tag{1.16}$$

if some constants are introduced we can reshape the equation to:

$$\left(\frac{\Delta x}{\sigma}\right)^2 = m_{xy}\ln\left(\frac{\mathbf{P}^2}{\sigma v}\right) + b \tag{1.17}$$

where $\sigma = \frac{2\lambda\cdot 1.22}{NA}$, and λ, NA are the laser wavelength and the numerical aperture, respectively; while m_{xy} and b are constant values that will be extracted from fitting this equation to the data obtain by SEM.

For the estimation of longitudinal voxel size, we consider the expression for intensity on the beam axis[89] $I(0,0,z) = \frac{I_0}{1+(z/z_0)^2}$ and after some manipulations we obtain this expression

$$\left(\frac{\Delta z}{\sigma}\right)^2 = m_z\sqrt{\left(\frac{\mathbf{P}^2}{\sigma v}\right)} + c \tag{1.18}$$

where σ is the same constant defined in the case of lateral voxel size, while m_z and c are constant values.

After obtaining the Eqs. (1.17) and (1.18) we computed the squared values of lateral and longitudinal voxel size as function of the variable $\mathbf{P}^2/\sigma v$, as shown in Figure 1.6. The last step consisted in fitting Eq. (1.17) and Eq. (1.18), and then obtaining the values for the constants m_{xy}, b, m_z, and c, and finally generating a function to compute the voxel size in terms of the laser power and scanning speed.

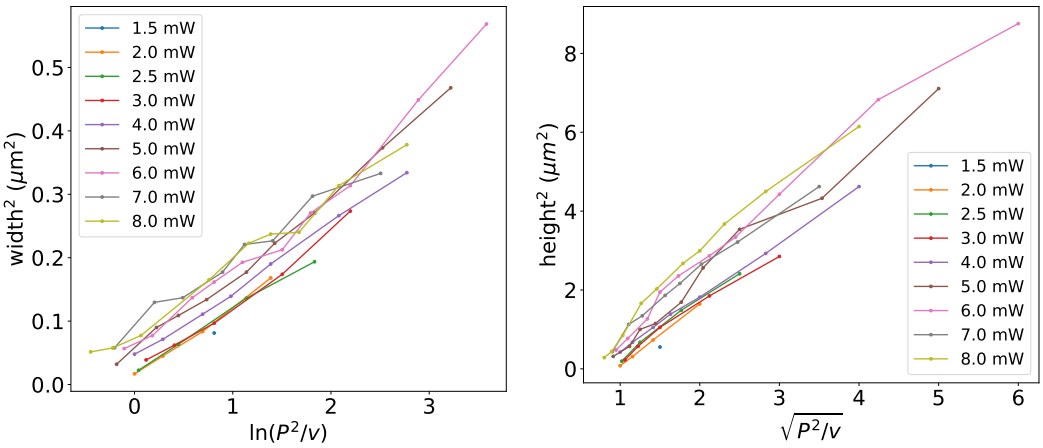

Figure 1.6. Experimental data as function of laser power and scanning speed. Squared values of voxel size measurements obtained by SEM images as function of **P** and v. Left plot corresponds to squared lateral size while squared longitudinal voxel size is presented on the right.

Given the characteristics of this microfabrication technique, such as resolution of the order of 100 nanometer, the spatial confinement of the laser energy allowing the fabrication of complex 3D objects, the aspect ratio of the genetared structures, in addition to the time and materials used, we consider TPP a technique beyond the state-of-the-art [48].

1.2.2 Microfabricated sample preparation

For the purpose of this thesis, the microstructures must be fabricated with a biocompatible material, i.e., it must sustain and promote bacterial motility, besides, the surface of the finished structure should promote an easy attachment of bacteria. Furthermore, for the tracking microstructure it is important to have and object with clearly defined boundaries, allowing detection of it, which means that the microrobot must be transparent but have a high refractive index. Given all these requirements, SU-8 Series 2000 (KAYAKU Advanced Materials, Inc., Westborough, MA, USA), a negative photoresist that forms strong crosslinking on exposure to ultraviolet light, and the non-exposed areas are easily removed using a developer solution. In Figure 1.7[1] it is shown the schematic process followed for SU-8 samples.

Coverslip cleaning and pre-treatment

The selected substrate for the generation of SU-8 microstructure is a coverslip of soda lime glass, dimensions 24 $mm \times 50$ mm. To achieve uniform, defect-free deposition of the photoresist, a fundamental step is that the substrate surface must be free of dust and other particles. One of the most commonly used procedures for small-scale cleaning of glass is by the use of an acid solution. In our case, we

[1]Picture modified from `https://www.elveflow.com/microfluidic-reviews/soft-lithography-microfabrication/su-8-mold-lithography/`

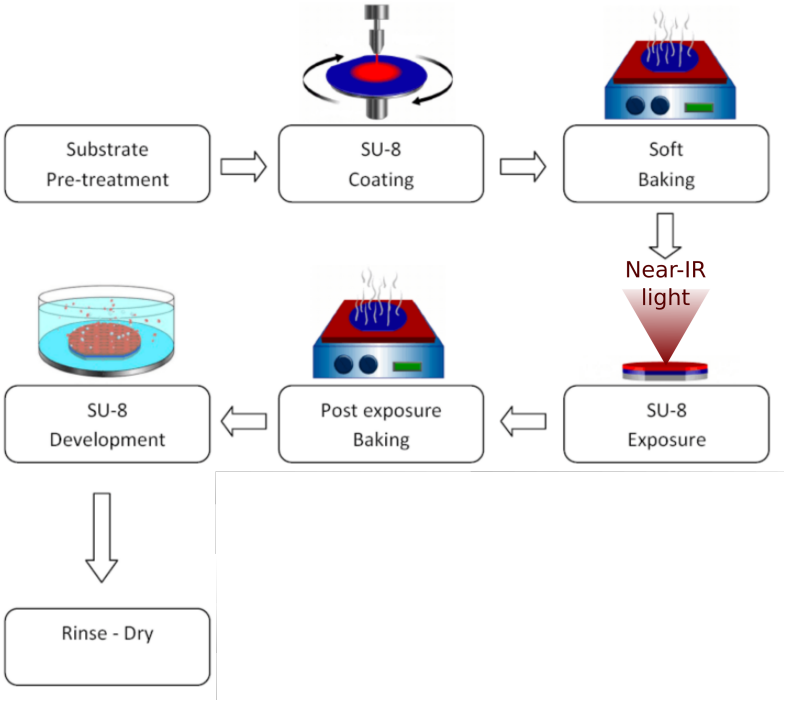

Figure 1.7. Microfabrication sample preparation. Scheme of the process for generating a photoresist layer on a substrate for microfabrication by TPP. Picture taken from the official website of Elveflow Microfluidics.

immersed the coverslips in a solution composed of sulfuric acid and a Nochromix (Godax laboratories, Takoma Park, MD, USA) at 5%(w/v), for a period of 24 hours minimum. The coverslips are extracted from the acid container using stainless acid-proof tweezers, and then a rinse in pure water is followed. Immediately after removal from the rinse, the slide is blow dried using clean compressed air (Nitrogen).

As mentioned in reference [3]: verification of a successful cleaning procedure following acid cleaning is essential. The sample should be completely wettable to water during the pure water rinse. Wettability of a surface to water in this context implies that a film of water on the surface does not dewet. Dewetting is observed when dry patches are formed, where the liquid film has receded from an area of surface. They are characterized by the presence of a liquid film with thickness of order one millimeter adjacent to a "dry" zone (by visual observation). This may be verified, if necessary, by halting the water flow and holding the substrate vertically. The water film will then thin. As it thins, colored light interference fringes should be observed. If dry patches are formed before the interference fringes are seen, the glass is not completely wetting in these areas and the cleaning has failed. On completion this test, the glass should immediately be re-wet with water and dried carefully as described above.

Another important property of the substrate is its wettability, which refers to the ability of the photoresist to spread on the surface and form intimate contact and strong chemical bonds with surface molecules, and, as a consequence, it allows a uniform spread of SU-8. For improving the wetting of our coverslips we applied

a plasma treatment using Oxygen at 2 bars with a flow rate of 80 scm during 10 minutes. After the plasma treatment, coverslips must be stored in a clean container and kept away from atmospheric contaminants or the transfer of oils by e.g. touching with bare skin. Due to hydrophobic recovery [56] it is advisable to follow with the next step as sooner as possible.

Depending on the final aim of a microstructure,i.e., if it will remain attached to the coverslip or if it will used as a free standing microstructure, then, for the former case an adhesion promoter can be deposited by spin coating before applying the photoresist. We strengthened adhesion by dispensing 300 μL of Omnicoat (KAYAKU Advanced Materials, Inc., Westborough, MA, USA) with a micropipette while the coverslip was rotating on a spin coater (Chemat Scientific) [2] at a speed of 1500 rpm for 49 s. Then, we bake the sample for 2 minutes at 200 $°C$. For a stronger adhesion we applied this step 3-times, in this way we generated 3 layers of Omnicoat. On the other hand, if we will use free-floating microstructures, then this passage is omitted and the protocol for water-soluble sacrificial layer is implemented as explained in the next section. Light must be turned off during this whole part of the process.

Photoresist coating

For generating the photoresist layer where microstructures were fabricated, we implemented an analogous process used in Omnicoat application. Based on previous observations, and due to both SU-8 viscosity and the fact that it is stored in a cold environment, allowing the photoresist to warm up to room temperature before spinning prevented bubbles formation on the layer. Using a micropipette we spread 300 μL on the coverslip distributing it from the center and following to each of the corners, then we put the sample as centered as possible on the spin coater chuck, and coat during 78 seconds. Depending on which type of SU-8 is used, then the spin coating speed is different, as well as the final thickness of the layer, as shown in Table 1.1. The main differences between SU-8 2000 and SU-8 3000 series is that the last one has been developed for improving substrate adhesion and reducing coating stress.

Table 1.1. Parameters for the spin coater speed and the resulting layer thickness for the two types of SU-8 photoresist available.

SU-8	Spinning speed (rpm)	Thickness (μm)
2015	800	~ 50
3025	2000	~ 25

After SU-8 spin coating the photoresist layer thickness is approximately 50 μm, for removing the exceeding material accumulated on the border of the coverslip we used lens paper. Subsequently, samples are kept in a clean container avoiding any exposure to light until continuing with the soft bake. As in the last step, during photoresist coating the lights must be kept off.

[2] Model KW-4A Spin Coater 110V `http://www.chematscientific.com/Spin-Coating/KW-Series/KW-4A-Spin-Coater-110V-SkuID-2`

Photoresist soft-bake

The purpose of baking the photoresist layer before exposure is to evaporate the solvent that remains after spin coating. Several studies have demonstrated the strong relation between solvent content and aspect ratio of microstructures showing that a quantity around 7% of solvent generates a high fidelity in microfabrication [117]. We used a hot plate for the soft-bake of our sample, which presents some advantages in comparison with the use of an oven, e.g., the hot plate allows to heat from the bottom to the top of the coverslip favoring solvent evaporation, instead, using an oven generates an external hardened layer on the SU-8 surface producing a low solvent concentration and, hence the slow down of solvent evaporation in the bulk. Given the photoresist layer thickness obtained from the previous step, and according to the manufacturer,[3] we use a temperature of 95 $^{\circ}C$. While the soft baking time suggested by the manufacturer is around 10 minutes, after a previous optimization process the standard time was changed to 30 minutes. Nevertheless, for the calibration process (subsection 1.2.1) we observed that 2 hours of soft bake allowed to produce high-aspect ratio microstructures. A longer soft bake time (12 hours) was used for measuring the voxel size in subsection 1.2.1, from the comparison between the obtained values from SEM images we concluded there were not significant differences so we established 2 hours soft baking as new standard time. After this process, samples are stored in a clean container avoiding any exposure to light.

Two-photon polymerization

The sample is placed on a holder mounted on the piezo-stage (indicated by S on Figure 1.2). Due to two-photon polymerization, the exposed photoresist to near-infrared light will initiate the cross linkage by the activation of the photo-active component. Since SU-8 is a negative photoresist, the parts not exposed are dissolved during development while the rest of the photoresist will be polymerized.

Photoresist post-exposure bake

The next step after two-photon polymerization of SU-8 is a second bake denominated post-exposure bake. Once the energy dose is provided to the photoresist by two-photon absorption, the photoactive components in SU-8 are stimulated, but, to continue the reaction it is required further energy which given by this bake. Due to mechanical stress inside the SU-8 photoresist the heating and cooling down of the sample had to be done gradually. Thus, we set the initial temperature of the hot plate at 65 °C, followed by increments of 5 °C per minute until reaching 95 °C, then the sample was kept at this temperature for a total of 7 minutes. Finally, the hot plate is switched off and the sample remains still in it, producing a progressive cooling down. Make sure your sample is at the room temperature before continuing the process.

[3] `https://kayakuam.com/wp-content/uploads/2019/09/SU-8-3000-Data-Sheet.pdf`

Development and dry sample

The development is the process through which the non linked SU-8 photoresist is removed from the sample by the use of a solvent. It is after this step that the microstructures are revealed on the substrate. SU-8 is developed using the SU-8 developer [4] which is mainly composed of propylene glycol monomethyl ether acetate (PGMEA). First, the substrate is submerged in a bath container of 50 mL of SU-8 developer in a downward position [25], i.e., with the photoresist layer facing the bottom of the container. After 5 minutes, the coverslip is transferred to a second, cleaner bath and further developed for 5 more minutes. We repeated this step for the third time, and then, for the rinse part, we placed the sample on a bath containing a mix of double distilled water and ethanol (25 $mLofeachliquid$) and after 5 minutes we transferred the substrate to second, cleaner rinse bath for further 5 minutes. We repeated this procedure in a third rinse container for 5 minutes. Finally, the sample was dried applying a gentle blow of Nitrogen. In the case of using free standing microstructures, then the last three rinse steps are omitted.

Water-soluble sacrificial layer for free microstructures

Throughout this thesis, most of the experiments require implementing free-floating microstructures. In our laboratory, the traditional method for detaching structures from the substrate is by a mechanical micromanipulator, but this strategy can be slow, and cumbersome, besides damaging the structures. An alternative approach of releasing microstructures is by means of a sacrificial layer, nevertheless, this strategy frequently involves the use of toxic chemicals. For example, the material most commonly used is silica (SiO_2); by applying aqueous hydrofluoric acid (HF), SiO_2) is selectively etched. HF also etches many other materials, including metal oxides and organic polymers [70]. In contrast, the use of water-soluble polymers to for this purpose have several attractive characteristics: they can be easily deposited by spin-coating, the resulting layer can be dissolved in water, no corrosive reagents or organic solvents are required. Based on the characterization of water-soluble sacrificial films developed by Linder *et al.* [69] we selected Dextran for the release layer.

Based on [69, 98], we developed the following protocol.

Materials

- Dextran average mol wt 64,000-76,000 [5]
- Double-distilled water

Procedure

1. Prepare Dextran solution by mixing the appropriate amounts of Dextran and water in a Falcon tube, as show in the table
2. Complete dissolution of Dextran is obtained by placing the Falcon tube in a bath of hot water at 95°C for 30 minutes.

[4] `https://kayakuam.com/products/su-8-developer/`

[5] `https://www.sigmaaldrich.com/catalog/product/sigma/d8821`

Table 1.2. Parameters for spin-coating Dextran solutions as a pretreatment for microfabrication layers.

Solution concentration (w\v)	Dextran (g)	Water (mL)	Spin-coating speed (rpm)
2.5	0.25	10	1000
5.0	0.50	10	4000

3. Once that the solutions reach room temperature, they must be filtered (0.45 μm or 5 μm pore size for solutions of polymer with less or more than 5% (w/v), respectively).

4. Dispense onto the substrate until about 90% of the surface is covered with the solution and wait 30 seconds.

5. The sacrificial layer is then prepared by spin-coating the substrate at the corresponding speeds written in the previous table for a time lapse of 15 seconds.

6. Then the film is baked on a hot plate at 150°C for 2 minutes.

7. Next, SU-8 layer can be spin-coated on the Dextran layers as normally.

8. The exposed substrate is post-baked and developed in PGMEA (SU-8 developer) using the 3 steps of 5 minutes inside the plastic container.

9. Finally, the substrate was simply dried with nitrogen after PGMEA development.

1.2.3 Van der Waals sign reversal to eliminate adhesion

A common problem when working with free-floating microstructures is aggregation between objects and adhesion to the substrate. On this section we present a novel method for addressing this issue.

Colloids contain two phases in which one substance is dispersed in another. The dispersed substance is usually called the dispersed phase, and the dispersant is also called a continuous phase. Given the interactions within colloidal systems, they are not stable in time. The concept of stability used here is intended as a balance between two kind of forces: the repulsive electric double layer forces and the attractive, short-range Van der Waals forces. If the sum of the repulsive forces is higher than that of the attraction forces, the described system can be considered stable. At short distances, attractive Van der Waals forces are always stronger then electrical repulsion, giving as result adhesion between particles. The addition of different substances as well as other factors such as the concentration, ionic strength or pH can change the total potential energy of interactions. In the case of macromolecules addition, the mechanisms of stabilization can be divided in three: electrosteric stabilization, steric stabilization, and depletion stabilization. The steric and electrosteric stabilization mechanism apply to the situation where a polymer is attached to the particle surface; the difference between both methods is that the

former one implies the use of a non electrostatic charged polymer while in the last one a polymer with an ionic nature is employed. For the depletion method a polymer is not adsorbed on the solid particle and it is used as a mechanical barrier between the solid particles which leads to a decrease in the attraction forces [75].

In many systems colloidal stabilization is accomplished through these methods, nevertheless, in our case they have some disadvantages. The use of bacteria represents a constrain for the possible techniques to implement, mainly because the motility buffers used for bacteria contain sodium chloride (NaCl) which affects the repulsive electrostatic forces (depending on the salt concentration these forces can be progressively screened until they are dominated by attractive Van der Waals forces [37]) besides adding stabilization polymers in bacterial solutions can interfere with their behavior or even damage them. For this reason we approached to adhesion problem from a different perspective.

Van der Waals interactions represent the attractive forces in adhesion and aggregation problems, but there is the possibility of inverting their sign, thus contributing to the repulsive forces and avoid adhesion to the surface. The deduction of the following expression is beyond the scope of this thesis, nevertheless more information can be found at [55, 64].

The Hamaker constant A is a coefficient accounting for the Van der Waals interaction between two materials. In the scenario where two macroscopic phases 1 and 2 are interacting across a medium 3, then A is given by:

$$\begin{aligned} A_{total} = A_{\nu=0} + A_{\nu>0} \approx \frac{3}{4} kT \left(\frac{\epsilon_1 - \epsilon_3}{\epsilon_1 + \epsilon_3}\right)\left(\frac{\epsilon_2 - \epsilon_3}{\epsilon_2 + \epsilon_3}\right) \\ + \frac{3h\nu_e}{8\sqrt{2}} \frac{(n_1^2 - n_3^2)(n_2^2 - n_3^2)}{(n_1^2 + n_3^2)^{1/2}(n_2^2 + n_3^2)^{1/2}\{(n_1^2 + n_3^2)^{1/2} + (n_2^2 + n_3^2)^{1/2}\}} \end{aligned} \tag{1.19}$$

There are several interesting aspects of this equation:

- "In the symmetric case", i.e., two identical phases 1 interacting in a medium 3, the Van der Waals force is always attractive (A positive), while between different bodies in a medium it can be attractive or repulsive (A negative).
- The Van der Waals force between any two particles in vacuum or air ($\epsilon_3 = 1$ and $n_3 = 1$) is always attractive.
- If the relation $n_1 > n_3 > n_2$ is satisfied, then Van der Waals force is negative.

Consider the situations presented in Figure 1.8. The refractive index of glass is $n_{glass} = 1.51$, for the medium $n_{water} = 1.33$, and the refractive index of polymerized SU-8 is $n_{SU-8} = 1.57$[6], for the scenario shown in Figure 1.8(a), and according to Eq. 1.19, the Van der Waals forces are attractive, thus the SU-8 particle will attached to the glass. In contrast, if glass is coated with a material whose refractive index is smaller than n_{water}, then the situation presented in Figure 1.8(b) is possible, and Van der Waals forces will be reversed avoiding surface adhesion.

[6] According to `https://refractiveindex.info/?shelf=other&book=negative_tone_photoresists&page=Microchem_SU8_3000`

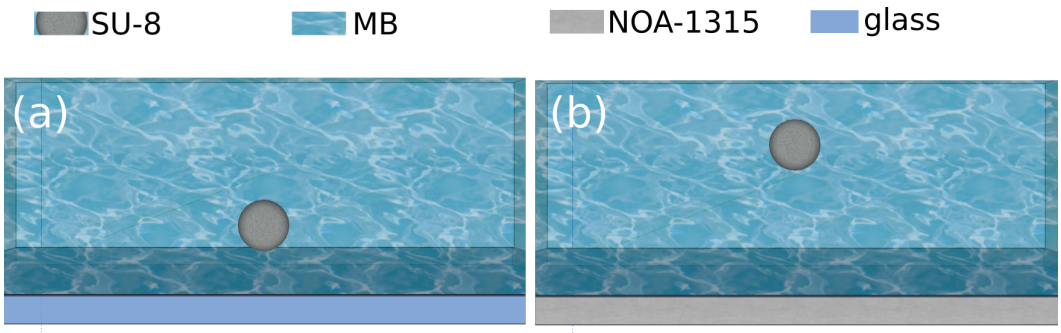

Figure 1.8. Van der Waals inversal sign. (a) The refractive indices of the glass-substrate, the medium (water) and the microparticle made of SU-8 do not satisfy the relation $n_1 > n_3 > n_2$ so, the forces between the particle and the substrate are attractive. (b) In the same scenario but substituting the glass-substrate with an UV-adhesive layer which refractive index is smaller than the one of the water, the Van der Waals forces are sign inverted, resulting in repulsive interactions.

After searching for a material with a refractive index smaller than n_{water} capable of being applied upon the substrate, we found a commercial UV-curing adhesive suitable for Van der Waals reversal sign: Norland Optical Adhesive 1315 which refractive index is $n_{NOA} = 1.315$ (NOA 1315)[7]. Due to NOA 1315 composition (1-15 % of Aliphatic Urethane Acylate and 85-99% of Acrylic Monomer), this adhesive exhibits oxygen inhibition when used exposed to air [92], and, when used as a coating, the temperature of the adhesive must be kept below 9° C to prevent vaporization.

To overcome oxygen inhibition it is necessary to cure the adhesive under an inert atmosphere. Nitrogen (N_2) is commonly used for this purpose, however we selected carbon dioxide (CO_2) for generating an inert atmosphere because of the several advantages of it in comparison with N_2 [101, 102]. For example, CO_2 is widely available, and at least as cheap as N_2, besides CO_2 is heavier than air and can be easily maintained in a container. Based on different sources [92, 101, 102, 68], we developed a method for generating a low-refractive-index layer.

In the laboratory, all the Norland UV curing adhesives with low refractive index (from 1.315 to 1.38) exhibit oxygen inhibition when used exposed to air, to overcome this the adhesive must be cured under an inert atmosphere, such as nitrogen or carbon dioxide. Besides, in some cases for generating a coating the temperature must be kept below 9°C to prevent vaporization.

First method: thin plastic film

For adhesives where a low temperature is not required, we developed a method with no implementation of inert atmosphere:

Materials

- A flat surface, this can be a plastic box, or a piece of metal
- Thin plastic film, we used food wrap

[7] https://www.norlandprod.com/adhesives/NOA1315.html

- Fishing thread
- Cover slip
- Norland 13685 (or any other with a low viscosity)
- THORLABS UV Mounted LED M365LP1

Procedure:

1. Expand the food wrap on the flat surface avoiding the air bubbles formation between the surface and the plastic film.
2. Use fishing thread as spacer between the food wrap and a cover slip.
3. Introduce 50 μL of Norland 13685 on the border of the cover slip, the liquid enters for capillarity.
4. Expose under UV LED for 10 minutes (this lapse depends on the UV adhesive properties).
5. Finally, remove the plastic film with the cover slip from the flat surface very carefully for then remove the food wrap from the cover slip
6. An easy polymerization quality test is to observe the shape of a water drop on the NOA layer. Due to the hydrophobicity of the adhesive, the water contact angle must be larger than 90°.

Second method: cold room

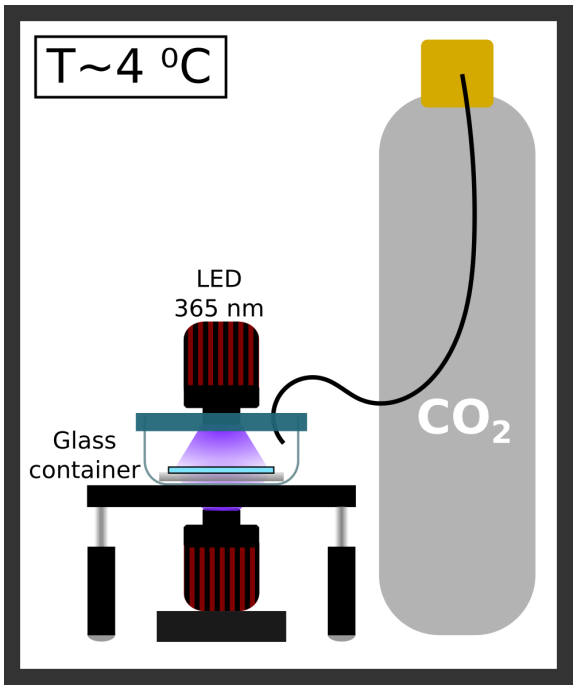

Figure 1.9. Van der Waals sign reversal layer. Experimental set-up for low-refractive index layer using NOA.

Given the chemical composition of NOA adhesives, after several trials using nitrogen (N_2) as inert atmosphere, we replaced it with carbon dioxide (CO_2). The main reasons of this change are due to the fact that CO_2 is heavier and cheaper than N_2.

As mentioned, for some NOA adhesives it is fundamental to satisfy a low temperature condition during the thin layer generation. After working inside a cold room and combining a low temperature, CO_2 saturated environment, and two sources of UV light to illuminate from above and below the sample, we developed the following protocol:

Materials

- CO_2 tank with flexible tube
- Cold room with temperature at 4°C
- Transparent glass container with a plastic lid
- Metal platform with adjustable legs for horizontal control
- Metal sample holder with magnets
- Gene frame
- Cover slip
- Norland 1315
- 2 THORLABS UV Mounted LED M365LP1
- UV protective glasses
- Bull's eye level
- 5 mm and 3 mm hex keys

Procedure:

1. Leave all the materials in the cold room allowing to reach the 4°C
2. Place a gene frame on a cover slip using the closed side of it.
3. Due to NOA low viscosity, the adhesive layer must be generated on a horizontal surface. To reach this requirement it is necessary to place a metal sample holder with magnets on the inside of the glass container and then place the glass container on the metal platform. By a bull's eye level on the sample holder and adjusting the height of the legs of the platform, a horizontal position is guaranteed (the purpose of the magnets is to interact with the metal platform and fixed the position of the sample holder).
4. The shape of the metal platform allows sample UV exposition from top and bottom at the same time, so we place bottom UV LED from the shortest distance possible to the glass container.
5. Close the glass container with its plastic lid (the cover must be modified: drill a small hole for the CO_2 flexible tube and another hole of the size of the UV LED, shortening the top LED-sample distance).
6. Introduce CO_2 flexible tube on the glass container and open the CO_2 valve tank allowing a strong flux of gas during 1 minute (in this way the air volume will be CO_2 saturated).
7. Close the CO_2 valve until just a subtle flux remains and wait for 30 seconds.

8. Put on protective glasses for UV radiation.
9. Introduce 50 μL of Norland 1315 in the center of the gene frame
10. Once NOA volume has reached the gene frame border, turn on bottom UV LED.
11. Place top UV LED on the plastic lid and turn it on.
12. Leave the sample exposed under UV LEDs for 10 minutes.
13. Then, turn off both UV LEDs and close the CO_2 valve.
14. Keep the sample on a clean box.
15. Outside of the cold room and without CO_2 inert atmosphere, it is fundamental to leave the sample under UV LEDs for 60 minutes more for ensuring a full curing.

Observations and comments for both methods

The first method is suitable for adhesives with viscosity similar to the one of water, in the cases where the UV adhesive viscosity is very high then it is necessary to first introduce the volume of adhesive in the center position where we will generate the NOA layer, and then put the cover slip above. By this method we generated layers with 8 of 9 NOA adhesives,nevertheless for those NOA with low temperature requirement, the layer presented a rough surface because of bubbles formation due to the vaporization issue.

In the case of the second method, spin coating technique was not used due to oxygen inhibition and the available small quantity of each UV adhesive. The gene frame implementation helps to reach a flatter surface in comparison with layers obtained on cover slips with no limiting frame. The reason is unknown.

Step number 15 is the result of performing several experiments in which the NOA layer was left with water for 1 day, and then discovered bubbles or spherical particles inside of NOA layer. The origin of this strange behavior can be explained by the Norland 1315 adhesive composition: if NOA layer has not been completely cured, then the contact with water will dissolve the urethane part, breaking the crosslink between acrylic chains. Fortunately, this problem is solved increasing 60 minutes the UV exposition time for NOA layer. The reason because a low temperature and an inert atmosphere are no longer required is because exposed NOA layer surface has been already cured, so oxygen will not diffuse on the inside of the material.

We tested this method by calculating the diffusion coefficient (D) for polystyrene particles with diameter of 10 μm immersed in MB, and we used substrates coated with materials of different refractive index (1.315, 1.32, 1.327, 1.328, 1.33, 1.36, 1.5). The calculated diffusion coefficients for each refractive index are presented on Figure 1.10, the red dashed line corresponds to n_{water} and $n_{glass} = 1.5$ corresponds to glass beads.

Besides this last experiment, we tested the stability of the low-refractive-index layer by using an open sample with SU-8 microstructures and bacteria on motility buffer held overnight. After 12 hours there was no adhesion of microstructures and bacteria were swimming still.

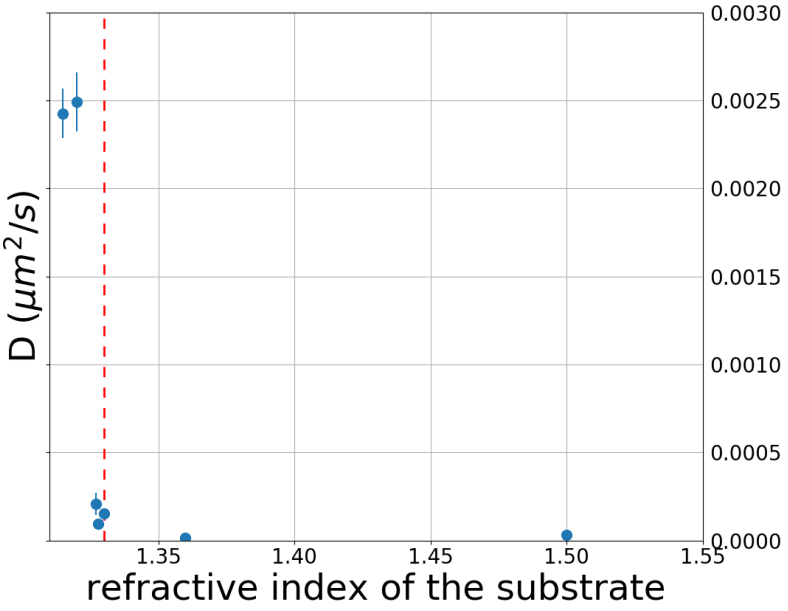

Figure 1.10. Testing low-refractive index layer. Diffusion coefficients for different coated substrates using low refractive index layers. Red dashed line indicates the value of n_{water}

1.3 Conclusions

Direct laser writing by two-photon polymerization is a three-dimensional fabrication technology which makes possible building of structures with resolution on the order of 100 nm. This resolution is defined by the smallest unit of solidified polymer that forms at the focal point of the laser beam during two-photon polymerization, thus it is important to determine the resolution of our custom built two-photon polymerization set-up. By fabricating a single line for different values of scanning speed and laser power, we measured the lateral and longitudinal dimensions of the voxel through images obtained by scanning electron microscopy. With the experimental data we obtained the expressions for both lengths as function of laser power and scanning speed. In addition, we developed a method for overcoming adhesion to the substrate, a common issue when working with free-floating microstructures. From the expression for the Hamaker constant in Van der Waals forces it is possible to generate a sign reversal if the refractive index of the substrate, medium and particle satisfied certain condition, therefore Van der Waals forces are repulsive instead of atractive. We demonstrated the feasibility of this method by measuring the diffusion coefficients for several low refractive index layers.

Part II

3D microstructures for active matter studies

Chapter 2

Bacteria as propellers

Even though microfabrication origins can be found in the manufacturing techniques of integrated circuits, the development of these strategies triggered the interest of using this fabrication approach for making smaller and smaller electrical and mechanical components. Simultaneously opened up new ways for studying the dynamics of microsystems in a very broad range of applications in microengineering and cell biology. While the immense progress in microfabrication methodologies reached in the last decades represents a huge advantage, it is crucial to understand the scaling of physical phenomenona when a system of micrometer dimensions is produced. An inadequate comprehension of the physics at the microscale will make even the simplest manipulation tasks challenging.

The design of micro-robots represents a laborious and stimulating research field mainly because the intuition developed for the macroscopic world must set aside due to the scaling of physical effects. As a result, emulating swimming strategies of micro-organisms or implementing motile micro-organisms as propellers have been the main strategies for providing a mechanism of actuation to micro-robots. In this chapter, we present a brief description of the principles for swimming at the micro-scale. We also give a summary of the mechanisms implemented by *Escherichia coli* for surviving in a low Reynolds number regime. Finally, a recent discovery of how to implement genetically modified bacteria to generate propulsion in artificial microsystems is explained.

2.1 Life at low Reynolds number and swimming strategy of *Escherichia coli*

Understanding the rules behind the movement in the microscopic world requires modifying the insight acquired in our daily macro-size world. The physics determining the swimming of a bacterium, for example, is different from the physics of a man moving in the sea. At the micro-scale, inertial forces are practically negligible while viscous forces are dominant, such a world is better known as "low Reynolds number" regime. The Reynolds number, Re, is defined as $Re = {}^{\rho UL}/_{\eta}$, where ρ is the fluid density, η is the viscosity and U and L are characteristic velocity and length scales of the flow, respectively. Re is a dimensionless quantity with several interpretations, being the ratio between inertial and viscous forces in a fluid the classical one [62]. But, how can we tell when Re is small? Using the definition of Reynolds number for different organisms gives the answer: consider different bodies moving trough a liquid, the density and viscosity in the case of water are $\rho \sim 10^3\ {}^{kg}/_{m^3}$ and $\eta \sim 10^{-3}\ Pa \cdot s$, respectively. Therefore, for a human swimming in a pool $Re \sim 10^4$, while for a goldfish it might get down to 10^2, and finally, in the case of microorganisms like *Escherichia coli* Re is about 10^{-4} or 10^{-5} [81].

For unraveling the dynamics of objects swimming at the micro-scale it is essential to study the force distribution on the microorganisms. We thus need to solve for the flow field $\mathbf{u}$ and pressure p in the surrounding fluid. In the case of an incompressible Newtonian fluid with density ρ and viscosity η, the flow satisfies the Navier–Stokes equations [62]

$$\rho\left(\frac{\partial \mathbf{u}}{\partial t} + (\mathbf{u}\cdot\nabla)\mathbf{u}\right) = -\nabla p + \eta\nabla^2\mathbf{u}, \qquad \nabla\cdot\mathbf{u} = 0 \tag{2.1}$$

in addition to the boundary conditions applicable to the problem in question. In the case of *E. coli*, having such a small Re allows to study the limit of $Re = 0$, for which the Navier-Stokes equations (2.1) simplify to the Stokes equations

$$-\nabla p + \eta\nabla^2\mathbf{u} = 0, \qquad \nabla\cdot\mathbf{u} = 0. \tag{2.2}$$

The time independence and linearity of Stokes equations generate two important properties of locomotion at low Reynolds number [81]. The first one is rate independence: the distance travelled by a swimmer that undergoes surface deformation does not depend on the configuration change rate, but only on its geometry (i.e. the sequence of shapes the swimmer passes through between these two configurations). The second important property of swimming with negligible inertia is the so-called scallop theorem: if the sequence of shapes displayed by a swimmer deforming in a time–periodic fashion is identical to its time-reversed version, then the swimmer cannot move on average [62]. The main implication of the last theorem is excluding "reciprocal deformation" as possible locomotion mechanism. Nevertheless, through evolution microorganisms have developed several locomotion strategies to overcome the limitations imposed by their environment. For instance, many microscopic swimmers employ one or more appendages for generating propulsion. In the case of *E. coli*, the appendage is a relatively stiff helix with a corkscrew-like rotation.

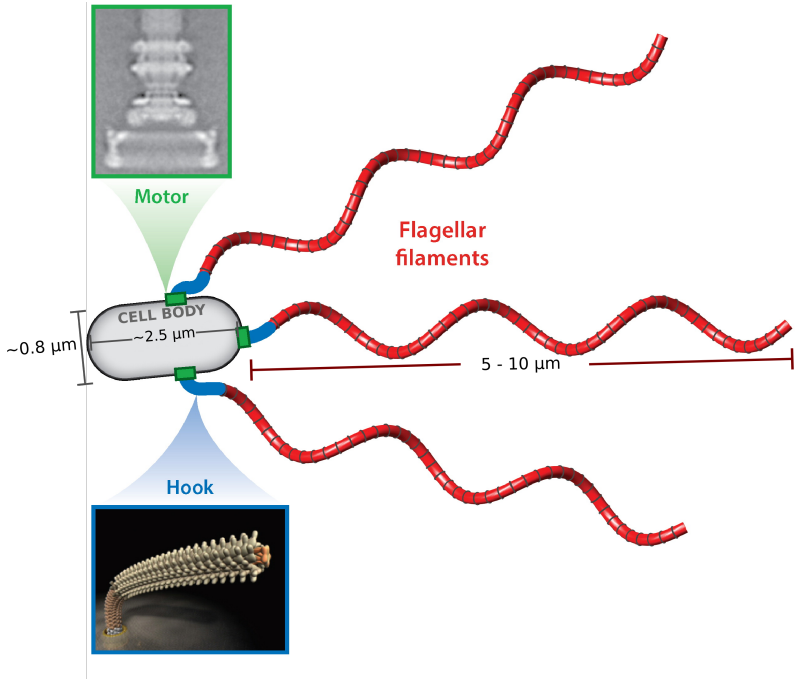

Figure 2.1. *Escherichia coli* features. Schematic representation of a bacterium with three flagellar filaments, a bacterial rotary motor embedded in the cell wall is shown in the upper inset, while a hook with its junction to a flagellar filament is presented in the lower inset. The cell body of *Escherichia coli* is rod-shaped an has an approximate length of 2.5 μm and a diamenter of about 0.8 μm. The bacterium propels itself by the rotating of a bundle formed of flagella; the range of filaments length varies from 5 μm up to 10 μm. Modified from [60].

The swimming mechanism of *E. coli* consists in rotating a bundle formed by 4-5 flagella which are randomly distributed on the cell surface. Bacterial flagellar filaments are helical polymers made of a single protein named flagellin (FliC), with a cap composed of another protein, FliD [54]. The features of a single flagellum consist in a variable length from 5 μm to 10 μm, and only 40 nm in diameter. Each filament is attached to a short flexible hook with approximately 60 nm in length (upper inset in Figure 2.1) which acts as a universal joint. The hook is turned by a bacterial rotary motor which works in a stepper fashion driven by a proton flux (lower inset in Figure 2.1) [119].

With the purpose of having a deeper comprehension of bacteria, it is essential to understand the internal structure and functioning of the bacterial flagellar motor. This bionanomachine is built by about 20 proteins and extends across the outer membrane, passing through peptidoglycan wall and the inner membrane, reaching into the cytoplasm. The structural constituents of this rotary motor can be divided into two categories: the rotor and the stators (Figure 2.2). The rotor is composed by four concentric protein rings connected to a rod in their center, each ring is named in correspondence with its location on the membrane: L-ring sits at the lipopolysaccharide outer membrane; P-ring is located at the peptidoglycan cell wall; MS-ring denote membrane and supramembrane ring; finally, the C-ring is in the cytoplasm, mounted on the MS-ring. Instead, the stators are located around the

periphery of the rotor, producing a larger concentric protein ring outside the MS-ring [119].

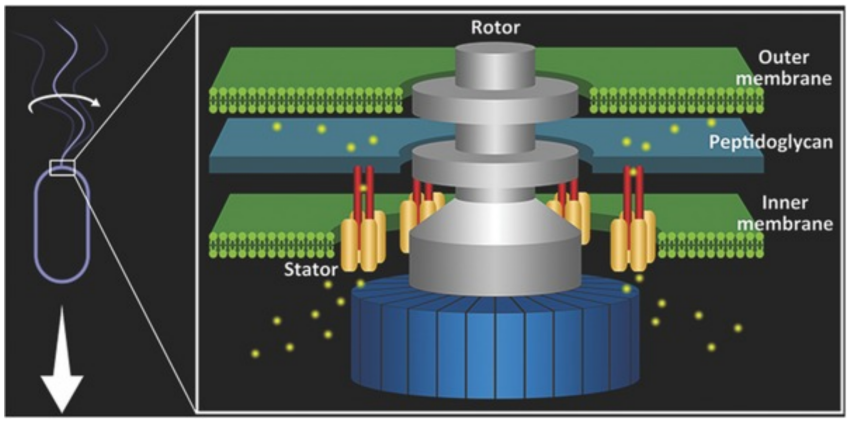

Figure 2.2. Bacterial flagellar motor. A marvelous nanomachine embedded in the cell envelope generates rapid rotation of the flagellum ($\sim 100Hz$) by harvesting the free energy of ion flux across the cytoplasmic membrane. From [119].

By the precise coordination of the motion of numerous proteins, the bacterial motor generates the propulsion in bacteria. Despite the nano-scale of the bacterial motor it bears some resemblance with macro-engines, like the use of repeating cycles, however due to its size it is subject to the principles of low Reynolds number regime. Thus, given that viscous forces dominate over inertial forces, a microscopic object halts its movement if the driving force or torque is withdrawn. Another consequence of the micro-world is Brownian motion which provides a stochastic force capable of causing molecules to pass over high energy barriers, a non feasible situation in the macroscopic world.

The main difference between most linear molecular motors (such as myosin on actin filaments[17], or kinesin and dynein on microtubules[18]), and the bacterial flagellar motor is the power mechanism. In the first case, the mentioned motors are powered by adenosine triphosphate (ATP) hydrolisis, while the bacterial flagellar rotatory motor is powered by protons moving down an electrochemical gradient. The work per unit charge generated by a proton passing through the cytoplasmic membrane is called the proton motive force (PMF), Δp in Eq. (2.3). In general, PMF consists of two terms: the first component due to the transmembrane electrical potential difference, or the membrane potential $\Delta\Psi$, and the second part is proportional to the transmembrane pH difference, $\Delta\mathsf{pH}$:

$$PMF = \Delta p = \Delta\Psi + 2.3\frac{k_B T}{e}\Delta\mathsf{pH} \tag{2.3}$$

where k_B is the Boltzmann's constant, T the absolute temperature, and e the proton charge. By convention, $\Delta\Psi$ is the internal potential minus the external potential, and $\Delta\mathsf{pH}$ is the internal pH minus the external pH.

The bacterial motor can rotate in two different directions, counterclockwise (CCW) and clockwise (CW), when viewed from behind the cell. If all motors on *E. coli* turn CCW, then the bundle is formed allowing to push the cell steadily forward,

this smooth segment of the movement is known as "run" state; when one or more of the motors redirect to spin CW, the flagellar bundle breaks causing the cell to tumble randomly, these erratic intervals are known as "tumbles" [13]. From a 3D tracking experiment of single bacteria it was observed that, in isotropic solutions, the mean run and tumble intervals are well described by exponential distributions with characteristic times of $\tau_{run} \sim 1\ s$ for runs (this time slightly changes from cell to cell) and $\tau_{tumble} \sim 0.1\ s$ for tumbles (same value from cell to cell) [14]. Aided by this strategy peritrichous bacteria such as *E. coli* are able probe their environment.

2.2 Swimming near surfaces: *E. coli* circular trajectory

Even though the general methodology of studying and cultivating bacteria in a laboratory is through cell suspensions in liquid media, the natural environment of bacteria involves a wide variety of surfaces available for their attachment and colonization. Thus, understanding the influence of surfaces on the behavior of bacteria represents a fundamental research field for several phenomena such as biotechnology, biofilm formation, biofueling, among others[110]. For the purpose of this thesis, instead of broadening in the bacterial adhesion process, we will address the repercussions of surfaces on the swimming movement of *E. coli* presenting a summary of the main results obtained in several studies.

As described in the previous section, *E. coli* cells in solution move in a random walk fashion, alternating straight swimming trajectories with short time movements for reaching a new direction. However, when *E. coli* cells move near a rigid surface, their trajectories become circular. In one of the initial studies regarding this topic, it was measured the diameter of the circular motion of a smooth-swimming strain of *E. coli*[7] (i.e. nontumbling), obtaining a value of the order of 25 μm for the radius of curvature[16]. In said study, the swimming direction was CW when viewed from above, which was expected, because the flagellar bundle rotates CCW while the cell body rotates in the CW direction. In addition to the presence of a solid surface, if other variables are considered and modified then the radius of the circular trajectory of *E. coli* will be altered. For instance, producing an increment in the temperature of a bacterial suspension (temperatures above $34°C$) generates circular curves for the motion near a glass slide, and increases the values of the radius ($\sim 10 - 50\ \mu m$)[71]. In other studies, by use of a tracking microscope[42, 41], the authors described the trajectories for wild-type and smooth-swimming cells moving near a glass surface demonstrating, again, that bacteria follow a circular path. In addition, they noticed that if the distance between the boundary and the cell diminished, then the swimming speed followed the same trend. Another astonishing discovering was related with the time employed by each type of strain near the surface, quoting the authors: "wild-type cells swim in circular paths when moving adjacent to a surface and often leave the surface after tumbling, whereas smooth-swimming cells swim along the surface much longer"[42]. Due to the spatial resolution of the tracking microscope ($\pm 2\ \mu m$), in these former works it was not possible to have a precise measurement of the distance between the surface and the cell. It was in other studies[111, 112] that the origin of attraction between the swimming bacteria and solid surface was addressed. Besides, the authors manage to establish that the distance to the surface

is of the order of tens of nanometers. Furthermore, it was found that standard DLVO theory (developed by Derjaguin, Landau, Verwey, and Overbeek) could not explain the characteristic of the cells to stay near the surfaces, but that some other force remained unidentified. Based on their observations, they proposed that the extra force is the result of a hydrodynamic effect, and they developed a conceptual model where, depending on the distance to the surface, it was possible to identify 3 different outcomes on the cell: no effect, only the hydrodynamic effect, or both the hydrodynamic and the physicochemical effects on the surface[112].

In 2006 Lauga *et al.* [61] published one of the most famous works where they present a hydrodynamic model for *E. coli* swimming near solid boundaries. The authors model is shown in Figure 2.3, where the bacterium is represented as spherical body (of radius a) connected to a single, left-handed rigid helix, the center of mass of the body is positioned at a distance d above a solid surface; between the rigid surface and the cell body there is a liquid gap of height h. Then, the position of the cell is assumed to be parallel to the surface pointing in the y direction. For the parameters of the helix the authors assumed a thickness of $2r$, wavelength λ, radius b, and a number n of wavelengths alongside of the helix, in order to have a total length of the helix $L_{\parallel} = n\lambda$. As it was mentioned in the previous section, the bundle rotates in the CCW direction (seen from behind of the bacterium), thus its angular velocity relative to the body can be written as $\omega = -\omega \mathbf{e}_y$, where ω has a positive value. For the bacterium, the instantaneous velocity and rotation rate (measured from the center of the cell body), are denoted by $\mathbf{U} = (U_x, U_y, U_z)$ and $\mathbf{\Omega} = (\Omega_x, \Omega_y, \Omega_z)$, respectively.

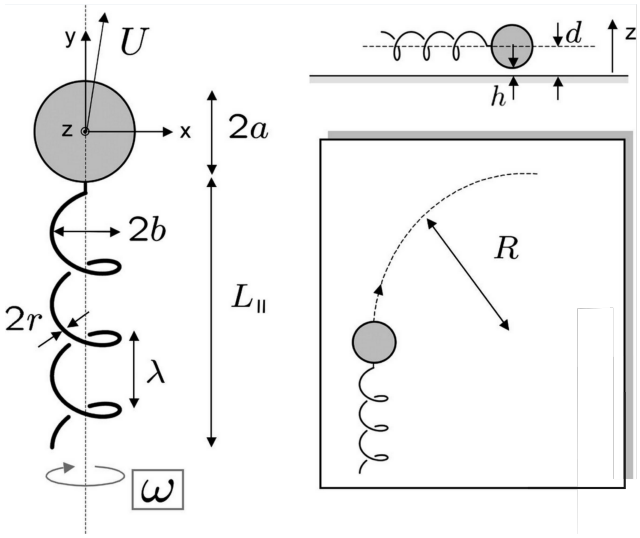

Figure 2.3. Modeling *E. coli* swimming near a rigid surface. Representation of the mechanical model for *E. coli* swimming near a solid surface. The notations regarding the variables for the model are included. Picture taken from [61].

When a bacterium is near the surface, the cell body rotates around the y-axis in a CW direction, as a consequence there is a viscous force acting on it in the x-direction (to the right in the inset of Figure 2.3). Correspondingly, the bundle of flagella is also subjected to a net force in the x-direction (force induced only by the

presence of the wall). Due to the helical shape of the bundle, some of its parts are placed closer to the surface than other parts located further away. Because the local drag coefficient on an elongated filament decreases as the distance from the nearby surface is increased, on the sections of the bundle that are close to the surface there will be acting a larger local viscous force, compared with the hydrodynamic force on the portions of the helix located further away from the surface. As the bacterial bundle rotates in a CCW direction around the y-axis (seen from behind), the parts of the helix closer to the surface move with a positive x velocity, which generates a net viscous force with negative value acting on the bundle (a force pointing to the left in the inset of Figure 2.3). The net effect of these forces is a wall-induced moment acting on the cell. Because the cell is torque-free, it needs to rotate (here, CW when viewed from above), leading to circular trajectories [60].

2.3 Proteorhodopsin: light-controlling speed on *E. coli*

Chemotaxis is the biased motion of an organism for the sake of finding the best environment, i.e., it will move forward when conditions are identified as attractive and/or it will withdraw if the surroundings are found repellent. As it was mentioned before, far from a rigid surface the motion of flagellated bacteria such as *E. coli* is composed of two parts: run and tumble. The corresponding time spent by a bacterium on each part is very different, tumbles last a fraction of second, while runs tend to have a very variable duration, reaching up to several minutes. Nevertheless, even though the time in tumbles is very short it is enough to generate a random direction for the next run. Due to the dimensions of *E. coli* (some microns long) they are unable to measure gradients concentration differences by comparing head surroundings with the tail conditions. Alternatively, they implement a kind of memory in a way that comparisons between the current and the past chemical environment are possible. When the bacterium recognizes that its environment is deteriorating (a reduction in the attractant concentration or repellent concentrations increase) the tumbling rate is enhanced. On the contrary, when cells perceive that conditions are improving, they do not tumble and keep running. Therefore, when a bacterium runs up a gradient of attractants or down a gradient of repellents it tends to continue on course [116].The chemosensory pathway of bacterial chemotaxis depends on Che proteins and interacts with the motor via the response regulator protein CheY [4]. The deletion of CheY allows the creation of a mutant strain in which tumbles are suppressed. These bacteria are commonly named smooth-swimmers [118].

While the use of chemical stimuli to control the movement of bacteria has been extensively studied since the sixties [1, 15, 118, 29], in the following decades the employment of a wide range of different stimuli has been explored for an analogous objective to chemotaxis: cause a directional motion or “-taxis”. Bacteria have been shown to respond to the following stimuli: move along the vector of an electric field (electrotaxis or galvanotaxis) [2]; react to variation in oxygen concentration (aerotaxis) [105]; sense a magnetic field and direct movement as a reaction (magnetotaxis[1] [23]);

[1]The term is commonly applied to bacteria that contain magnets and are physically rotated by the force of the earth’s magnetic field. In this case, the "behaviour" has nothing to do with

migration along a gradient of temperature (thermotaxis) [77]; and the response to variation in light intensity and direction (phototaxis) [6]. Using light as a physical stimulus for controlling bacteria exhibits advantages in comparison with others cases. For example, light patterns can be generated spatially and temporally with a high degree of control by the implementation of optical instruments as spatial light modulators (SLM), and digital micromirror device (DMD), such a precise control of the environmental conditions for the mentioned stimuli can be hard to manage spatially.

As a consequence of evolution, phototrophic bacteria have developed a wide variety of photosensory proteins to respond to light, the dominating stimulus in their environment. Not long ago, these proteins were considered an exclusive and exotic characteristic of phototrophic bacteria, nevertheless, with the advances reached in genome sequencing during the last decades, it has been confirmed that chemotrophic bacteria contain a multitude of genes that encode photosensory proteins [109]. Photoreceptors are signal-transduction proteins with a specific region where light absorption is activated, known as chromophore. Light in the visible spectrum stimulate the photoreceptor, inducing its conformational change and then initiates a flow of downstream events resulting in the signal transduction. Most of these photoreceptors can be classified in six well-defined families: rhodopsins, phytochromes, xanthopsins, cryptochromes, phototropins, and BLUF proteins. A characteristic chromophore (or a different photochemistry) is correspondent to each of these families [108].

Over the last few years, a new research area has appeared from the intersection between biology and engineering: synthetic biology [12, 5, 122]. This cutting-edge field endeavors the design and assembling innovative biological components, with the purpose of extend or modify the behavior of organisms and engineer them to perform new tasks. The use of modern tools such as DNA synthesis and editing, allows to extend the response of *E. coli* to light-stimuli by introducing exogenous genes coding for photoreceptors, i.e., genes that originally belong to different organisms. A marvelous example of synthetic biology was presented in 2005 by Levskaya *et al.* [65] when they created a functioning light sensor in *E. coli* by engineering a chimaera that uses a phytochrome from acyanobacterium, generating bacteria capable of "seeing light".

Beyond phototaxis, bacteria are able of display another photosensory motor response. Photokinesis describes the dependence of speed on light stimuli. In this case the direction of the light beam is irrelevant and the organisms detect the absolute, steady-state irradiation [53]. At one time the only known strategy for bacteria to harvest energy from light was via photosynthetic centers. After the groundbreaking discovery of the light-powered proton pump proteorhodopsin (PR) in 2000 [11] (PR is the analogous protein to bacteriorhodopsin[100] for Bacteria which was initially thought to be confined within Archaea [40]), the vision of the process by which sun energy is captured and converted into chemical energy (phototrophy) in bacteria was transformed. It paved the way for further studies establishing that this phototrophy alternative mechanism is significantly common in marine bacteria [43]. Additionally, PR may be correctly folded in *E. coli* membranes, contrastively to bacteriorhodopsin, another light-powered proton pump [10]. Moreover PR extracted

sensation and the bacteria are more accurately described as "magnetic bacteria". [36]

from different bacteria show to have different absorption spectrum [59], revealing the possibility of tuning the excitation wavelengths depending on the use. On account of these characteristics, PR is an ideal tool for a wide range of applications in synthetic biology.

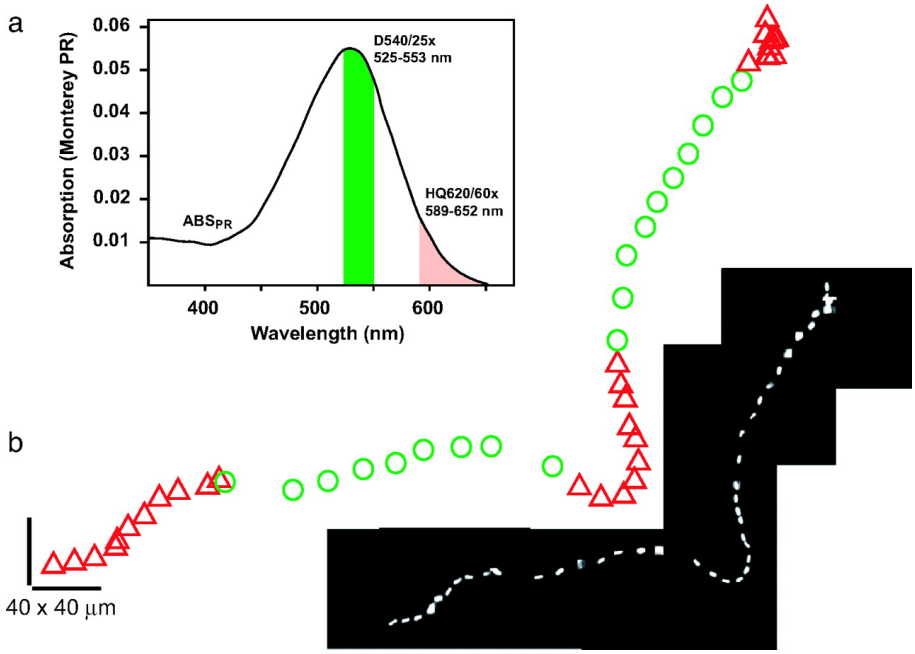

Figure 2.4. Effect of green light on PR+ *E. coli*. (a) Outline of spectra and spectral overlaps. Black corresponds to PR absorption spectrum, while green and red bars indicate illumination wavelengths. (b) Single PR+ bacterium swims faster when illuminated with green light. From [115].

On a study from 2007 the authors were able to use PR expressing (PR+) *E. coli* cells to power its flagellar motor by absorbing light [115]. In previous studies it has been shown that speed of the flagellar motor is proportional to the PMF [44], thus, under light illumination, the outer proton flux created by PR can power the rotation of the flagellum when H+ re-enter the cell through the motor. Walter *et al.* [115] demonstrated that the flagellar motor speed can be controlled by means of green light (532 nm) in single smooth-swimmer cells PR+, tethered on a glass slide in an environment where the PMF could not be maintained by oxidative phosphorylation. The authors inhibited respiration using azide, on Figure 2.4b they show that single bacterium velocity during illumination with green light increased 96% in comparison with the periods of red illumination.

A marvelous illustration of implementing photokinetic bacteria PR+ was presented very recently. Vizsnyiczai *et al.* [113] demonstrated by modulating the intensity of green light the speed of micromotors fabricated by two-photon polymerization can be controlled, this as a consequence of using a genetically modified strain of smooth-swimmers expressing PR. They reached separately tuning of the speed of the microstructures by adjusting their illumination levels with a SLM. On figure 2.5(a) the rotational speed of only 5 microtors from the array shown in 2.5(b) was obtained by lowering the illumination power. Thus, this study [113] is a brilliant

display of the capability of modified bacteria to induce forces on movable structures.

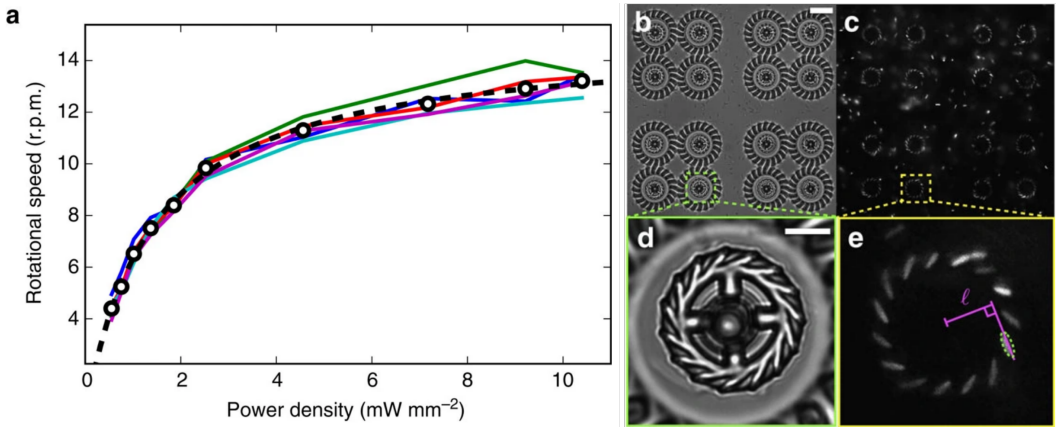

Figure 2.5. Light controlled 3D micromotors powered by bacteria. (a) Rotational speed of 5 micromotors obtained by changing the illumination power. (b,c) 16 rotors array used for the rotational dynamics characterization. Cell bodies are visible in the fluorescence image (c). The scale bar is 20 μm for both (b,c). (d,e) Magnified view of a single rotor shown in b,c. The scale bar is 5μm for both d,e. Modified from [113].

What if instead of moving a fixed micro-object we would like to exploit the same principle in [113] but using a free-standing and free- moving microstructure? What kind of conditions and how complex they could be to reach this aim? We will find an answer to these questions through the upcoming chapters.

Chapter 3

Light-driven biohybrid microshuttles

The work on this chapter was influenced by previous works from Gaszton Vizsnyiczai. In the case of section 3.5 the design of the microstructure was originally created by Gazston Vizsnyiczai.

The design and fabrication of micro-robots has been a very active research topic in the last decades. Integrating the ability to perform power, actuation and sensing on micro-scale robots have evolved at an incredible pace in the last fifteen years, principally as a consequence of the reached advances in fabrication techniques. Based on the different mechanism of microrobots[1], we find a number of existing approaches to microrobot mobility in the literature for motion in two dimensions and three dimensions: chemical propulsion, swimming microrobots, magnetic gradient pulling and byohibrid cellular microrobots [94].

Microrobots working under chemical propulsion are self-propelled and use available chemical energy present in their environment to power the motility, sensing and other functional capabilities [24]. Some examples of this kind of micro scale robots are microtubular jet microrobots [95], electro-osmotic microswimmers [52], and catalytic micro/nanomotors [35]. Generally, one of the disadvantages of chemical control methods is the poor temporal resolution. In addition, they are characterized by a relatively large stochasticity.

In contrast, swimming microrobots arise from the imitation of bacteria, e.i., use a flexible flagella to generate propulsion by helical rotation, which is an optimized strategy for both propel and change direction. On this category we find the colloidal magnetic swimmer [34], the magnetic thin-film helical swimmer [120], the microscale

[1]Many robots usually consist of sensors and actuators, a control unit, and an energy source. Depending on the arrangement of these components, there is a possible classification of microrobots according to the following criteria: locomotive and positioning possibility (yes or no), manipulation possibility (yes or no), control type (wireless or tethered), and autonomy. For more information regarding this categories consult reference [76].

magnetic helix fabricated by glancing angle deposition [46], the helical microrobot with cargo carrying cage fabricated by direct laser writing [107], among other synthetic microswimmers. As seen, the mentioned swimming microrobots function by magnetic actuation. In the case microrobots pulled in 3D using magnetic field gradients (like the MRI-powered and imaged magnetic bead [73]), even if the strategy for remote control offers several advantages in comparison with the catalytic micromachines, there are some issues that interfere with their performance. The use of magnetic control for steering a microrobot deep inside the body implies the application of very high magnetic field gradients due to the exponential decay with the distance presented in this kind of forces, producing heat and damage in the tissues. Furthermore, another possible problem is the requirement of expensive magnetic instrumentation for this kind of microrobots.

In the case of chemical and magnetic actuation, along with bio-inspired microrobots, their components are made using polymers, magnetic particles, and metals, i.e., artificial materials. Besides, another common characteristic of these systems is the lack of inter-componential communication and control. Micromachineries with sophisticated internal communication can be found in nature, e.g., bacteria and spermatozoa, microorganisms that have evolved through millions of years to developed robust and adaptive mechanisms for surviving in their environment. The incorporated machines in this organisms are continuously taking the available chemical energy in their environment and transforming it into mechanical work, furthermore, they can modulate the power output as a reaction to forces, stimuli, and chemicals in their surroundings. Therefore, a biohybrid microrobot indicate the physical combination of single cells or a film composed of such cells and synthetic materials in a way that, as an entity, the microsystem is able to exploit the sensing and power capabilities of the cells. This process of hybridization may enable complex microrobotic tasks to be managed in a fully autonomous way.

Escherichia coli is an optimal organism to provide propulsion for an hybrid microsystem. The motors embedded on the cell wall are connected to stiff helical protein filaments called flagella whose rotation generates thrust through viscous drag. Due to the highly sophisticated functioning of the flagellar motor, the combination of bacteria and synthetic microstructures to generate self-powered microrobots has been used previously. In 2007, Steager *et al.* [98] were able to displace a microstructure by releasing it on the surface of swarming *Serratia marcescens* bacteria. More recently, employing the same type of bacteria, the authors of [99] demonstrated the rotation control of a squared microstructure by means of bacteria attached to the surface and by electrical stimulus. In another work, Stanton *et al.* [97] used electropolymerized microtubes with interior surface functionalization, allowing to partially trapped a single bacterium. Microtubes are modified with magnetic components for external guidance using magnetic fields. While in the last two studies there is a significant movement of microstructures, the steering strategies expose some disadvantages. The use of magnetic and electric fields for controlling the direction of the microrobot represents a limitation in time and space, besides, finding a method not involving surface modification can simplify the experiments.

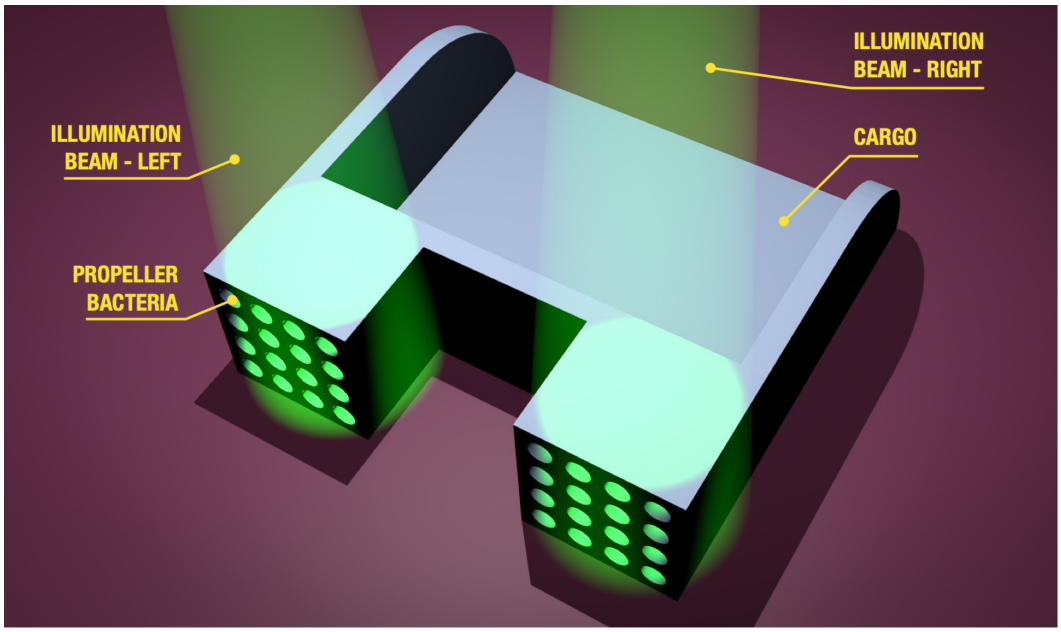

Figure 3.1. Microshuttle. Scheme of a structure designed for been propel by *E. coli* bacteria. The size of each cavity allows the entrance of a single bacteria.

Following this last approach but considering light as the control signal, we propose a new biohybrid microrobot shown in Figure 3.1. The use of light patterns for steering the microstructure give us the advantage of guide the structure smoothly in space and time. On the other hand, in our model it is not necessary to develop surface functionalization on the synthetic part of the microrobot, and finally we can control the precise number of cells on the inside of the microshuttle. We used light-driven *E. coli* cells, where the bacterial flagellar motor converts light into motion, and we fabricated several microstructures by two-photon polymerization technique, incorporating a defined number of bacteria which act as propeller unities. Due to the fact that the speed of bacteria can be regulated by their response to the light intensity, we also expect the motion of the microstructure to be similarly controllable.

3.1 Basic design: *coli*-house

Using bacterial power as the propulsion strategy for a microstructure implies addressing several challenges in the way of the realization of this idea. Among the possible issues in this project we can find: design of the microstructure, incorporation of bacteria on the microrobot, using chemical or optical modifications to the environment facilitating bacteria to enter in the shuttle, and influence of surface forces in the free movement structure, just to mention some. By overcoming each one of the emerging problems, we will describe the evolution of our microrobot into the final microshuttle.

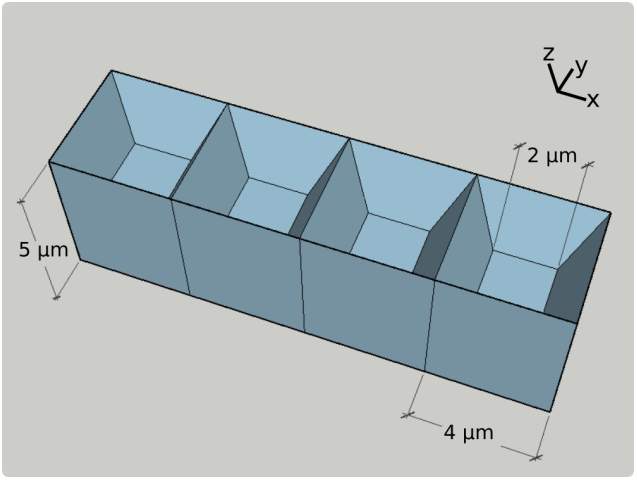

Figure 3.2. 3D model of the first microshuttle design. The microrobot consists of four *E. coli* microchambers joined side by side. The internal side length of the microchamber is 2 μm, while the external side length is 4 μm, and the external deepness including the ramp is 5 μm.

The very first design for our microshuttle is a basic model. Considering the dimensions of *E. coli*, we started with a box-type microchamber with enough space for a single bacterium to enter: square intern shape with length side of 2 μm, external length 4 μm, and an external deepness of the microchamber of 5 μm; with the purpose of facilitating the entrance of the cell, we implemented a short ramp on each side of the compartment which inclination was $\theta = 35°$. The whole microrobot consisted of 4 single microchambers joined side by side. As shown in Figure 3.2, the microstructure was fabricated in a vertical position with the aim of obtaining a smooth transition on the border of each microchamber entrance. It is important to highlight that each microchamber features were designed to leave the entire flagellar bundle outside for maximal propulsion.

By means of the SLM in the two-photon polymerization experimental set-up generating multiple fabrication foci is straightforward, hereby making possible to build several structures at the same time. The parameters used for the first model, that we called *coli*-house, were a laser power of 2 mW or 2.5 mW per focus and a scanning speed that varied between 60 and 100 $\mu m/s$. Because we needed to detach the microrobots from the surface[2], the microstrutures were fabricated on a sample where only SU-8 photoresist was spun following the process mentioned in section 1.2.2. After development, rinsing, and drying, the microstructure were detached from the glass substrate using a pulled glass pipette controlled by a micromanipulator[3].

For the experiments we used an open sample, using UV adhesive, we fixed a plastic ring (with a diameter of $\sim$ 2 cm and height of $\sim$ 1 cm) on the coverslip, placed around the microstructures. In the detachment microrobots process we used

[2]At the beginning of this project thesis the protocol for the water-soluble sacrifitial layer used for free-floating microstuctures had not been developed yet.

[3]The first trials of *coli*-house fabrication were done using samples with one layer of Omnicoat to improve adhesion, and thus ensure finding the microstructures after development. Nevertheless, once we attempted to detached the microrobots, they were damaged or some residues of Omnicoat remained attached to the free microshuttle. Therefore, we chose to use samples only with SU-8

400 μL of a solution composed by motility buffer (MB) for bacteria with Tween 20 at a concentration of 0.2%. Once we had several microstructures detached from the glass substrate, we added 50 μL of a dense solution of HCB437 smooth-swimmer bacteria [118] (optical density (OD) not measured) at a long distance from the free microrobots. The microstructures were observed using bright field illumination on a custom-built inverted optical microscope equipped with a 20x (NA 0.50), 10x (NA 0.30) or 4X(NA 0.13) objectives.

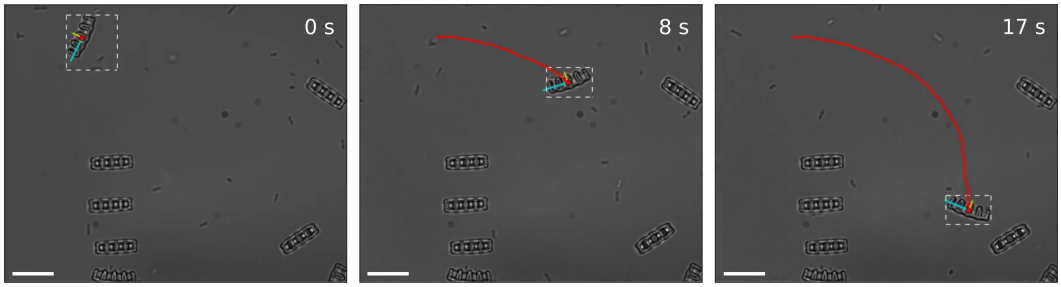

Figure 3.3. *Coli*-house propelled by four bacteria. Tracking of a 17 seconds video recorded using bright field illumination for a *coli*-house microstructure with the 4 michochambers filled with a single bacteria. The scale bar is 15 μm.

A tracking algorithm was coded in Python Programming Language to analyze the motion of the geometric centroid. Video frames were captured, digitized and imported for analysis. First, through the edge contrast effect of the SU-8 microstructure we determined the region of interest for the shuttle by means of a threshold level. Then, we calculate the image moments (image moments are defined as weighted averages of the image pixels intensities) up to second degree, then, for each frame, we calculated [87] the coordinates of the center of mass and orientation by solving the covariance matrix of the second degree image moments. The next step was write this information to a data file for posterior analysis to obtain the trajectory of the microrobot as well as its velocity by another Python code. An example of the tracking microrobot of one video of 17 seconds is shown in Figure 3.3 while the results from the data analysis are shown in Figure 3.4.

From the results we observe two important features of the microshuttle movement. The first characteristic is related with the average speed, due to the configuration of the microchambers and the fact that our microstructure is propelled by four bacteria, considering that the mean speed of a single cell of *E. coli* is $\sim 20\ \mu m/s$, the value for the microrobot average speed is expected to be of the order of the value of a single cell, instead, we obtained a speed of $4.7\ \mu m/s$. Among the causes of this significant reduction in the speed of the microshuttle there are the surface forces which attract the SU-8 structure to the glass substrate stalling its free movement; another potential factor is a largest microchamber deepness such that the flagellar bundle is not completely outside of it, therefore, the maximal propulsion is not reached. The second characteristic is circular motion. As it was explained in the last chapter, whenever a bacterium swims near a rigid surface its trajectory will follow a

circular path[4]. A possible solution to this issue is to modify the distance between the surface substrate and the closest side of the microchamber to the surface until finding the optimal value for minimizing the circular trajectory.

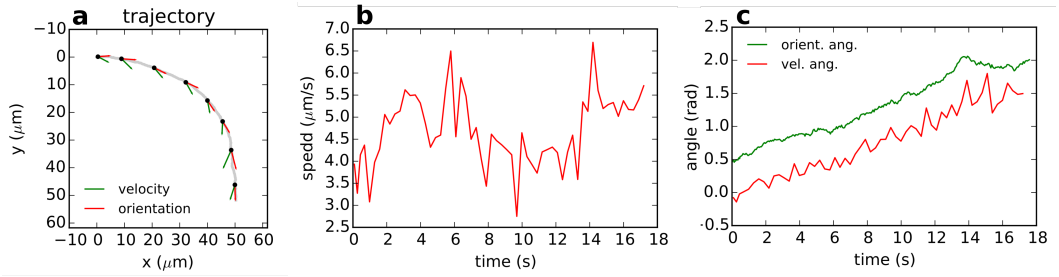

Figure 3.4. Results from the tracking of the *coli*-house video. **(a)** A circular trajectory is followed by the microstructure. **(b)** Values of the speed for the microshuttle. **(c)** Angle of the orientation and angular velocity of the microrobot.

For the following experiments, some modifications were made to overcome the mentioned issues. Regarding the small mean speed of the microstructure we decided to use a different strain of smooth-swimmers and implement fluorescent bacteria, this allows to verify the microchamber size avoiding flagellar bundle blocking. About the correction of the circular trajectory, we decided to include a ramp on the floor of the next design for the microshuttle, in a way to increase the distance between the bacteria and the substrate surface.

3.2 Including ramps in the shuttle

The initial design for the microshuttle was modified after evaluating the results obtained from the *coli*-house microstructure experiments. These modifications include integration of a ramp on the bottom plane of the microrobot, and developing a multilevel design in order to increase the number of propellers to self-assembly on the microstructure. Both adjustments would allow to generate a power propulsion enhancement in the microshuttle.

[4]Although we observed the microstructures from below the substrate (using an inverted optical microscope), we obtained CW. This is due to a reflection in the optical path focal plane-camera where the image is captured.

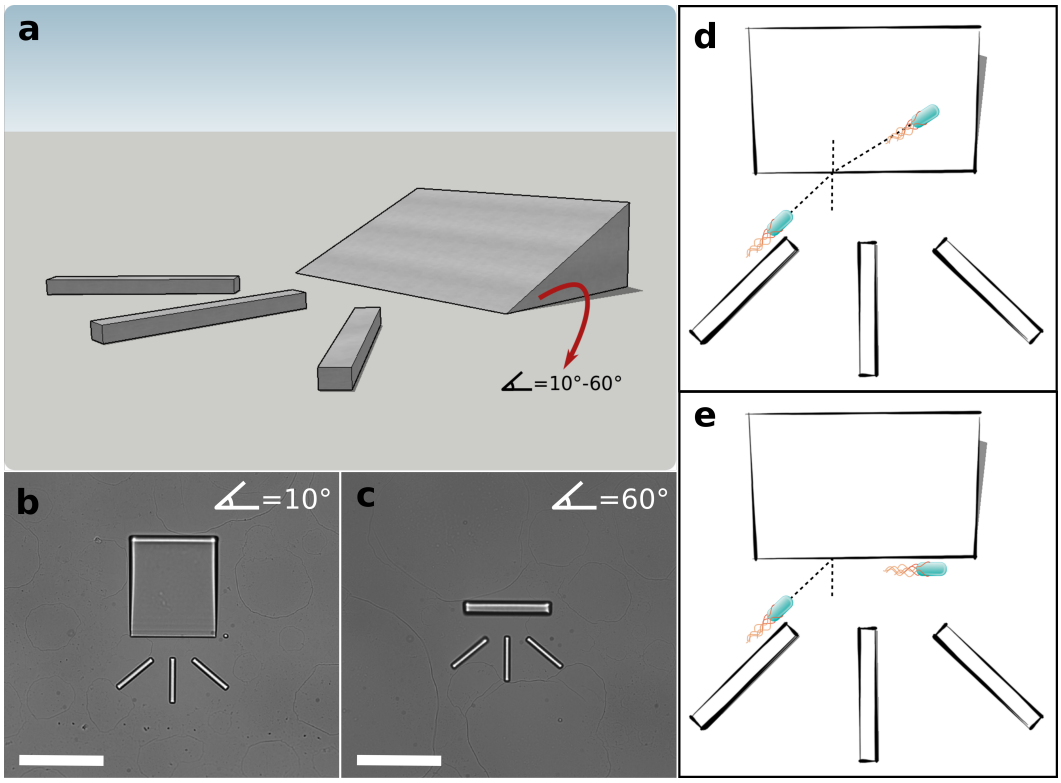

Figure 3.5. Ramp experiments. **(a)** 3D model of the microscopic ramp, the design includes 3 barriers functioning as guides for directing bacteria to the incline surface. **(b)** Bright field image of a ramp with inclination at 10°. **(c)** Bright field image of the ramp with the highest inclination, 60°. In both cases, the scale bar is 40 μm. **(d)** Scheme of one bacterium moving trough the ramp. **(e)** Second scenario for the behavior of bacteria, in this case the surface inclination is so very steep, so bacteria move on the border of the structure.

With the purpose of implementing a grade in the microstructure, first we needed to characterize the value of the optimal angle to tilt the surface. Moving on this direction, we planned to fabricate several ramps where the value of the slope varied between 10° and 60°. In addition some guides would be fabricated in front of the ramp, so bacteria would be directed to the base of the microstructure easily. On Figure 3.5a a model of the microramp is shown as well as the guides. Figure 3.5b and c are bright field images captured by the same custom built microscope used in the last section and correspond the minimal and the maximum ramp inclination, respectively. The possible scenarios for each ramp is shown in Figure 3.5d and e. In the first case, the ramp allows a smooth transition from the substrate to the microstructure, while in the second one the bacterium transition to the ramp is interrupted because the surface angle is too steep and the cell moves alongside the border.

During the process of the ramp microfabrication, there were some difficulties regarding the detachment of the thinnest part of it, specifically in the case of the larger ramp with the smallest angle. After several trials, the microstructure separation from the substrate was ascribed to thermal stress subsequent to the

post-exposure bake of the sample. Initially, the second bake of SU-8 was performed for 7 minutes at 95 $°C$, followed by 1 minute cooling, and then we continued with the development. Due to the mismatch between the coefficients of thermal expansion of glass substrate and SU-8, it is necessary to increase and lower the temperature gradually. Once we started to apply a temperature ramp both when heating and cooling the sample, then we improved the attachment of the ramp to the glass, avoiding thermal stress.

After overcoming the detachment issue, the measurements were performed in an open sample made in the same way as in the previous section, and consisted in recording bright field illumination videos of microstructures immersed in a solution of smooth-swimmers bacteria and MB. To facilitate tracking the bacteria were captured slightly above the focal plane. In this configuration, the cell bodies produce bright blobs which were easily tracked using a center of mass algorithm. Base on the results (data not shown), we determined that angles smaller than 40° enable bacteria to pass from the substrate to the ramp.

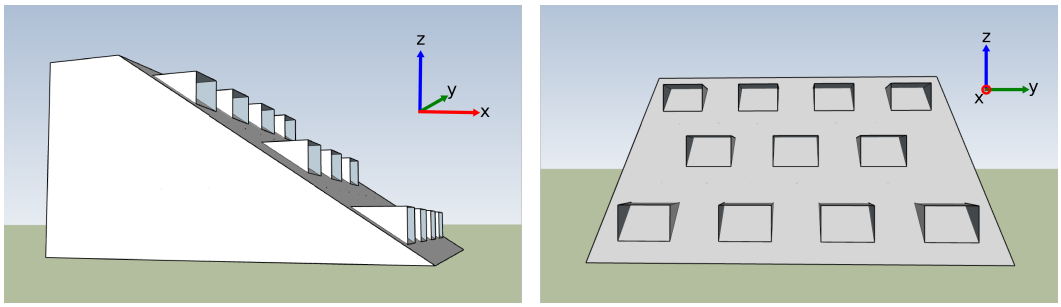

Figure 3.6. 3D scheme of the multilevel microshuttle.In the new model, we implement a ramp for the entrance of bacteria. On the left we show the top view of the microrobot. The side view of the microstructure is shown on the right side.

Considering the last results, we designed another model for the microshuttle. Additionally, in order to integrate more than four bacteria on the microrobot we arranged more microchambers on a multilevel fashion. Each microchamber parameters were the same used for the *coli*-house structure while its lateral sides were modified, because the cell body position must be parallel to the base of microstructure, the microchamber needs to be embedded on the body of the ramp. Thus, the lateral sides were the result of the intersection between the surface of the microchamber and the ramp, whereas the upper microchamber surface protruded from the surface for ensuring holding bacteria on the interior. There were four microchambers on the bottom level of the microshuttle, while in the second level we placed only three, and finally another four microchambers in the upper level. The distance between each microchamber was designed to allow bacteria access to the further-up levels in the microshuttle. The microshuttle was fabricated in the same position as the ramp microstructure, shown in Figure 3.6.

Experiments were performed on an open sample in the same set-up used for the previous measurements, a custom-built inverted optical microscope with bright field illumination. The first step was to detach the microrobots by the use of a mechanical micromanipulator with structures immersed in MB and Tween 20 at a

concentration of 0.2%. After separating several microshuttles from the substrate we added 30 μL of a dense solution of smooth-swimmer bacteria (optical density (OD) not measured). On Figure 3.7 we overlapped the initial and the last frames from a 28 seconds video recorded of two microstructures with a ramp angle of 35°. The upper right object stayed in the same position during the whole video, the bottom left microstructure, in contrast, was free to move based on its lateral side.

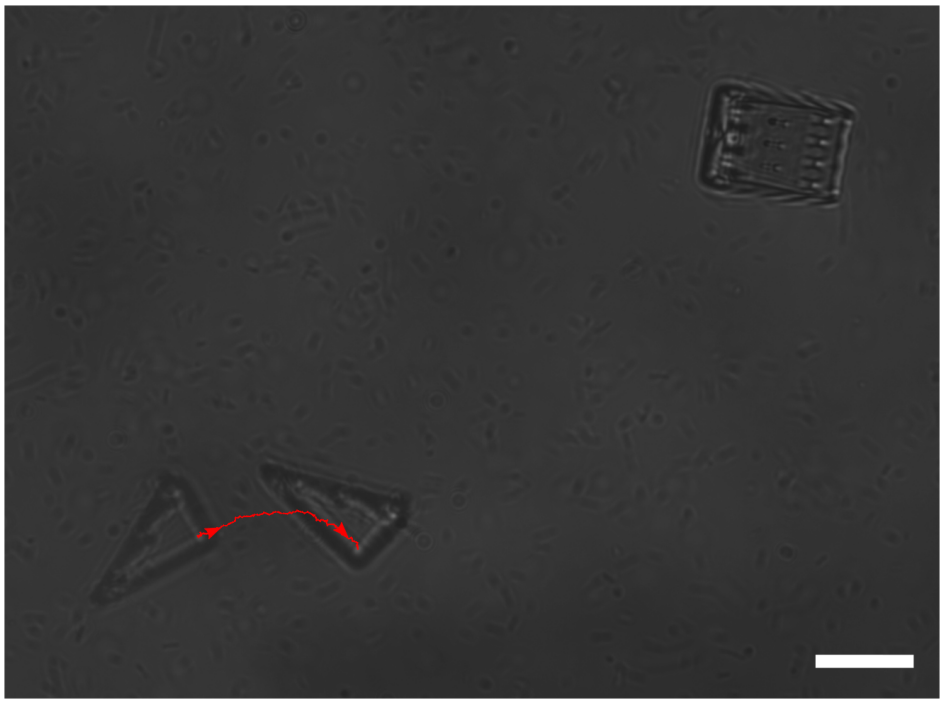

Figure 3.7. Trajectory followed by one of the second model for a microshuttle from a 28 seconds video. Last and final frames were overlapped. The orientation of the microstructure localized at the bottom it is not the optimal, even though the structure is free to move. On the other hand, the microshuttle on the top remained in the same position. The scale bar is 15 μm.

During these experiments several problems arose. Whenever bacteria entered the microchambers, they never reached the upper level of the structure. This issue could derive from the hydrodynamic interactions between bacteria. Consider only a small section of the microshuttle such that three bacteria are inside of it, two placed in the bottom level while the third bacterium is located in the middle level; for a bacterium to reach the upper level in the microstructure, it must pass trough the flow field produced by the other three bacteria. Studies regarding the flow field generated by individual freely swimming bacteria have demonstrated that hydrodynamic effects between two bacteria cannot be negligible when the distance between them is smaller than $\sim 3.3\ \mu m$ [33], which is a fulfilled condition for the relative position of bacteria in our microshuttle.

Additionally, many of the microstructures ended up positioned in several incorrect orientations (as shown in Figure3.7), and, even if most of the fabricated structures detached easily, they reattached to the coverslip after some minutes. A possible

solution to the first problem is to modify the design of the shuttle by fabricating a symmetric structure in such a way that, even if the microrobot is downwards, bacteria move inside the microchambers. Regarding the adhesion problem, we implemented several strategies to overcome it, which are explained in the following section.

3.3 Solving adhesion problem strategies

As an initial strategy to overcome the adhesion problem for the microstructures getting attached to the coverslip, we use Polysorbate 20, better known commercially as Tween 20[5]. The main problem with this trial was the damage caused to the bacteria after some time (results not shown) given the high concentration of surfactant.

The second strategy consisted in employ the polymer Polyvinylpyrrolidone (PVP). We used it in two different modes: as a substrate coating and as another element in the solution. On the first trial we coat overnight a Leja sample[6] with a 1% w/w PVP and methanol solution, then we employed polystyrene (PS) beads of 5 μm diameter. On the top part of Figure 3.8 two frames of different videos are shown, on the left one there was no PVP coating while on the right one we used a coated sample; on the bottom part we show a comparison of the difference between 2 frames separated by a time lapse of 10 seconds with the purpose of observing on which scenario the particles change their position the most, the red spots correspond with the initial particles position, while the yellow areas represent the particles displacement. It is noteworthy that the number of beads that moved in 10 seconds is higher on the PVP coated sample.

In contrast, when PVP was added to a solution composed of MB, and PS beads of 10 μm diameter, depending on the concentration of PVP we obtained different results. For the smaller PVP concentration (0.005%) particles moved for a couple of minutes and then they attached to the surface. While, for a higher PVP concentration of 0.05% the microbeads were on movement for more time $\sim$ 15 minutes, after which particles were deposited on the coverslip.

Finally, the third strategy for overcoming adhesion to the substrate was implementing Van der Waals reversal forces The process for obtaining a low-refractive index layer is explained in subsection 1.2.3, and based on the experiments showed in that subsection, we chose to employ this technique for future experiments involving free-floating microstructures.

[5]The MB already contains Tween 20 in a small concentration of 0.002%, but used as a surfactant for the microshuttles we added it at a concentration of 0.2%

[6]`https://leja.nl/`

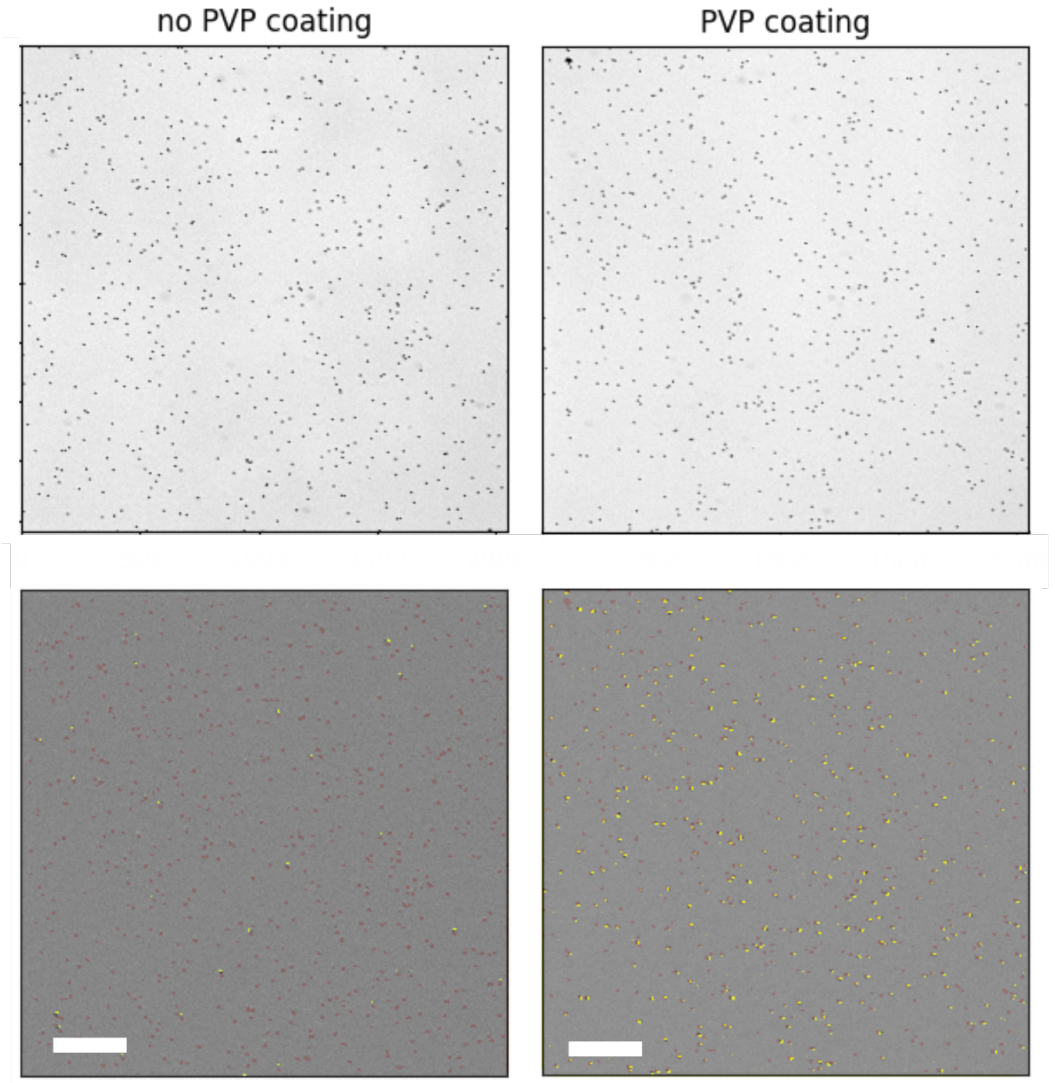

Figure 3.8. Testing PVP coating effectiveness. Two different samples using polystyrene (PS) beads with 5 μm diameter. The left column corresponds to non PVP coating on the substrate, while on the right column we applied a PVP coating. On the bottom we show the initial and final frames comparison for the particles displacement after 10 seconds. The red spots correspond to initial particles position, while the yellow areas represent the particles that moved apart from their original position. The scale bar is 200 μm.

3.4 Symmetric microshuttle and influence of the ramp extension

Once the low-refractive index layer protocol was generated and its effectiveness was tested, we proceeded with experiments using a new design for the microshuttle. Derived from the previous section results, we discarded a multilevel style structure for incorporating bacteria. Instead, we reconsider the basic model and we included ramps with 10° inclination in both bottom and top surfaces for a reflection symmetric

structure[7]; besides the microchambers were elevated at 1 μm above the base of the ramp. Due to weak adhesion of structures we used a sample with SU-8 3025 which was preliminary coated with a water solvent layer (section 1.2.2). The fabrication parameters were a laser power of 10 mW and scanning speed for the spacers between each michochamber and the body of 60 and 160 $^{\mu m}/_{s}$, respectively. The microchamber size of the square cross section was 2.6 μm, thus the total height was 3.7 μm.

Moving towards the development of control and steering of the microshuttle by light-driven bacteria, the set-up used for experiments involving strains expressing PR is a custom-built inverted optical microscope wit a 60x (NA 1.27) water immersion objective. Green light is reflected on the chip of a Digital Light Processor (DLP-Texas Instruments DLP Lightcrafter 6500) to then focus it on the same focal plane of the camera to stimulate photoreceptors on bacteria. The DLP nucleus is a digital micromirror device (DMD), which contains over 2 million micromirrors with a high resolution 1080p (1920x1080). The microscopic mirrors correspond to pixels in the displayed image and they can modulate the amplitude, direction, and/or phase of incoming light. We control the DLP through a Python shell, which allows to shift in time and space between light patterns with arbitrary shape. The sample is mounted on a motorized 3-axis translation stage from Zaber, while the motion control is made by a programmable 3-axis joystick from Zaber. For guaranteeing that green illumination is exclusively coming from the DLP, we filtered the source of bright field illumination.

We used a genetically modified strain of *E. coli* AB1157[32] with ATP and CheY deleted genes and proteorhodopsin expression through plasmid insertion [106] which can be indicated by AB1157 ΔATP ΔCheY + PR plasmid. The ATP and CheY deletion were done on our laboratory by red recombination [28]. The speed of this mutated strain is modulated as a function of green light intensity. For the experiments, we needed a sealed sample which was obtained by attaching two coverslips on top of each other: the top one with microstructures in a downwards position, and the bottom one consisted of a gene frame as spacer with a low-refractive index layer. We used UV glue to sealed two sides of the sample, then 200 μL of bacteria in MB were introduced to the sample. Then, the sample was completely sealed using vacuum grease on the open sides. A sample in this configuration allowed obtaining free-floating microshuttles without using a mechanical micromanipulator. In this sample oxygen was depleted by bacteria in one hour at cell concentration of 10% of bacteria with 0.47 OD. After this time, cells were non motile and only swam in the presence of green light illumination. In Figure 3.9 a shuttle is shown in a frame extracted from a video registered at 100 fps, after the tracking we obtained the coordinates of the center of mass which is presented in the same figure.

[7]The microstructures had reflection symmetry with respect to the plane parallel to the ramp base which contains the point at half the shuttle height.

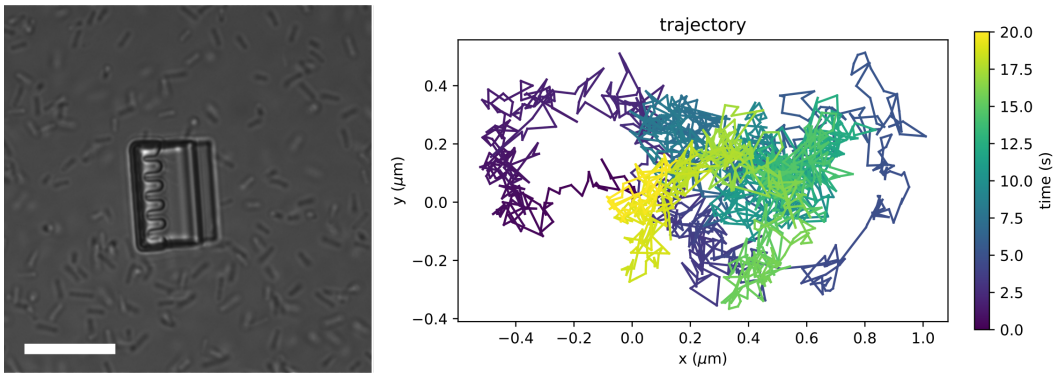

Figure 3.9. On the left we show the first frame from a microshuttle video recorded at 100 fps for 20 seconds unde bright field illumination. The microrobot trajectory is shown on the right. The scale bar is 15 μm.

From the trajectory in Figure 3.9 we observed two important features: there is no circular path in the microshuttle movement, and the total displacement of the object is significantly smaller than the distance obtained in the basic model *coli*-house (section 3.1 Figure 3.4), even though both results were obtained from similar time-length videos and similar number of bacteria on-board. We concluded that the source of this issue is the ramp extension. Given the small inclination angle of the ramp its length is $\sim 7\ \mu m$, while, as mentioned in the previous chapter, the flagellar filaments length is variable from 5 up to 10 μm, this implies that only a short portion of the flagellar bundle is outside the microstructure, generating a critical reduction in the propulsion. As a verification of this deduction, we fabricated a modified shuttle with a shortened ramp (ramp angle of 30°) and repeated the last experiment (data not shown). We measured a major increment in the microrobot propulsion, nevertheless its movement continued following a circular trajectory.

Until this point we had managed to solve most of the problems that arose throughout the development of this part of the thesis. The implementation of a low-refractive index layer on the substrate allowed free movement of the structures during several hours. A water-soluble sacrificial layer facilitated the microrobots detachment without recurring to a mechanical micromanipulator. On the other hand, the circular path in the trajectory of each shuttle model represents a big challenge for achieving the optimal control of the self-powered microrobot. In the next section we approach to this situation by changing the location of bacteria on structure.

3.5 Steering of the final microstructure: micro-catamaran

Among the different models of microshuttle used in the previous experiments, there is a common feature: the orientation of bacteria in the structure. In the idealization of a self-powered microrobot using as energy source the maximal propulsion of the flagellar bundle, we chose to place bacteria in a perpendicular position with respect to the largest axis of the shuttle. However, after several trials it appears as this strategy generates the circular path trajectory of each microstructure as an intrinsic consequence. What should be the proper orientation of bacteria to enable an optimal control and steering of the shuttle? On which way and magnitude is it possible to

reduce the influence of a near rigid surface on swimming bacteria by changing their orientation?

Consider a microshuttle with only two chambers and imagine a plane of symmetry containing the wall shared by the chambers, represented by the red line in Figure 3.10. Then, picture changing the orientation of bacteria by increasing the angle between the axis of the microchambers (yellow dashed line in Figure 3.10) and the middle plane until reaching an antiparallel position as shown on the right in Figure 3.10, i.e., rising the angle from $\theta_i = 0°$ up to $\theta_f = 90°$. For θ_i the component of bacterial flagellar propulsion parallel to the red plane is maximal but the shuttle moves following a circular trajectory, in contrast for θ_f the circular path would reach a limit radius of zero (this means that the microstructure would only have a rotational motion, while the translational motion would disappear) and the propulsion generated by one bacterium is countered by the bacterium at the opposite position generating no movement. Thus, there must be an angle θ such that $\theta_i < \theta < \theta_f$ which maximizes the translational velocity and maximizes the number of bacteria to be assembled in the microshuttle.

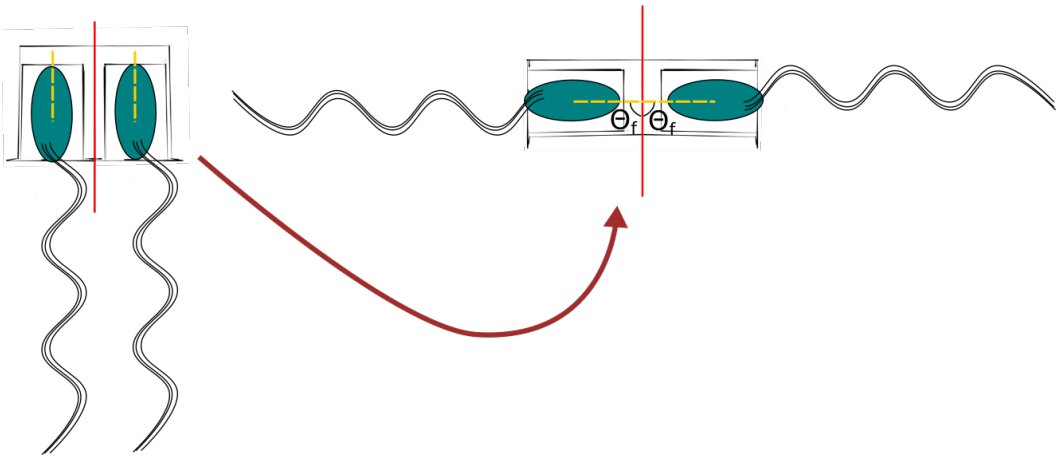

Figure 3.10. Top-down perspective of an hypothetical two microchambers shuttle. We show on the left side the initial position of two bacteria in an hypothetical basic microshuttle. The red line represents a symmetry plane while the yellow dashed line corresponds to the axis of the chamber. After increasing the angle between this two coloured lines to the maximum value of 90°, bacteria are placed in an antiparallel orientation, right side.

Based on this conjecture, we developed a completely different shuttle design. The microchambers were arranged as shown in Figure 3.11a tilted at $\theta = 45°$. Because each bacteria has a self-propulsion given by a constant force, if we only analyse a pair of them symmetrically located and represented by blue vectors on Figure 3.11a, then the total propulsion will be pointing in the positive y direction (the addition of this forces are presented in Figure 3.11).

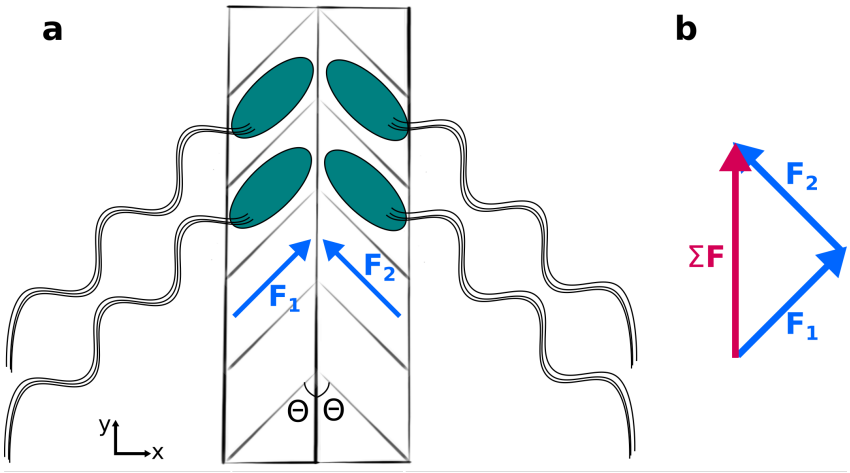

Figure 3.11. Ultimate microshuttle approach for integrating bacteria(a) Scheme of microchambers arrangement in a single arm. **(b)** Addition of the vectors representing the propulsion of a couple of symmetric bacteria.

Before starting with the new microshuttle fabrication, in order to ensure the entrance of single bacteria, we characterized the internal walls separating each microchamber on the structure by changing the scanning speed under a fixed laser power. We used two different SU-8 photoresist for a comparison between the energy dose for each case, and, because microstructures must be attached to the surface, we used samples coated with three layers Omnicoat. We fabricated the shape shown in Figure 3.11a which consists of the body (bottom and upper plane surface, and center wall), and the internal walls generating seven pairs of microchambers. The body scanning speed was 30 $\mu m/s$ fixed for the range of laser power (1.9, 2.5, 3, 4, 5 mW), on the other hand, depending on the value obtained from $\mathbf{P}^2/\sigma v$ (which is the argument in equations (1.17) and (1.18)) we chose several values for the internal walls scanning speed. The most interesting cases corresponded to laser powers of 1.9 and 2.5 mW, which are shown in Figure 3.12, for the other values the energy dose was high enough that there was no microchambers formed correctly.

Each image consist of two parts: the upper section was acquired under bright field illumination showing microstructures immersed in double distilled water, red line enclosure corresponds to internal walls generated trough a single scanning line, while the yellow line represents fabrication by a double scanning line; the bottom section is a fluorescence image where cells bodies are clearly visible, we used the strain HCB437 RFP+, these cells express the red fluorescent protein mRFP1 [113]. Based on this observations we chose a laser power of 1.9 mW and a scanning speed of internal walls of 4 $\mu m/s$ as fabrication parameters for the new microshuttle.

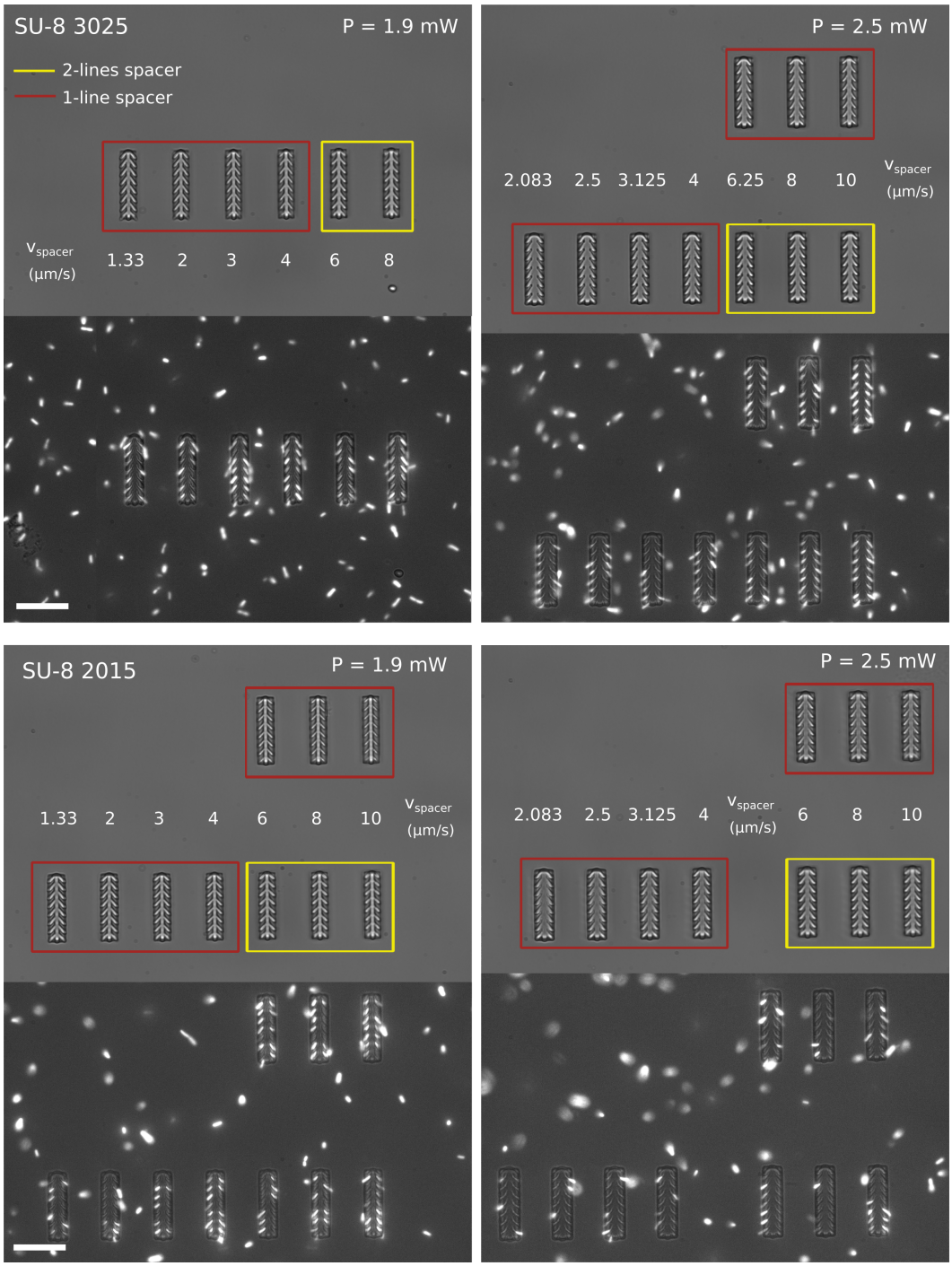

Figure 3.12. Internal walls calibration. Microstructures fabricated using two different series of SU-8. Upper row of images correspond to SU-8 3025, and bottom row to SU-8 2015. A single figure is formed by two pictures: bright field microscopy image is located at the top while cell bodies are shown below in a fluorescence microscopy photograph. The internal walls were generated by a single scanning line (groups inside a red stroke) or a double scanning line (yellow enclosure). Laser power and scanning speeds are indicated on each image. The scale bar is 15 μm.

Aiming for an easy method to control steering of the microrobot without requiring a feedback algorithm technique, the shuttle will consist of four main parts: two arms with same number of microchambers, and two long connectors joining both arms. In this arrangement the shuttle can be remotely controlled by modulating green light intensity on each arm. Considering the flagellar length and bacteria orientation determined by the michochambers, the separation distance between the arms must allow a free movement of all the flagellar bundles. A bright field image of this new microshuttle design is shown on Figure 3.13, which was named catamaran due to its geometry and shape. The length and width of each arm is 20 μm and 5 μm respectively, the distance between microchambers is 2.6 μm, and the connector length is 15 μm.

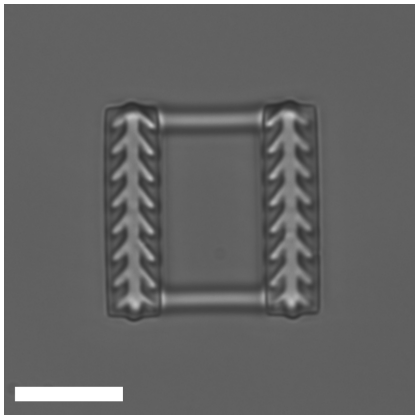

Figure 3.13. Catamaran model Bright field image of a microshuttle. The scale bar is 10 μm.

After achieving a catamaran shuttle with suitable features for bacteria[8], we proceeded with experiments for testing the microstructure guiding through light patterns. We used a sealed sample made by following same procedure described in the last section, bottom substrate coated with a low-refractive index layer while the coverslip where microrobots were fabricated was used as top surface. As a consequence of issues related with bacterial growth, it was not possible the use the appropriate bacteria strain. Ideally these experiments should be performed employing light-driven smooth-swimmers AB1157 ΔATP ΔCheY PR+, instead we used a light-driven tumbling strain (AB1157 ΔATP[9] + PR plasmid). We projected onto the sample two different green light patterns: first one composed of three vertical stripes, and the second one formed by three horizontal rectangles, in both cases the central rectangle had a green light intensity equal to zero, while for the rest of the surface we projected the maximum light intensity.

We expect to steer the microshuttle movement by placing a single catamaran arm under green light while the rest of the structure is under a dark region, there will be a non-uniform propulsion on the microrobot caused by green light illuminated bacteria. On Figure 3.14 we show the trajectory followed by the same microshuttle when illuminated by two different green patterns. Left side of each figure shows first and last frame of a video recorded at 50 fps, microshuttle final position is red highlighted and the illuminated region is shown in green shade. On the right side, we show the trajectory followed by the catamaran during the time-lapse indicated in the color bar.

Comparing the trajectories shown in Figure 3.14 with the results of section 3.1 there are several improvements to achieve. For example, the trajectory for *coli*-house in Figure 3.4 shows a larger displacement in comparison with the last experiment.

[8]Due to details related with the optical alignment of two-photon polymerization set-up, appearance of the microstructure showed in Figure 3.14 is quite different to the picture showed in Figure 3.13.

[9]Gene deletion by lambda red recombination method [28]

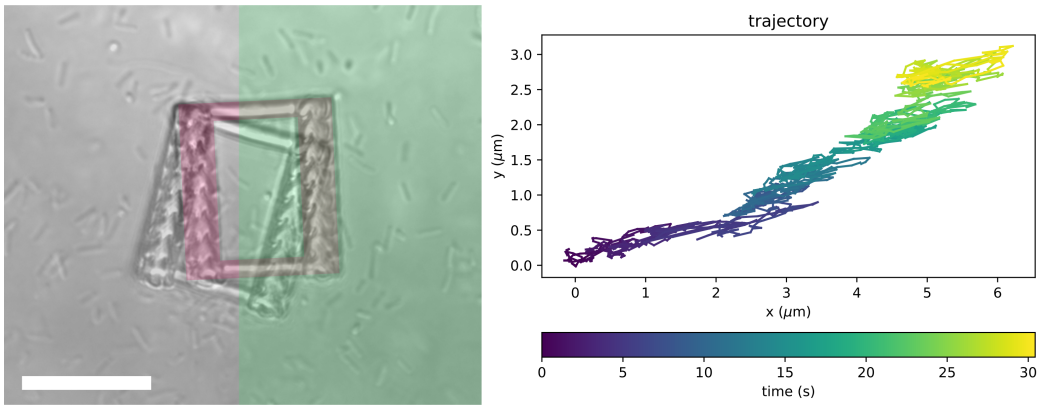

(a) Vertical stripes illumination. Counterclockwise rotation

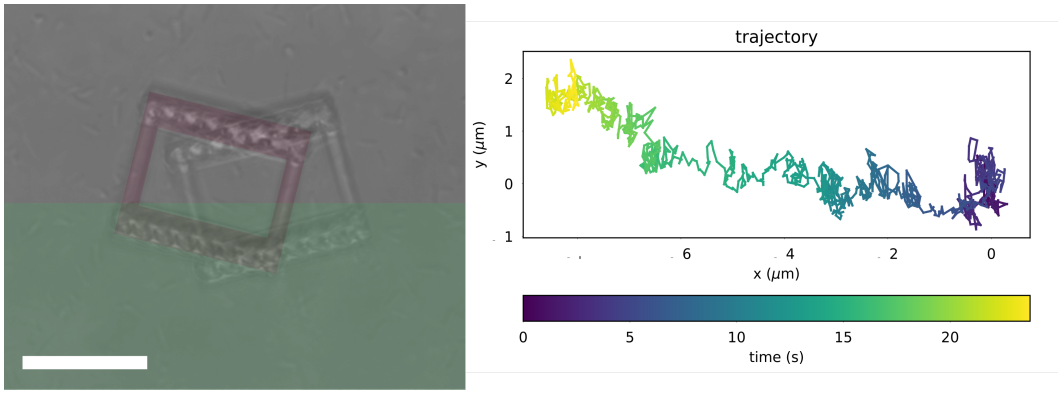

(b) Horizontal bands illumination. Clockwise rotation

Figure 3.14. Microshuttle trajectory under non-uniform green light patterns. Left side: bright field images extracted from videos recorded at 50 fps. Final video frame is red shaded, while the green light illuminated region is represented as a green rectangle. Right side: trajectory followed by the microbot. The time-lapse is indicated on the color bar. Both scale bars correspond to 20 μm.

This result could be caused by two main factors: (i) the use of light-driven tumbling bacteria, and (ii) the features of the microstructure. Light-driven smooth-swimmers are the perfect bacteria type for these experiments because they remain inside of microchambers as well as the total number of bacteria on-board, instead tumbling bacteria change swimming direction each second which implies a time variable number of bacteria propelling the microstructure which produces a low displacement efficiency. The microfabrication correspondence between the structure and the design is also very important. Unfortunately, the microrobot used in the last experiments had several imperfections: the internal walls on the arms were deformed generating microchambers not built properly, each arm appears to be tilted positioning bacteria at a variable height from the substrate.

The results shown in Figure 3.14 uncover a very mesmerizing outcome: for the first time in the brief history of this project the microshuttle was controlled to rotate following a counterclockwise path. This fact will have major implications for future experiments. After testing these simple green light patterns, the next step is project

on the sample a light trial composed by two parallel stripes. The width of these light stripes must be slightly larger than the width of a single arm catamaran, thus by modulating light intensity the microrobot will move on the trajectory defined by the light trial. Once the features of this light path be define then transportation of a cargo by a microshuttle will be feasible.

3.6 Conclusions

We demonstrate that control and steering of biohybrid microrobots can be obtained by combining the self-assemble of a defined number of propelling units onto precisely defined location of genetically engineered swimming bacteria. Using two-photon lithography we fabricated four different designs for the microrobot: basic microshuttle, microshuttle with ramps, symmetric microshuttle, and finally catamaran design. Propelling bacteria expressing the light-driven proton pump proteorhodopsin can be confined in sealed samples and obtain energy from harvesting light from the environment. Light patterns are easily shaped in space and time, by the use of a DLP we were able to control the trajectory of a single microshuttle by addressing it with a delimited light path. One of the main issues in developing the experiments was microstructures adhesion to the substrate, this was overcome by the implementation of a novel low refractive index layer producing Van der Waals forces reversal sign. The characteristic clockwise circular motion of bacteria near a solid boundary contribute to a deficient control of the microshuttle, by modifying bacteria distribution on the catamaran microstructures it was possible to maximize the number of propeller units along with the velocity of the microrobot. Besides we show that catamaran microshuttle is capable of rotate in both clockwise and counterclockwise directions by illuminating only one part of the structure. This could lead to control and steering without a feedback control loop for the movement of the microrobot. Future studies may try to explore the use our microshuttles for transporting cargo objects, such as bigger cells or colloidal particles.

Part III

3D microstructures for soft matter studies

Chapter 4

Dynamics of microhelices

The work in this chapter was first presented in [20] and was done in collaboration with Silvio Bianchi, Gaszton Vizsnyiczai, and Roberto Di Leonardo.

In this chapter of the thesis we combined two-photon lithography and optical tweezers to investigate the Brownian fluctuations, propeller characteristics and relaxation dynamics of microfabricated rigid and deformable helices.

4.1 Introduction

We find that Brownian motion displays correlations between angular and translational fluctuations from which we can directly measure the hydrodynamic coupling coefficient that is responsible for thrust generation. By varying the distance of the microhelices from a no-slip boundary we can systematically measure the effects of a nearby wall on the resistance matrix. Our results indicate that a rotated helix moves faster when a nearby no-slip boundary is present, providing a quantitative insight on thrust enhancement in confined geometries for both synthetic and biological microswimmers. Moving to deformable helices we studied the dynamics following elongation and found an exponential relaxation to equilibrium resulting from a translational mobility that only weakly depends on elongation.

Helical structures are widely used in the macroscopic world as rigid rotating propellers or as elastically highly deformable elements. The same functions can be performed by micro-helices although the dynamics is dominated by factors like a strong viscous damping and Brownian motion. Micro-helices are often used as propellers in both biological[13, 66] and synthetic[46, 83, 121, 91] micro-swimmers. The characterization of the thrust force of a rotating helix has been the subject of numerous studies in the field of low Reynolds number hydrodynamics [67, 82, 26, 88, 21]. The absence of inertial effects is an important element in the description of dynamical phenomena at the micron scale, but the truly distinctive feature of microscopic dynamics is Brownian motion. In this respect very little has been done for chiral objects. Although roto-translational couplings may be present in non-chiral objects, they disappear when we place the object's origin on the center of hydrodynamic resistance[49]. On the contrary, helices are chiral objects with an intrinsic roto-traslational coupling that is responsible for the appearance of correlations in the Brownian fluctuations of rotational and translational degrees of

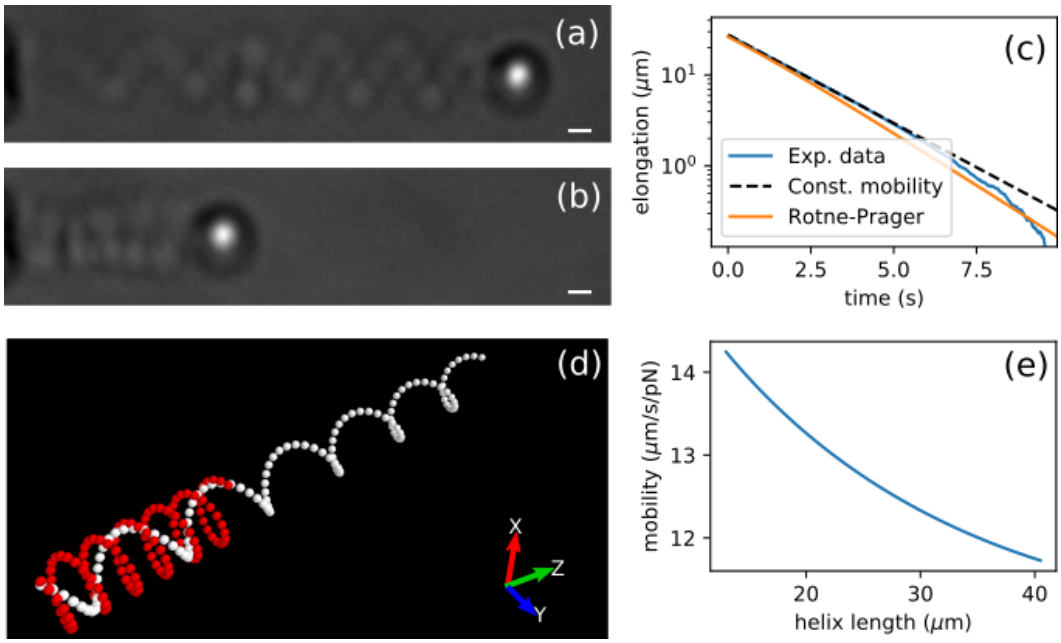

Figure 4.1. Elastic micro-helix.(a) Bright-field image of a soft BSA micro-helix elongated using an optical trap. (b) After the optical trap is turned off the micro-helix relaxes to its equilibrium position. Note that the left extremity of the helix is connected to a support anchored to the coverglass. (c) Average trajectory the micro-spring shown in (a) relaxing to its equilibrium position. Blue line plots the experimental data, dashed line is a fit to an exponential decay and orange line plots the result obtained by computing the drag with the Rotne-Prager method. (d) Discretization of the helix into many spherical elements. The two clusters show the helix in its rest position and in an elongated state. (e) Simulated mobility coefficient respect to an elongation of the helix-handle structure. All scale bars are 2 μm.

freedom. These intrinsic correlations in chiral colloids have never been observed in experiments.

It is important to mention the criterion for denominating rigid or elastic micro-helix. Considering the applied forces by optical tweezers (on the order of pN), and taking into account the values for the elastic modulus for each material (according to reference [30], SU-8[1] Young modulus is E_{SU-8}=(4.95 $\pm$ 0.42) GPa, while, for the case of bovine serum albumin (BSA) elastic modulus are of the order of 1 MPa [58]), the micro-helix fabricated using the BSA protein it is called "elastic micro-helix", while, "rigid micro-helix" is assigned to the material with the highest Young's modulus, i.e., SU-8.

4.2 Materials and methods

4.2.1 Elastic micro-helix fabrication

We fabricated an elastic micro-helix using protein photocrosslinking. By the combination of proteins with photoinitiators it has been demonstrated the creation of 3D

[1]in tension, post-exposure baking at 95°C, screw tensile testing machine

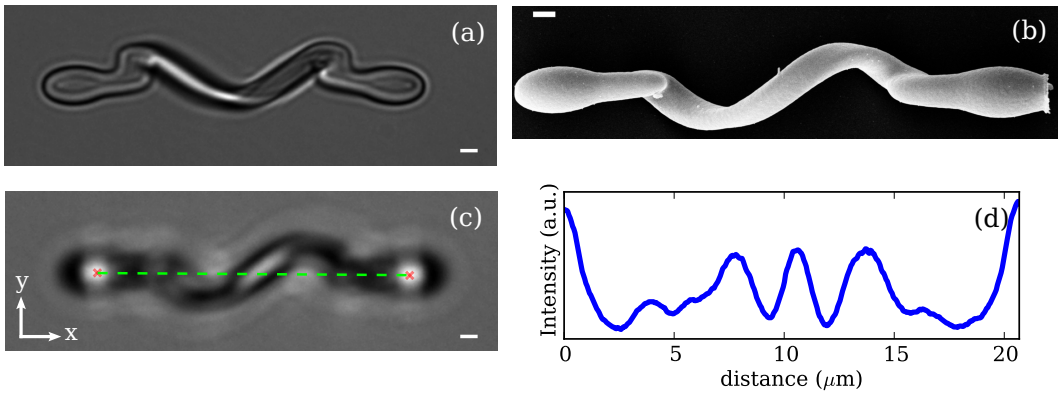

Figure 4.2. *Rigid micro-helix.*(a) Bright-field microscopy image of a micro-fabricated helix. At each extremity, the helix is connected to an ellipsoid with an L-shaped joint. The two ellipsoids serve as handles for two optical traps. (b) Scanning electron microscopy image of a micro-helix. (c) During the measurements optical traps are shifted 1 μm above the focal plane to facilitate tracking. (d) A slice of the intensity of the frame shown (b) interpolated along the green dashed line connecting the two intensity peaks produced by the handles. The central peak, which is due to the helix, shifts as the helix rotates. All scale bars are 1 μm. Reproduced from Ref. [20].

microstructures [79]. For the generation of this flexible micro-helix we implemented a custom built two-photon polymerization setup [114, 22] and BSA [80, 96] on an open sample. The corresponding laser power and scanning speed were 16 mW and 20 μm/s, respectively. After fabrication, the non crosslinked BSA was gently extracted with a pipette and substituted with deionized water, we repeated this step until the liquid is completely replaced with water. In its rest position the fabricated micro-helix has a length of 13 μm and a radius of 4 μm (see Figure 4.1(a,b)). We estimate the thickness of the helix filament to be about the point spread function of our NIR laser that is 0.7 μm. Based on a previous microstructure design [104], one extremity of the spring is connected to a cubic support, which is anchored to the coverglass, while the other extremity is connected to a 4 μm sphere that serves as a handle that facilitates trapping by providing a strong axial gradient force that balances the scattering force on the helix filament and allows stable 3D trapping for tracking easily the structure elongation.

4.2.2 Rigid micro-helix generation

On the other hand, the rigid micro-helices were created from SU-8 2015 photoresist (MicroChem Corp) on the same two-photon polymerization set-up mentioned before using a 60x 1.4NA objective. Laser power and scanning speed were 3 mW and 8 μm/s, respectively. After exposure, the photoresist sample was baked at 100 °C for 7 min, then developed by its standard developer solvent, followed by rinsing in a 1:1 mixture of water and ethanol, and finally dried with a gentle blow of nitrogen. Strong adhesion of the structures to the carrier cover glass was ensured by a layer of OmniCoat adhesion promoter (MicroChem Corp). To minimize deformations of the micro-helices due to the fluid flows and surface tension forces present during development, a protective structure composed of three walls is fabricated for each

micro-helix. After development, the micro-helices are first immersed in deionized water and then detached from the glass substrate using a pulled glass pipette controlled by a micromanipulator. Free-floating helices could then be trapped by optical traps.

A bright-field image and a scanning electron microscopy image of a micro-helix are shown respectively in Figure 4.2(a) and Figure 4.2(b). The micro-structure is designed as an helix with pitch angle ψ=42°, radius 2 μm and length $L = 2\pi r \tan(\psi) = 11.5$ μm. At each of the two extremes, a joint connects the helix to a prolate ellipsoid with major an minor diameters of 4 and 2 microns respectively. The complete length of the structure including the helix, the L-shaped joints, and the ellipsoidal handles is approximately 24 μm. The micro-helices are fabricated vertically (i.e. standing up on the photoresist coated coverglass) with one of the two ellipsoid adhering on the glass. The point spread function of the writing laser is elongated along the vertical axis resulting in a helical ribbon shape (see Figure 4.2(b)). A section of the helix filament can be thought as an ellipse with minor and major axis measuring 0.6 μm and 1.1 μm respectively.

A standard optical microscope coupled with an IR holographic optical tweezers setup is used to observe the Brownian fluctuations. The two ellipsoids at the extremities of the micro-helix that, similarly to the handle of the elastic structure shown in Figure 4.1, serve both as handles for optical trapping and for tracking. To facilitate tracking the helices are arranged horizontally at about 1 μm above the focal plane as shown in Figure 4.2(c). In this configuration, the two ellipsoids produce bright blobs which can be easily tracked using a center of mass algorithm. Calling (x_1, y_1) and (x_2, y_2) the in-plane coordinates of the two handles, with x and y directions defined in Figure 4.2(c), we define the helix position (x, y) as the middle point of the segment joining the two handles (dashed line in Figure 4.2(c)). The in-plane orientation of the helix is computed as the angle between the line connecting the two handles and the x axis: $\theta = \arctan\left[(y_2 - y_1)/(x_2 - x_1)\right]$. The helix appears as a dark stripe with a sinusoidal shape and has a bright elongated blob given by the part of the helix that is closer to the focal plane. The rotations of the helix around its axis are measured by tracking the position of the blob respect to the handles. For each frame we interpolate the image along a line connecting the center of the two ellipsoids. Figure 4.2(d) shows the image interpolated intensity along the green dashed line shown in Figure 4.2(c), the peak corresponding due to the helix filament shifts upon helix rotation but is not affected by translations of the entire structure. After tracking the peak position (again using a center of mass algorithm) we convert its linear displacement Δl to an angle shift $\Delta\phi = 2\pi\Delta l/L$. The mean vertical distance of the helix from the coverglass can be indirectly derived as the sum of the holographic displacement of the trapping spots (1 μm) and the vertical displacement of the focal plane from the coverglass (7 μm). This last value can be measured by focusing on small scatterers attached to the coverslip surface and then applying a controlled z translation using a piezoelectric stage.

4.3 Results and discussion

4.3.1 Dynamics of an elastic micro-helix

In this section we analyse the relaxation dynamics of an elastic micro-helix. Using optical tweezers, the spring is stretched up to a length of approximately 40 μm (its equilibrium length is 13 μm) and is then released by blocking the trapping laser. We iterated 60 times the procedure to average out Brownian fluctuations and extracted the mean trajectory shown in Figure 4.1(c).

We can assume that the restoring force exerted by our micro-helix is linear with its elongation ΔL. Therefore, since the relaxation trajectory is well described by an exponential, we can conclude that the drag coefficient γ_L of the helix remains constant as the elongation ΔL changes. To check the validity of this statement, using the Rotne-Prager method, we computed the drag of an helix that is extending/contracting while is fixed in one point (see Figure 4.1(d)). A rigorous simulation would require the computation of the elastic stress acting on each element composing the extended helix that consequently can be used to compute the velocities. Here, to simplify our procedure, we will simply assume that the spring maintains its helical shape while keeping constant its contour length. This last assumption is supported by the following argument: a BSA straight filament with same section of our micro-helix (BSA elastic modulus are of the order of 1 MPa [58]) stretched by a the typical force produced by an optical trap (approximately 1 pN) would change its length by less than 0.01%. Calling c the contour length of the helix, N the number of turns and L the length, we have that the coordinates of the elements composing the spring are:

$$x = \sqrt{c^2 - L^2}/(2\pi N)\cos(2\pi N s) \tag{4.1}$$

$$y = \sqrt{c^2 - L^2}/(2\pi N)\sin(2\pi N s) \tag{4.2}$$

$$z = sL \tag{4.3}$$

where s is real valued parameter, bounded in the interval $(0, 1)$, whose value for the n-th particle is $s = n/N_{\text{tot}}$ (N_{tot} is the total number of elements composing the helix). Given the velocity of contraction/extension of the helix $\dot{L}$ the translational velocity v_n of each element is computed as $\mathbf{v}_n = \dot{r} = (\partial_L \mathbf{r})\dot{L}$ where ∂_L indicates the partial derivative respect to L. To compute the rotational velocity $\boldsymbol{\omega}_n$ of each element we first write the tangent versor $\hat{\mathbf{p}} = \partial_s \mathbf{r}/\left|\partial_s \mathbf{r}\right|$ along the helix. The rate at which the versor changes is related to $\boldsymbol{\omega}_n$ as $\partial_L \hat{\mathbf{p}} \dot{L} = \boldsymbol{\omega}_n \times \hat{\mathbf{p}}$. Taking the cross product of $\hat{\mathbf{p}}$ with both sides of this last expression and assuming that the helix experiences no torsion (i.e. $\boldsymbol{\omega}_n \cdot \hat{\mathbf{p}} = 0$), after a few manipulations we get to the result $\boldsymbol{\omega}_n = \hat{\mathbf{p}} \times \partial_L \hat{\mathbf{p}} \dot{L}$. Once we have the translational and rotational velocities of the helix elements, respectively $\mathbf{v}_n$ and $\boldsymbol{\omega}_n$, we can use the Rotne-Prager method to compute the viscous forces acting on them. We can finally compute the force acting on the helix as the sum of the forces acting on each element and divide it by $\dot{L}$ to obtain the drag. In the range of elongation explored the helix drag goes from 0.032 pNs/μm to 0.047 pNs/μm corresponding to a 50% variation. The helix drag must be summed to the drag of the spherical handle $6\pi\eta r_{\text{handle}} = 0.037$ pNs/μm to obtain the total drag γ_L which is related with the total mobility by $M_L = \gamma_L^{-1}$

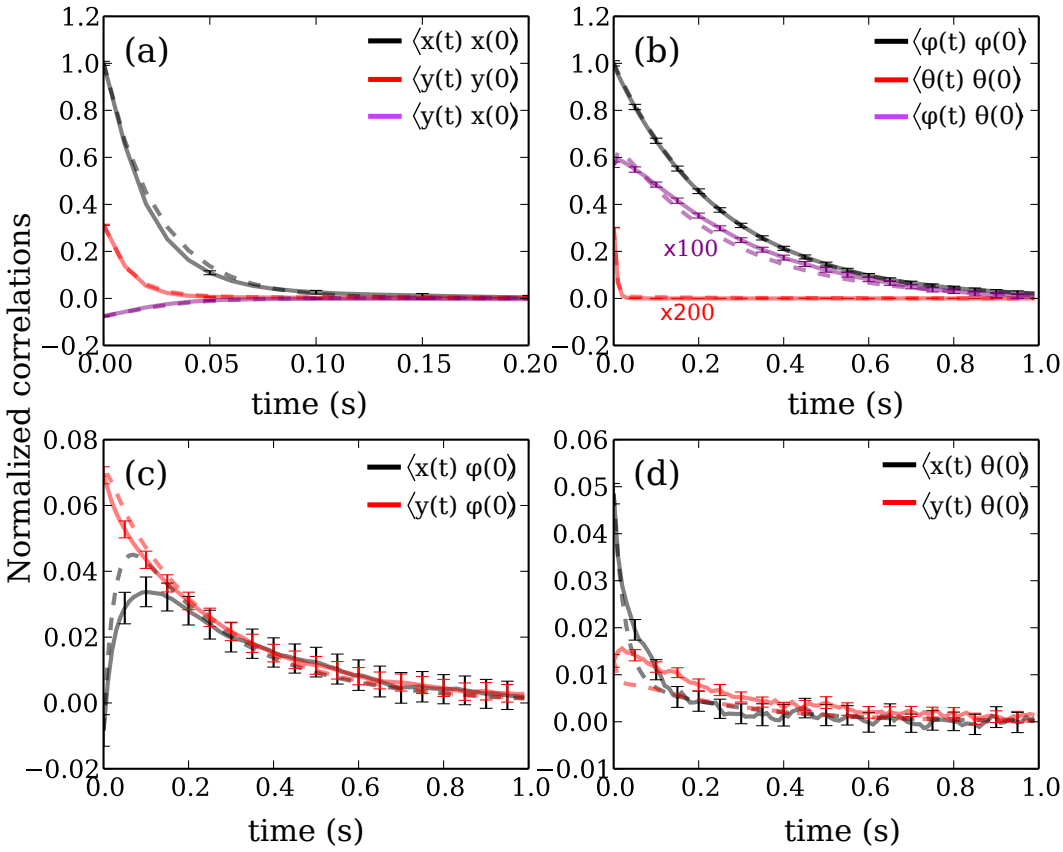

Figure 4.3. Brownian fluctuations of an optically trapped microhelix. The correlation functions have been normalized to $\langle x^2 \rangle$ in (a), $\langle \phi^2 \rangle$ in (b), $(\langle \phi^2 \rangle \langle x^2 \rangle)^{1/2}$ in (c), $(\langle \theta^2 \rangle \langle x^2 \rangle)^{1/2}$ in (d). Purple and red curves in (b) have been further multiplied by factors of 100 and 200 respectively to make them visible on the same scale. Experimental data are plotted as solid lines while the dashed lines represent the best fitting curves obtained using Eq. (4.8). Reproduced from Ref. [20].

plotted in Figure 4.1(e). To compare this last result with our experimental data we numerically integrate the equation $\gamma_L \dot{L} = -kL$ where k is the constant value adjusted to best match the fitted exponential exponential decay constant with the average value of k/γ_L. The result, plotted in Figure 4.1(c), display a fair but not perfect agreement with experimental data. The reason for such a discrepancy is probably due to the presence of the nearby glass wall that increases the drag of the handle and reduces the importance of the 50% drag variation of the helix.

4.3.2 Study of a rigid micro-helix

In Figure 4.2(c) it is shown the configuration of a trapped rigid micro-helix i.e. with the L-shaped in the upwards direction. This appears to be the most favorable position in terms of tracking and stability. The trapped helix is imaged at 100 fps for almost 5 hours. We track the position and orientation of the helix through the four

coordinates x, y, θ, ϕ defined above. For small fluctuations around the equilibrium configuration the force field produced by the optical traps can be derived from a quadratic potential:

$$U = \boldsymbol{\xi}^T \mathbf{K} \boldsymbol{\xi} \tag{4.4}$$

where $\boldsymbol{\xi}$ represents the column vector $(x, y, \phi, \theta)^T$. This last assumption is confirmed by the fact the probability distribution of all coordinates is Gaussian as expected using Boltzmann statistics. The elastic constants K_{ij} of the potential can be characterized using the well known properties of multivariate Gaussian distribution:

$$\langle \boldsymbol{\xi} \boldsymbol{\xi}^T \rangle = k_B T \mathbf{K}^{-1} \tag{4.5}$$

where k_B is the Boltzmann constant, T is absolute temperature. Replacing the average operator $\langle \cdot \rangle$ with a time average we compute $\langle \boldsymbol{\xi} \boldsymbol{\xi}^T \rangle$ from our tracks and thus obtain $\mathbf{K}$. Indicating with $\mathbf{M}$ the mobility matrix and with $\boldsymbol{\eta}(t)$ the zero average white noise term we can write a Langevin equation for the helix:

$$\dot{\boldsymbol{\xi}} = -\mathbf{M}\mathbf{K}\boldsymbol{\xi}(t) + \mathbf{M}\boldsymbol{\eta}(t) \tag{4.6}$$

whose formal solution can be written as [86]:

$$\boldsymbol{\xi}(t) = \mathbf{G}(t)\boldsymbol{\xi}(0) + \int_0^t \mathbf{G}(t - t')\mathbf{M}\boldsymbol{\eta}(t')dt' \tag{4.7}$$

where $\mathbf{G}(t) = \exp(-\mathbf{M}\mathbf{K}t)$. The time correlation function can be obtained by multiplying equation (4.7) by $\boldsymbol{\xi}^T(0)$ and by taking the ensemble average. Noting that the noise term has no correlation with the initial condition (i.e. $\langle \boldsymbol{\eta}(t)\boldsymbol{\xi}^T(0) \rangle = 0$) and using Eq. (4.5) to replace the term $\langle \boldsymbol{\xi}(0)\boldsymbol{\xi}^T(0) \rangle$ we have that:

$$\langle \boldsymbol{\xi}(t)\boldsymbol{\xi}^T(0) \rangle = \mathbf{G}(t)\mathbf{K}^{-1}k_B T \tag{4.8}$$

An explicit expression of the matrix exponential $\mathbf{G}$ is complicated but its numerical computation is straightforward. Calling $\boldsymbol{\Lambda}$ the diagonal matrix storing the eigenvalues of $\mathbf{MK}$ and indicating with $\mathbf{C}$ the coordinates transform that diagonalize $\mathbf{MK}$ we have:

$$\mathbf{G}(t) = \mathbf{C} \exp(-\boldsymbol{\Lambda} t)\mathbf{C}^{-1} \tag{4.9}$$

Now that we have a way to compute the time correlations we can fit them to the data using the elements of $\mathbf{M}$ as free parameters. For each pair ξ_i and ξ_j we compute the correlation function and build the correlation matrix $\langle \boldsymbol{\xi}(t)\boldsymbol{\xi}^T(0) \rangle$. Figure 4.3 shows the measured correlation functions as solid lines. The uncertainty on each curve is calculated by dividing the trajectory into many shorter subtrajectories. For each subtrajectory we compute the correlation functions and compute their mean and the corresponding standard error (indicated by error bars in Figure 4.3). The cross correlations functions are small when compared to the typical variance of each component of $\boldsymbol{\xi}$ and thus have larger uncertainties than autocorrelations.

The fitted values of $\mathbf{M}$ are reported in Table 4.1. The coupling term $M_{y\phi}$ is different from zero because of the L-shaped arms connecting the helix to the

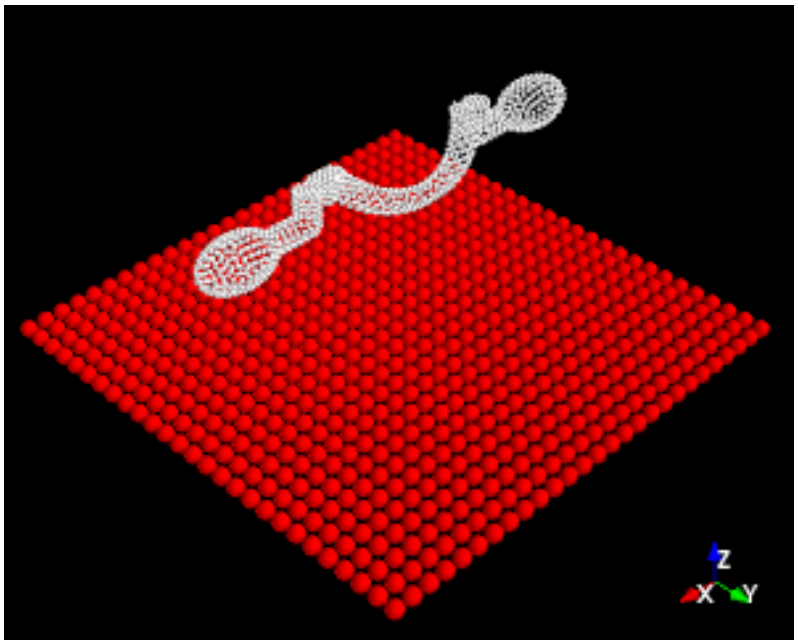

Figure 4.4. 3D view of the numerical model. Both the microhelix and the coverglass surface are represented as rigid clusters of spheres. The mobility matrix of the sphere cluster composing the helical structure has been computed using the Rotne-Prager method. [84, 51] Reproduced from Ref. [20].

handles; as the helix rotates around its axis, they L-shaped joints act as paddles pushing the fluid along the y axis. Such a coupling term would be zero if the tracking center coincides with the center of hydrodynamic stress [49] but here we are considering rotations along the helix axis. Because of the symmetry of our structure, we expect $M_{xy}, M_{y\theta}, M_{x\theta}, M_{\phi\theta}$ to be zero while the values reported in Table 4.1 are not. Such small discrepancies could originate from a minimal deformation that the helix structures may suffer when detached from the coverglass.

Since, in principle, all coordinates are coupled, each correlation function $\langle \xi_i(t)\xi_j(0)\rangle$ depends on all the elements of the matrix $\mathbf{M}$ so that fitting them simultaneously may be inaccurate if one of the curves presents large systematic tracking errors. As an alternative way to get $\mathbf{M}$ we can fit the cross-displacement matrix, which at short times takes the simple form:

$$\langle \mathbf{\Delta\xi}(t)\mathbf{\Delta\xi}^T(t)\rangle = \langle [\boldsymbol{\xi}(t) - \boldsymbol{\xi}(0)]\,[\boldsymbol{\xi}(t) - \boldsymbol{\xi}(0)]^T\rangle \approx k_B T(\mathbf{M} + \mathbf{M}^T)t \tag{4.10}$$

The above expression tells us that, at short times, the coordinates $\boldsymbol{\xi}$ undergo a free diffusion before experiencing the effects of the quadratic potential. During free diffusion, each curve $\langle \Delta\xi_i(t)\Delta\xi_j^T(t)\rangle$ depends only on a single element M_{ij} of the mobility matrix. To obtain M_{ij} we numerically compute the time derivative of $\langle \Delta\xi_i(t)\Delta\xi_j(0)\rangle$. We then fit the latter to an exponential function, which empirically reproduces our data, and divide its value at $t = 0$ by $2k_BT$. In Table 4.1 are listed the elements of $\mathbf{M}$ obtained by taking the time derivative of $\langle \mathbf{\Delta\xi}(t)\mathbf{\Delta\xi}^T(t)\rangle$ at $t = \delta t$ (where δt is inverse of the framerate). Most of the values of $\mathbf{M}$ are compatible with

Table 4.1. Comparison between experimental and computed values of the mobility matrix. Experimental values have been obtained both by fitting the correlation functions (see Figure 4.3) and by extrapolating the time derivative of the coordinates cross displacement for $t \to 0$ (see Eq. (4.10)). The computed mobility matrix for our structure is obtained using a Rotne-Prager method both in the absence and in the presence of a nearby bounding wall as explained in the text. The experimental correlation functions have been obtained by averaging the correlation functions of many subtrajectories. The uncertainty on the fitted values of **M** are obtained using the bootstrap method on the subtrajectories. Reproduced from Ref. [20].

Matrix term	Exp. (Correlation)	Exp. (MSD)	RP (Helix)	RP (Helix + Wall)	Units
M_{xx}	10.0±0.6	10.7±0.3	14.2	11.5	μm/(s pN)
M_{yy}	6.8±0.7	6.7±0.2	10.5	7.7	μm/(s pN)
M_{xy}	0.26±0.14	-0.67±0.05	-0.01	0.03	μm/(s pN)
$M_{\phi\phi}$	1.6±0.1	1.53 ±0.05	1.86	1.84	$(\mu\text{m s pN})^{-1}$
$M_{\theta\theta}$	0.094±0.004	0.03±0.001	0.12	0.12	$(\mu\text{m s pN})^{-1}$
$M_{\phi\theta}$	0.006±0.001	0.02±0.001	0	0.006	$(\mu\text{m s pN})^{-1}$
$M_{x\phi}$	-0.45±0.06	-0.26±0.05	-0.22	-0.24	$(\text{s pN})^{-1}$
$M_{y\phi}$	-0.22±0.005	0.20±0.02	0.36	0.3	$(\text{s pN})^{-1}$
$M_{x\theta}$	0.021±0.001	-0.26±0.015	0	0	$(\text{s pN})^{-1}$
$M_{y\theta}$	0.000±0.001	0.40±0.006	0	0	$(\text{s pN})^{-1}$

the ones obtained by fitting the correlation functions.

The values of **M** can be compared with the ones computed using the Rotne-Prager method. In brief the helix structure and the coverglass are represented as rigid clusters of close packed small spherical beads (see Figure 4.4). For a given configuration of beads a grand mobility matrix is calculated connecting forces and torques on every bead to the linear and angular speeds of all other beads [84, 51]. By imposing a rigid motion on all spheres in the cluster while setting to zero the speeds of the spheres in the wall cluster, the forces and the torques acting on each sphere are obtained by inverting the grand mobility matrix. The total force and torque on the helix are finally obtained by summing up force and torque contributions from every bead in the helix cluster. Results are listed in Table 4.1. When the presence of the coverglass is neglected,a significant mismatch between the measured and simulated values of the translational drag is found when the presence of the coverslip is not taken into account. The coverslip has been included in the simulation by placing a 30 μm×30 μm planar layer of spheres on which we impose a zero velocity condition. In Figure 4.4 we show a 3D view of the spheres composing the micro-helix and the coverslip placed at a distance of 8 μm from the helix axis. Table 4.1 lists the values of **M** when the Rotne-Prager method also includes the coverslip effects. It is clear that the structure-wall hydrodynamic interactions play an important role. Unfortunately we were not able to increase the helix-wall distance since, as we move away from the coverslip, the optical trap strengths degrade because of spherical aberrations [85]. At approximately 10 μm scattering force become dominant and the structure cannot be trapped stably for more than a few seconds.

Having assessed the importance of hydrodynamic effects of the wall on the

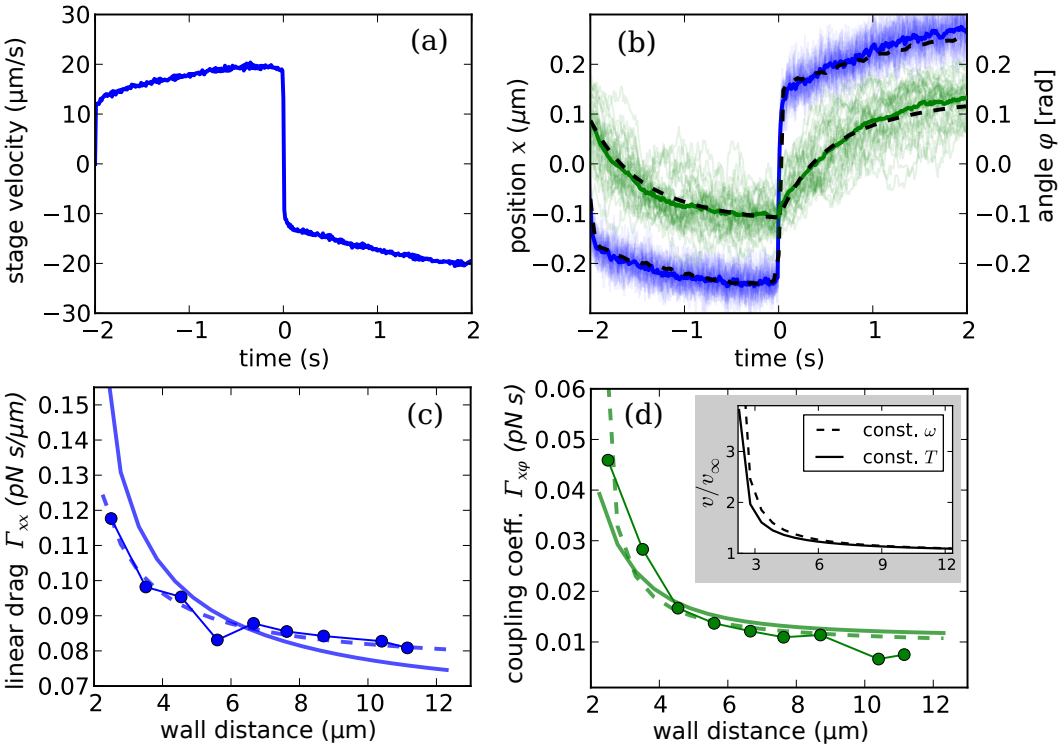

Figure 4.5. The piezoelectric stage is driven back and forth along the x direction while the structure is held in optical traps. (a) Velocity of the stage measured by its capacitive sensor. (b) Trajectories in x (blue) and ϕ (green). Brownian noise is filtered out by computing the average trajectory of x and ϕ plotted respectively as blue and green tick lines. Dashed lines plot a fit to the curve based on Eqs. 4.14 and 4.15. (c-d) Drag coefficients Γ_{xx} and $\Gamma_{x\phi}$ as a function of the distance between the coverglass and the helix axis. The same two quantities are computed using Rotne-Prager method and plotted as solid lines. Dashed line in (c) plots the best fit to the function $\gamma_\infty/(1-(9/16)a/z)$ (where a and γ_∞ are free parameters and z is the distance of the helix center from the coverslip); the same function is used to fit data point in (d). Inset in (d) plots the predicted linear velocity of an helical structure that rotates with a constant torque (solid line) or a constant speed (dashed line) at different wall separations. Reproduced from Ref. [20].

structure, we now want to study the dependence of the mobility as a function of the distance. In particular we are interested in the roto-translational coupling coefficient. To do this, we trapped our structure at a controlled distance from the coverslip and tracked it while the piezoelectric stage translated the sample along the x axis back and forth. Figure 4.5(a) shows the velocity v_{stage} of the piezoelectric stage as a function of time. Each back and forth cycle was repeated 40 times for each distance. Figure 4.5(b) shows 40 tracks of x and ϕ, each corresponding to a back and forth cycle, plotted respectively as blue and green thin lines. The tracks can be averaged to eliminate the Brownian noise and obtain a mean $x(t)$ and $\phi(t)$ which are plotted respectively as blue and green thick solid lines. If the Brownian noise is averaged out we can remove the stochastic term in Eq. (4.6) and include the effects of the translating stage by adding the external force $\mathbf{f} = \boldsymbol{\Gamma}\boldsymbol{v}$ where $\boldsymbol{\Gamma} = \mathbf{M}^{-1}$ and

$\boldsymbol{\upsilon} = (v_{\text{stage}}, 0, 0, 0)$:

$$\boldsymbol{\Gamma}\dot{\boldsymbol{\xi}} = -\mathbf{K}\boldsymbol{\xi} + \boldsymbol{\Gamma}\boldsymbol{\upsilon} \tag{4.11}$$

As a first approximation we neglect all the coupling terms in $\boldsymbol{\Gamma}$ except $\Gamma_{x\phi}$ and use the approximations $\Gamma_{xx}\dot{x} \gg \Gamma_{x\phi}\dot{\phi}$ and $\Gamma_{\phi\phi}\dot{\phi} \gg \Gamma_{x\phi}\dot{x}$ to simplify (4.11) to:

$$\Gamma_{xx}\dot{x} = -K_{xx}x + \Gamma_{xx}v \tag{4.12}$$

$$\Gamma_{\phi\phi}\dot{\phi} = -K_{\phi\phi}\phi + \Gamma_{x\phi}v \tag{4.13}$$

whose solutions are :

$$x(t) = x(0)e^{-t/\tau_x} + \int dt' v(t') e^{-(t-t')/\tau_x} \tag{4.14}$$

$$\phi(t) = \phi(0)e^{-t/\tau_\phi} + A\int dt' v(t') e^{-(t-t')/\tau_\phi} \tag{4.15}$$

where $\tau_x = \Gamma_{xx}/K_{xx}$, $\tau_\phi = \Gamma_{\phi\phi}/K_{\phi\phi}$ and $A = \Gamma_{x\phi}/\Gamma_{\phi\phi}$. Although this simplified model provides a very good fit to the data in Figure 4.5(b), the drag coefficients $\Gamma_{xx}, \Gamma_{\phi\phi}, \Gamma_{x\phi}$ obtained from the best fit parameters τ_x, τ_ϕ and A may not be quantitatively accurate because of the approximations involved. Since the trapping force field is linear in the explored range of displacements, we can follow a more straightforward way to extract Γ_{xx} and $\Gamma_{x\phi}$ which does not require the above approximations on the drag coefficients. After an exponential transient the average displacements of all the coordinates $\langle\xi_j\rangle$ are proportional to the stage velocity i.e. $\sum_j K_{ij}\langle\xi_j\rangle = \Gamma_{ix}v_{\text{stage}}$. For each distance from the coverglass, a 5 minutes movie at 100 fps was acquired while the stage was not moving and K_{ij} is obtained as in Eq. (4.5). The values of Γ_{xx} and $\Gamma_{x\phi}$ are plotted respectively as blue dots in Figure 4.5(c) and green dots in Figure 4.5(d). The same two quantities computed using Rotne-Prager method are also plotted in Figs. 4.5(c-d) as solid lines. The two curves are comparable but the agreement is not perfect. The drag on a sphere of radius a moving parallel to a no-slip wall at a distance z from the sphere's center can be approximated by $\gamma_{\parallel} = \gamma_\infty/(1 - (9/16)a/z)$ [63] where γ_∞ is the the drag in the bulk. Using this expression as a phenomenological fitting function we can fit the experimental values of Γ_{xx} (dashed line in Figure 4.5(c)) and obtain the effective parameters $a = 1.75$ μm and $\gamma_\infty = 0.084$ pNs/μm. The value a is close to the helix radius (approximately 2 μm). We fit $\Gamma_{x\phi}$ using the same functional form and obtain the curve plotted by dashed line in Figure 4.5(d) with parameters $a = 4.3$ μm and $\gamma_\infty = 0.084$ pNs. The length scale here is closer to the helix half-length (5.7 μm).

From systems in nature that have evolved for optimizing swimming at the micro scale[62] to the design of synthetic micro-swimmers[47, 123], micro-helices are often used as propellers. The fact that $\Gamma_{x\phi}$ increases as the helix approaches the wall implies that wall effects enhance the thrust force generated by a helical propeller rotating with a constant angular speed ω. Considering only the x and ϕ coordinates, the relation between linear speed v and ω for a force-free helix is $\Gamma_{xx}v + \Gamma_{x\phi}\omega = 0$ so that $v = -\omega\Gamma_{x\phi}/\Gamma_{xx}$. Although the drag coefficient Γ_{xx} also increases when approaching a wall, the self propulsion speed still grows as the wall distance decreases (see dashed line in inset of Fig 4.5(d)). Biological propellers, such

as bacterial flagella, are driven by a constant torque [27]. In this case both ω and v are derived by expressing the applied torque as $T = \Gamma_{x\phi} v + \Gamma_{\phi\phi}\omega$. The resulting self propulsion speed for a fixed T is $v = -T\Gamma_{x\phi}/(\Gamma_{xx}\Gamma_{\phi\phi} - \Gamma_{x\phi}^2) \approx -T(\Gamma_{x\phi}/\Gamma_{xx}\Gamma_{\phi\phi})$ where the drag coefficient $\Gamma_{\phi\phi}$ also increases close to walls. Since we cannot measure directly $\Gamma_{\phi\phi}$ we use simulations based on the Rotne-Prager method to obtain a reliable guess. We find that $\Gamma_{x\phi}$ compensates for all these drag increments (Γ_{xx} and $\Gamma_{\phi\phi}$) resulting in a self propulsion speed that increases near the wall as shown in inset of Figure 4.5(d). A direct measurement of $\Gamma_{\phi\phi}$ would require the possibility of either rotating the sample stage or applying a controlled torque on the helix, for example through radiation pressure [8]. The information on the drag coefficients coupling x and ϕ coordinate would still be the same due to the symmetry properties of the resistance and mobility matrices.

4.4 Conclusions

Using two-photon lithography we fabricated rigid an deformable helical structures connected to handles for optical trapping. We recorded the Brownian fluctuations of a trapped rigid structure and extracted its drag coefficients by fitting the time correlation functions and the mean squared displacements of all coordinates. Our structure was then trapped at various distances from the coverslip and dragged through the fluid by moving the stage. From this last experiment we obtained the translational drag coefficient Γ_{xx} and the roto-translational coupling coefficient $\Gamma_{x\phi}$ as a function of the distance from a no-slip boundary. Finally, we find that as the helix-wall distance is reduced $\Gamma_{x\phi}$ grows more rapidly than Γ_{xx} and $\Gamma_{xx}\Gamma_{\phi\phi}$ and concluded that when a helix is rotated at a constant speed or it is subject to a fixed external torque its velocity grows as it moves closer to a no-slip wall. By studying relaxation after stretching in deformable helices we found an overdamped, almost single exponential dynamics resulting from a drag coefficient that is only weakly dependent on extension.

Chapter 5

Critical Casimir Forces probes

The work in this chapter was done in collaboration with Alessandro Magazzu, Giovanni Volpe and Roberto Di Leonardo.

In the present chapter we propose a novel microprobe design for studying critical Casimir forces. Using optical tweezers we trap a probe and by tracking its position we determine the optical features of the microstructure. Finally, experiments with microprobes immersed in a binary liquid mixture were developed.

5.1 Critical Casimir forces

At macroscopic scales thermal fluctuations of a physical property of a system are typically negligible. In contrast, at the micrometer and nanometer scales fluctuations become generally relevant and they give rise to novel and intriguing phenomena such as critical Casimir effect. Critical Casimir forces [39] are the thermodynamic correspondent to quantum-electrodynamical Casimir forces, it acts between surfaces immersed in a binary liquid mixture amidst to its critical point and arises from the confinement of concentration fluctuations within the thin film of fluid separating the surfaces [45].

In 2008, Hertlein *et al.* were able to measure the critical Casimir forces between the interaction of a single sphere and a plate[50]. Figure 5.1 shows the experimental set-up and some results from their work. They calculate critical Casimir forces by means of total internal reflection microscopy (TIRM) obtaining measurements with femtonewton resolution. The medium of immersion used is a binary liquid mixture with a lower critical demixing point at $T_c \backsimeq 307K$. at a lutidine mass fraction of $c_L^c = 0.286$. The binary mixture can be considered as an effectively homogeneous solvent for temperatures far below the demixing line temperatures, thus critical Casimir forces are not present.

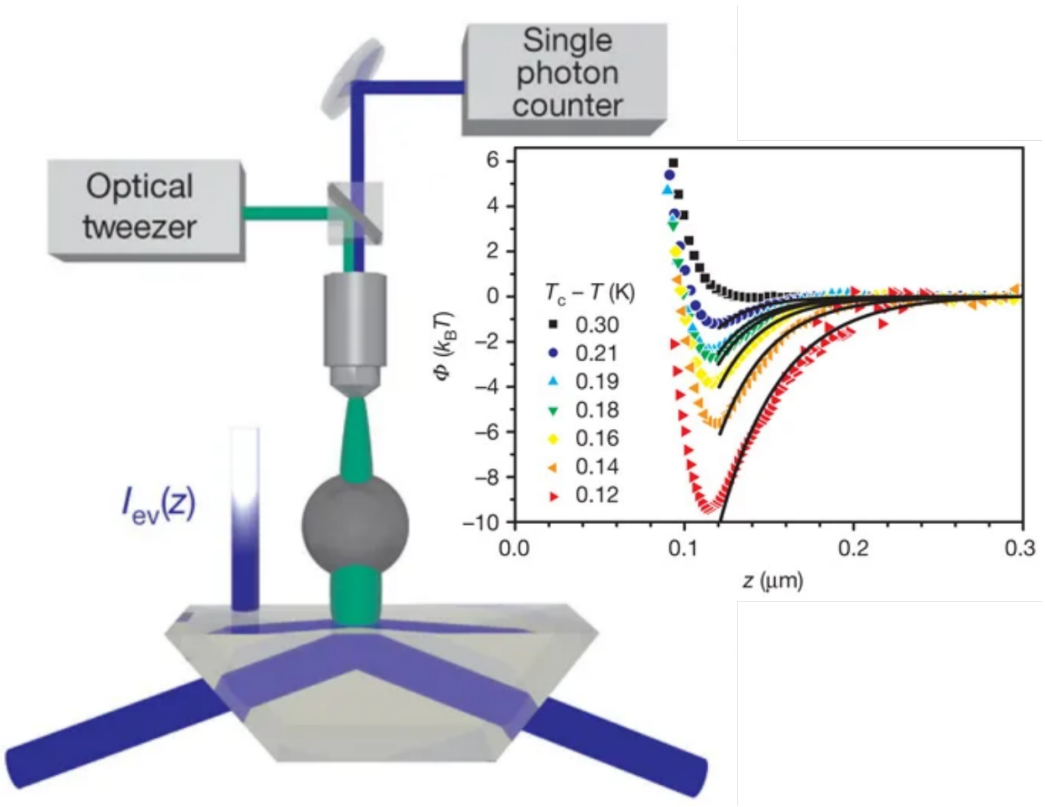

Figure 5.1. Critical Casimir forces measurement between a colloidal sphere and a rigid surface. Scheme of TIRM set-up for studying a colloidal particle interacting with a flat silica surface. A binary mixture near its critical point is used as medium. Inset: Critical Casimir potentials between a wall and a particle for symmetric boundary conditions. Modified from ref[50]

So far, most of the experiments and proposed models for studying critical Casimir Forces consider the interaction between simple geometrical objects such as two spheres[90, 72], and the mentioned case of a single sphere and a plate. In the present work we propose a more complex object to measure critical Casimir forces between two plates.

5.2 Microprobe characterization by optical trapping

The novel 3D microprobe was fabricated by two-photon polymerization technique, the microstructure can be optically trapped to directly measure effective forces and torques between colloidal objects with non spherical shapes. The microprobe is composed of three main elements: one cube with 5 μm size side, and two spheroids (connected to the cube) with a minor axis of 1 μm and a mayor axis of 1.5 μm. The microfabrication parameters are laser power of 2 mW and the scanning speed varied between 24 and 40 $^{\mu m}/_{s}$.

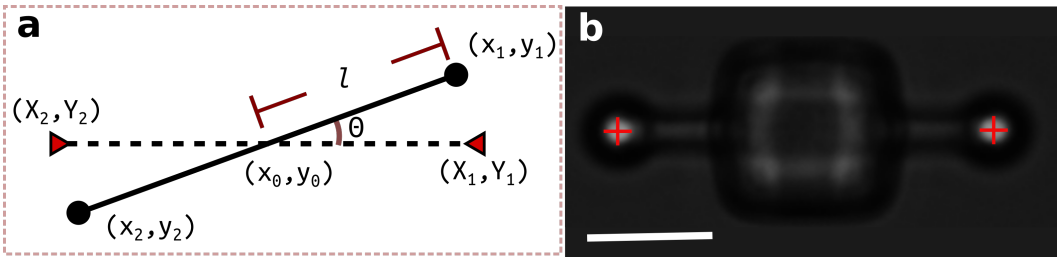

Figure 5.2. Design of a 3D microprobe for critical Casimir forces and simplified model.(a)Diagram of the spheroids and optical tweezers positions. The red triangular marks are the position of the optical tweezers (X_i, Y_i), while the circular marks are the position of the spheroids (x_i, y_i), with $i = 1, 2$. The distance between the center of mass (x0,y0) of the system and the spheroid on the side is equal to l. (b) Single frame from the tracking video of the microprobe. The red crosses represent the position of the optical traps. The scale bar is 5 μm.

In a simplified model of the microstructure under the influence of optical tweezers, we find three degrees of freedom: x_0 and y_0 center of mass coordinates, and the angle θ. The in-plane coordinates of the two spheroids are denominated (x_1, y_1) and (x_2, y_2), while the middle point of the segment joining the two handles corresponds to the center of mass coordinates (x_0, y_0) (Figure 5.2a). The third degree of freedom is the in-plane orientation of the microprobe which is computed as the angle between the line connecting the two handles and the x axis: $\theta = \arctan\left[(y_2 - y_0)/(x_2 - x_0)\right]$. Thus, the two spheroids coordinates are defined as:

$$\begin{aligned} x_1 &= x_0 + lcos(\theta) \quad & x_2 &= x_0 - lcos(\theta) \\ y_1 &= y_0 + lsin(\theta) \quad & y_2 &= y_0 - llsin(\theta) \end{aligned}$$

while the potential energy of the system will be:

$$U = \frac{1}{2}k\left[(x_1 - X_1)^2 + (x_2 - X_2)^2 + (y_1 - Y_1)^2 + (y_2 - Y_2)^2\right]$$

after considering first order approximation of the trigonometric functions, the form of the potential energy is:

$$U = k\left[x_0^2 + y_0^2 + l^2\theta^2\right] \tag{5.1}$$

The experimental setup used for studying the microprobe is the same standard optical microscope coupled with an IR holographic optical tweezers setup employed in section 4. The two spheroids at the extremities of the microprobe serve both as handles for optical trapping and for tracking. The Casimir probe is positioned horizontally approximately 1.5 μm above the focal plane as shown in Figure 5.2b. With the microstructure in this position, the two spheroids generate bright blobs which can be efficiently tracked using a center of mass algorithm.

Once the microprobe is trapped by optical tweezers, a video at 90 fps for 10 minutes is recorded. From the position values, the histograms for each degree of freedom are computed (Figure 5.3). From the comparison between Figure 5.3a and 5.3b it is evident that fluctuations for y_0 are larger than fluctuations on x_0

coordinate. Such variability could be originated from the microprobe configuration: given the along x-axis orientation of the two handles the coordinate x_0 is more confined than y_0 which results in a wider range of motion on the last coordinate. Finally, using the information from each histogram we fitted a Gaussian function to each degree of freedom (data not shown) which is a consequence of Eq. 5.1. A possible addressing for reducing y_0 fluctuations is to fabricate a third handle on the microprobe, in a way that there is a single free surface for developing critical Casimir forces experiments and the center of mass coordinates are similarly confined.

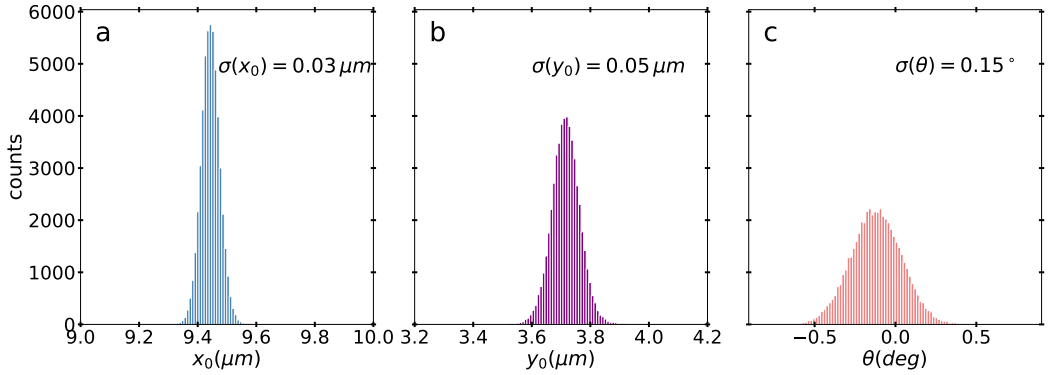

Figure 5.3. Histograms of the microprobe degrees of freedom. Histograms for (a) the coordinate x_0, (b) y_0, and (c) θ.

5.3 Testing microprobe in a binary liquid mixture

The experiment for characterizing the microprobe was realized with a double distilled water sealed sample. For studying and measuring critical Casimir forces it is necessary to confine the structures on a sealed sample using a binary liquid mixture, thus for the following experiments the structures were immersed in a critical mixture of water and 2,6-lutidine at the critical lutidine mass fraction $c_L^c = 0.286$, corresponding to a lower critical point at the temperature $T_c \backsimeq 34\ ^\circ C$. We tested our microprobes on the same optical set-up employed in reference [72] which consists of three main parts: holographic optical tweezers, a digital video-microscope, and a temperature control unit.

Since the microprobes are fabricated attached to the coverglass, a preliminary step before sealing the sample consists in detaching the microstructures by using a thin plastic fishing thread[1]. The sample is composed by a cavity slide[2] enclosed with the coverglass where microprobes are immersed in the binary liquid mixture. Figure 5.4 shows the sequence of eight frames extracted from a video recorded at 15 fps during 16 minutes. The process of aligning two microprobes for measuring critical Casimir forces is composed of several steps: once a single microstructure is localized, a second probe must be placed near the first one, on Figure 5.4a the upper microstructure is trapped by holographic optical tweezers, a second probe is

[1] When these experiments were made, the protocol for a water-soluble sacrificial layer had not been developed already.

[2] `https://www.sigmaaldrich.com/IT/en/product/aldrich/br475505`

positioned near to the first one by moving the 2D stage from the optical set-up; the following step is to halt optical tweezers on the first microprobe, and place both microstructures outside of optical tweezers area as shown in Figure 5.4b-c; after defining the position of four holographic optical tweezers for the handles of each microprobe, structures are placed near this area with the laser beam blocked, then we optically trap them (Figure 5.4d-e); and finally, by changing the coordinates of the optical traps, the distance between the microprobes is progressively decreased as presented in Figure 5.4f-h.

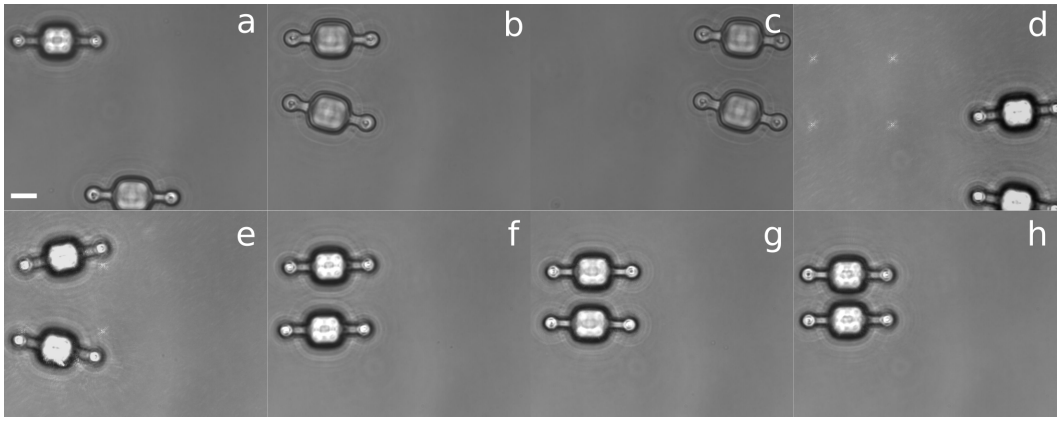

Figure 5.4. Two microprobes in a binary liquid mixture. Bright field images of two microprobes immersed in a critical mixture of water and 2,6-lutidine. (a)-(d) (e)-(h) Approaching of two microparticles by the use of optical tweezers. The scale bar is 5 μm.

The positions of the traps must be such that the microprobes are separated a few 100 of nanometers from each other. The microstructures trajectory is measured with a fixed temperature T by recording the position of the microprobes. We repeated this process for different temperatures in a way that $T_C - T$ progressively approaches to 0. For each temperature, the coordinates of the microprobe can be extracted from the videos by a center of mass algorithm, from the distribution of the center-to-center distance it is possible to obtain the critical Casimir potential. Given the limited number of microstructures we performed the experiment only once, unfortunately one of the microprobes was not tightly trapped, driven it out of the optical tweezers at the middle of the measurement.

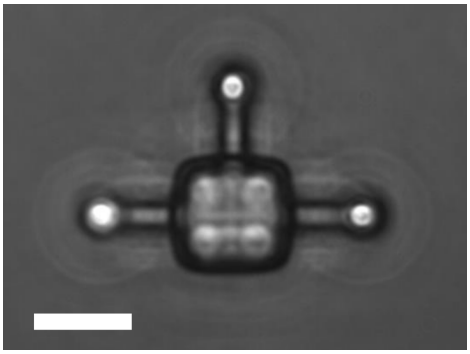

Figure 5.5. Three-handle microprobe. Bright field image of a optically trapped microprobe with a third handle. The scale bar is 5 μm.

Derived from the characterization experiment of the microprobe, a variant model was designed: we fabricated a microstructures with a third handle with the purpose of testing its stability in comparison with the original microprobe design. Figure 5.5 shows a bright field image of one of these three-handles microstructures immersed in

the binary liquid mixture. Given the method for detaching the microprobes from the coverglass (freeing them from the substrate by the use of a thin plastic thread), a common issue was to localize a reduced number of free-floating structures in the bulk, thus, only one three-handle was trapped. Nevertheless, transporting this modified microprobe demonstrated to be more stable when moving through the sample in both directions x and y.

5.4 Conclusions

By the use of two-photon polymerization we fabricated microcubes connected to handles for facilitating optical trapping and tracking. When two of these microprobes are separated by a distance of the order of hundred of nanometers and immersed in a binary liquid mixture, critical Casimir forces can be measured as long as the temperature in the sample verge to the critical temperature T_c. In the first part of this chapter, we characterized the microprobe stability, the center of mass coordinates distribution suggested that implementing a third handle could improve the y axis movement. From experiments using the initial design containing only two handles, we observed that fabricating a third handle in one of the free available faces of the cube improves the microprobe confinement and stabilization. Now that this microprobe design has been optimized, in the future experiments it will be possible to study critical Casimir forces between two plates as well as the induced torques, and force dependence on variable and controlled roughness of the contact surface.

Bibliography

[1] Adler, J. Chemotaxis in bacteria. *Science*, **153** (1966), 708.

[2] Adler, J. Galvanotaxis in bacteria. *Cold Spring Harbor Symposia on Quantitative Biology*, **53 Pt. I** (1988), 23.

[3] Aegerter, M. A. and Mennig, M. *Sol-Gel Technologies for Glass Producers and Users*. Springer US (2004).

[4] Alon, U., Camarena, L., Surette, M. G., Aguera y Arcas, B., Liu, Y., Leibler, S., and Stock, J. B. Response regulator output in bacterial chemotaxis. *The EMBO Journal*, **17** (1998), 4238.

[5] Andrianantoandro, E., Basu, S., Karig, D., and Weiss, R. Synthetic biology: New engineering rules for an emerging discipline. *Molecular Systems Biology*, **2** (2006), 2006.0028.

[6] Armitage, J. P. and Hellingwerf, K. Light-induced behavioral responses ("phototaxis") in prokaryotes. *Photosynthesis Research*, **76** (2003), 145.

[7] Armstrong, J. B. and Adler, J. Location of genes for motility and chemotaxis on the escherichia coli genetic map. *Journal of Bacteriology*, **97** (1969), 156.

[8] Asavei, T., Nieminen, T. A., Loke, V. L., Stilgoe, A. B., Bowman, R., Preece, D., Padgett, M. J., Heckenberg, N. R., and Rubinsztein-Dunlop, H. Optically trapped and driven paddle-wheel. *New Journal of Physics*, **15** (2013), 063016.

[9] Baldacchini, T. *Three-Dimensional Microfabrication Using Two-Photon Polymerization: Fundamentals, Technology, and Applications*. William Andrew (2015).

[10] Béjà, O., Spudich, E. N., Spudich, J. L., Leclerc, M., and DeLong, E. F. Proteorhodopsin phototrophy in the ocean. *Nature*, **411** (2001), 786.

[11] Béjà, O., et al. Bacterial rhodopsin: Evidence for a new type of phototrophy in the sea. *Science*, **289** (2000), 1902.

[12] Benner, S. A. and Sismour, A. M. Synthetic biology. *Nature Reviews Genetics*, **6** (2005), 533.

[13] Berg, H. C. *E. coli in motion*. Springer (2004).

[14] Berg, H. C. and Brown, D. A. Chemotaxis in escherichia coli analysed by three-dimensional tracking. *Nature*, **239** (1972), 500.

[15] Berg, H. C. and Purcell, E. M. Physics of chemoreception. *Biophys. J.*, **20** (1977), 193.

[16] Berg, H. C. and Turner, L. Chemotaxis of bacteria in glass capillary arrays. escherichia coli, motility, microchannel plate, and light scattering. *Biophysical Journal*, **58** (1990), 919.

[17] Berg, J. M., Tymoczko, J. L., and Stryer, L. *Biochemistry*, chap. 34. Molecular Motors. W. H. Freeman, New York, 5 edn. (2002). Section 34.2 Myosins Move Along Actin Filaments.

[18] Berg, J. M., Tymoczko, J. L., and Stryer, L. *Biochemistry*, chap. 34. Molecular Motors. W. H. Freeman, New York, 5 edn. (2002). Section 34.3 Kinesin and Dynein Move Along Microtubules.

[19] Betancourt, T. and Brannon-Peppas, L. Micro- and nanofabrication methods in nanotechnological medical and pharmaceutical devices. *Int. J. Nanomedicine*, **1** (2006), 483.

[20] Bianchi, S., Carmona Sosa, V., Vizsnyiczai, G., and Di Leonardo, R. Brownian fluctuations and hydrodynamics of a microhelix near a solid wall. *Scientific Reports*, **10** (2020), 4609.

[21] Bianchi, S., Saglimbeni, F., Lepore, A., and Di Leonardo, R. Polar features in the flagellar propulsion of E. coli bacteria. *Physical Review E*, **91** (2015), 062705.

[22] Bianchi, S., Vizsnyiczai, G., Ferretti, S., Maggi, C., and Di Leonardo, R. An optical reaction micro-turbine. *Nature Communications*, **9** (2018), 4476.

[23] Blakemore, R. Magnetotactic bacteria. *Science*, **190** (1975), 377.

[24] Ceylan, H., Giltinan, J., Kozielski, K., and Sitti, M. Mobile microrobots for bioengineering applications. *Lab Chip*, **17** (2017), 1705.

[25] Chao-Min, C. and Ren-Haw, C. Development behaviours and microstructure quality of downward-development in deep x-ray lithography. *Journal of Micromechanics and Microengineering*, **11** (2001), 692.

[26] Chattopadhyay, S., Moldovan, R., Yeung, C., and Wu, X. Swimming efficiency of bacterium escherichiacoli. *Proceedings of the National Academy of Sciences*, **103** (2006), 13712.

[27] Chen, X. and Berg, H. C. Torque-speed relationship of the flagellar rotary motor of escherichia coli. *Biophysical Journal*, **78** (2000), 1036.

[28] Datsenko, K. A. and Wanner, B. L. One-step inactivation of chromosomal genes in escherichia coli k-12 using pcr products. *Proceedings of the National Academy of Sciences*, **97** (2000), 6640.

[29] de Gennes, P. G. Chemotaxis: the role of internal delays. *Eur. Biophys. J.*, **33** (2004), 691.

[30] Dellmann, L., Roth, S., Beuret, C., Racine, G.-A., Lorenz, H., Despont, M., Renaud, P., Vettiger, P., and de Rooij, N. Fabrication process of high aspect ratio elastic structures for piezoelectric motor applications. In *Proceedings of International Solid State Sensors and Actuators Conference (Transducers '97)*, vol. 1, pp. 641–644 vol.1 (1997).

[31] Denk, W., Strickler, J., and Webb, W. Two-photon laser scanning fluorescence microscopy. *Science*, **248** (1990), 73.

[32] Dewitt, S. K. and Adelberg, E. A. The occurrence of a genetic transposition in a strain of escherichia coli. *Genetics*, **46** (1962), 577.

[33] Drescher, K., Dunkel, J., Cisneros, L. H., Ganguly, S., and Goldstein, R. E. Fluid dynamics and noise in bacterial cell-cell and cell-surface scattering. *Proceedings of the National Academy of Sciences*, **108** (2011), 10940.

[34] Dreyfus, R., Baudry, J., Roper, M. L., Fermigier, M., Stone, H. A., and Bibette, J. Microscopic artificial swimmers. *Nature*, **437** (2005), 862.

[35] Duan, W., Wang, W., Das, S., Yadav, V., Mallouk, T. E., and Sen, A. Synthetic nano- and micromachines in analytical chemistry: Sensing, migration, capture, delivery, and separation. *Annual Review of Analytical Chemistry*, **8** (2015), 311.

[36] Dusenbery, D. B. *Living at Micro Scale: the Unexpected Physics of Being Small*. Harvard University Press (2011).

[37] Ebeling, D., van den Ende, D., and Mugele, F. Electrostatic interaction forces in aqueous salt solutions of variable concentration and valency. *Nanotechnology*, **22** (2011), 305706.

[38] Farsari, M. and Chichkov, B. N. Two-photon fabrication. *Nature Photonics*, **3** (2009), 450.

[39] Fisher, M. E. and De Gennes, P.-G. Wall phenomena in a critical binary mixture. *C. R. Seances Acad. Sci, Ser. B*, **287** (1978), 207.

[40] Friedrich, T., Geibel, S., Kalmbach, R., Chizhov, I., Ataka, K., Heberle, J., Engelhard, M., and Bamberg, E. Proteorhodopsin is a light-driven proton pump with variable vectoriality. *Journal of Molecular Biology*, **321** (2002), 821.

[41] Frymier, P. D. and Ford, R. M. Analysis of bacterial swimming speed approaching a solid–liquid interface. *AIChE Journal*, **43** (1997), 1341.

[42] Frymier, P. D., Ford, R. M., Berg, H. C., and Cummings, P. T. Three-dimensional tracking of motile bacteria near a solid planar surface. *Proceedings of the National Academy of Sciences*, **92** (1995), 6195.

[43] Fuhrman, J. A., Schwalbach, M. S., and Stingl, U. Proteorhodopsins: an array of physiological roles? *Nature Reviews Microbiology*, **6** (2008), 488.

[44] Gabel, C. V. and Berg, H. C. The speed of the flagellar rotary motor of escherichia coli varies linearly with protonmotive force. *Proceedings of the National Academy of Sciences*, **100** (2003), 8748.

[45] Ganshin, A., Scheidemantel, S., Garcia, R., and Chan, M. H. W. Critical casimir force in ^{4}He films: Confirmation of finite-size scaling. *Phys. Rev. Lett.*, **97** (2006), 075301.

[46] Ghosh, A. and Fischer, P. Controlled propulsion of artificial magnetic nanostructured propellers. *Nano Letters*, **9** (2009), 2243.

[47] Ghosh, A. and Fischer, P. Controlled propulsion of artificial magnetic nanostructured propellers. *Nano letters*, **9** (2009), 2243.

[48] Hahn, V., Kiefer, P., Frenzel, T., Qu, J., Blasco, E., Barner-Kowollik, C., and Wegener, M. Rapid assembly of small materials building blocks (voxels) into large functional 3d metamaterials. *Advanced Functional Materials*, **30** (2020), 1907795.

[49] Happel, J. and Brenner, H. *Low Reynolds number hydrodynamics: with special applications to particulate media*, vol. 1. Springer Science & Business Media (2012).

[50] Hertlein, C., Helden, L., Gambassi, L., Dietrich, S., and Bechinger, C. Direct measurement of critical casimir forces. *Nature*, **451** (2008), 172.

[51] Holm, C. and Kremer, K. *Advanced computer simulation approaches for soft matter sciences III*, vol. 221. Springer (2008).

[52] Hwang, G., et al. Electro-osmotic propulsion of helical nanobelt swimmers. *The International Journal of Robotics Research*, **30** (2011), 806.

[53] Häder, D. P. Photosensory behavior in procaryotes. *Microbiological Reviews*, **51** (1987), 1.

[54] Ikeda, T., Oosawa, K., and Hotani, H. Self-assembly of the filament capping protein, flid, of bacterial flagella into an annular structure. *Journal of Molecular Biology*, **259** (1996), 679.

[55] Israelachvili, J. N. *Intermolecular and Surface Forces*. Academic Press (2011).

[56] Izdebska-Podsiadły, J. Chapter 6 - application of plasma in printed surfaces and print quality. In *Non-Thermal Plasma Technology for Polymeric Materials* (edited by S. Thomas, M. Mozetič, U. Cvelbar, P. Špatenka, and P. K.M.), pp. 159–191. Elsevier (2019).

[57] Kaiser, W. and Garrett, C. G. B. Two-photon excitation in caf$_2$: eu^{2+}. *Phys. Rev. Lett.*, **7** (1961), 229.

[58] Khripin, C. Y., Brinker, C. J., and Kaehr, B. Mechanically tunable multiphoton fabricated protein hydrogels investigated using atomic force microscopy. *Soft Matter*, **6** (2010), 2842.

[59] Kim, S. Y., Waschuk, S. A., Brown, L. S., and Jung, K.-H. Screening and characterization of proteorhodopsin color-tuning mutations in escherichia coli with endogenous retinal synthesis. *Biochimica et Biophysica Acta (BBA) - Bioenergetics*, **1777** (2008), 504.

[60] Lauga, E. Bacterial hydrodynamics. *Annual Review of Fluid Mechanics*, **48** (2016), 105.

[61] Lauga, E., DiLuzio, W. R., Whitesides, G. M., and Stone, H. A. Swimming in circles: motion of bacteria near solid boundaries. *Biophysical Journal*, **90** (2006), 400.

[62] Lauga, E. and Powers, T. R. The hydrodynamics of swimming microorganisms. *Reports on Progress in Physics*, **72** (2009), 096601.

[63] Leach, J., Mushfique, H., Keen, S., Di Leonardo, R., Ruocco, G., Cooper, J., and Padgett, M. Comparison of faxén's correction for a microsphere translating or rotating near a surface. *Physical Review E*, **79** (2009), 026301.

[64] Leite, F., Bueno, C., Da Róz, A., Ziemath, E., and Oliveira, J., O.N. Theoretical models for surface forces and adhesion and their measurement using atomic force microscopy. *Int. J. Mol. Sci.*, **13** (2012), 12773.

[65] Levskaya, A., et al. Engineering escherichia coli to see light. *Nature*, **438** (2005), 441.

[66] Li, G. and Tang, J. X. Low flagellar motor torque and high swimming efficiency of caulobacter crescentus swarmer cells. *Biophysical Journal*, **91** (2006), 2726.

[67] Lighthill, J. *Mathematical biofluiddynamics*, vol. 17. Siam (1975).

[68] Ligon, S. C., Husár, B., Wutzel, H., Holman, R., and Liska, R. Strategies to reduce oxygen inhibition in photoinduced polymerization. *Chemical Reviews*, **114** (2014), 557.

[69] Linder, V., Gates, B. D., Ryan, D., Parviz, B. A., and Whitesides, G. M. Water-soluble sacrificial layers for surface micromachining. *Small*, **1** (2005), 730.

[70] Madou, M. J. *Fundamentals of microfabrication: the science of miniturization*. CRC Press (2007).

[71] Maeda, K., Imae, Y., Shioi, J. I., and Oosawa, F. Effect of temperature on motility and chemotaxis of escherichia coli. *Journal of Bacteriology*, **127** (1976), 1039.

[72] Magazzù, A., Callegari, A., Staforelli, J. P., Gambassi, A., Dietrich, S., and Volpe, G. Controlling the dynamics of colloidal particles by critical casimir forces. *Soft Matter*, **15** (2019), 2152.

[73] Martel, S., Felfoul, O., Mathieu, J.-B., Chanu, A., Tamaz, S., Mohammadi, M., Mankiewicz, M., and Tabatabaei, N. MRI-based medical nanorobotic platform for the control of magnetic nanoparticles and flagellated bacteria for target interventions in human capillaries. *Int. J. Rob. Res.*, **28** (2009), 1169.

[74] Maruo, S., Nakamura, O., and Kawata, S. Three-dimensional microfabrication with two-photon-absorbed photopolymerization. *Opt. Lett.*, **22** (1997), 132.

[75] Matusiak, J. and Grządka, E. Stability of colloidal systems-a review of the stability measurements methods. *Annales - Universitatis Mariae Curie-Sklodowska, Sectio AA*, **LXXII** (2017), 33.

[76] Nelson, B. J., Dong, L., and Arai, F. *Springer Handbook of Robotics*, chap. Micro \Nanorobots, pp. 411–450. Springer Berlin Heidelberg, Berlin, Heidelberg (2008).

[77] Paster, E. and Ryu, W. S. The thermal impulse response of escherichia coli. *Proceedings of the National Academy of Sciences of the United States of America*, **105** (2008), 5373.

[78] Pelli, S., Righini, G. C., Scaglione, A., Guglielmi, M., and Martucci, A. Direct laser writing of ridge optical waveguides in silica-titania glass sol-gel films. *Optical Materials*, **5** (1996), 119.

[79] Pitts, J. D., Campagnola, P. J., Epling, G. A., and Goodman, S. L. Submicron multiphoton free-form fabrication of proteins and polymers: studies of reaction efficiencies and applications in sustained release. *Macromolecules*, **33** (2000), 1514.

[80] Pitts, J. D., Howell, A. R., Taboada, R., Banerjee, I., Wang, J., Goodman, S. L., and Campagnola, P. J. New photoactivators for multiphoton excited three-dimensional submicron cross-linking of proteins: Bovine serum albumin and type 1 collagen. *Photochemistry and Photobiology*, **76** (2002), 135.

[81] Purcell, E. M. Life at low reynolds number. *American Journal of Physics*, **45** (1977), 3.

[82] Purcell, E. M. The efficiency of propulsion by a rotating flagellum. *Proceedings of the National Academy of Sciences*, **94** (1997), 11307.

[83] Qiu, F., Fujita, S., Mhanna, R., Zhang, L., Simona, B. R., and Nelson, B. J. Magnetic helical microswimmers functionalized with lipoplexes for targeted gene delivery. *Advanced Functional Materials*, **25** (2015), 1666.

[84] Reichert, M. *Hydrodynamic Interactions in Colloidal and Biological Systems*. Ph.D. thesis, Universitat Konstanz, Konstanz (2006).

[85] Reihani, S. N. S. and Oddershede, L. B. Optimizing immersion media refractive index improves optical trapping by compensating spherical aberrations. *Optics Letters*, **32** (2007), 1998.

[86] Risken, H. Fokker-planck equation. In *The Fokker-Planck Equation*, pp. 63–95. Springer (1996).

[87] Rocha, L., Velho, L., and Carvalho, P. C. P. Image moments-based structuring and tracking of objects. In *Proceedings. XV Brazilian Symposium on Computer Graphics and Image Processing*, pp. 99–105 (2002).

[88] Rodenborn, B., Chen, C.-H., Swinney, H. L., Liu, B., and Zhang, H. Propulsion of microorganisms by a helical flagellum. *Proceedings of the National Academy of Sciences*, **110** (2013), E338.

[89] Saleh, B. E. A. and Teich., M. C. *Fundamentals of Photonics*. John Wiley & Sons, Ltd (1991).

[90] Schlesener, F., Hanke, A., and Dietrich, S. Critical casimir forces in colloidal suspensions. *Journal of Statistical Physics*, **110** (2003), 981.

[91] Schuerle, S., et al. Synthetic and living micropropellers for convection-enhanced nanoparticle transport. *Science advances*, **5** (2019), eaav4803.

[92] Schwalm, R. *UV Coatings Basics, Recent Developments and New Applications*. Elsevier Science, 1st edn. (2006).

[93] Selimis, A., Mironov, V., and Farsari, M. Direct laser writing: Principles and materials for scaffold 3d printing. *Microelectronic Engineering*, **132** (2015), 83. Micro and Nanofabrication Breakthroughs for Electronics, MEMS and Life Sciences.

[94] Sitti, M. *Mobile Microrobotics*. MIT Press (2017).

[95] Solovev, A. A., Mei, Y., Bermúdez Ureña, E., Huang, G., and Schmidt, O. G. Catalytic microtubular jet engines self-propelled by accumulated gas bubbles. *Small*, **5** (2009), 1688.

[96] Spivey, E. C., Ritschdorff, E. T., Connell, J. L., McLennon, C. A., Schmidt, C. E., and Shear, J. B. Multiphoton lithography of unconstrained three-dimensional protein microstructures. *Advanced Functional Materials*, **23** (2013), 333.

[97] Stanton, M. M., Park, B.-W., Miguel-López, A., Ma, X., Sitti, M., and Sánchez, S. Biohybrid microtube swimmers driven by single captured bacteria. *Small*, **13** (2017), 1603679.

[98] Steager, E., Kim, C.-B., Patel, J., Bith, S., Naik, C., Reber, L., and Kim, M. J. Control of microfabricated structures powered by flagellated bacteria using phototaxis. *Applied Physics Letters*, **90** (2007), 263901.

[99] Steager, E. B., Sakar, M. S., Kim, D. H., Kumar, V., Pappas, G. J., and Kim, M. J. Electrokinetic and optical control of bacterial microrobots. *Journal of Micromechanics and Microengineering*, **21** (2011), 035001.

[100] Stoeckenius, W. and Rowen, R. A MORPHOLOGICAL STUDY OF HALOBACTERIUM HALOBIUM AND ITS LYSIS IN MEDIA OF LOW SALT CONCENTRATION . *Journal of Cell Biology*, **34** (1967), 365.

[101] Studer, K., Decker, C., Beck, E., and Schwalm, R. Overcoming oxygen inhibition in uv-curing of acrylate coatings by carbon dioxide inerting, part i. *Progress in Organic Coatings*, **48** (2003), 92.

[102] Studer, K., Decker, C., Beck, E., and Schwalm, R. Overcoming oxygen inhibition in uv-curing of acrylate coatings by carbon dioxide inerting: Part ii. *Progress in Organic Coatings*, **48** (2003), 101.

[103] Sun, H.-B., Maeda, M., Takada, K., Chon, J. W. M., Gu, M., and Kawata, S. Experimental investigation of single voxels for laser nanofabrication via two-photon photopolymerization. *Applied Physics Letters*, **83** (2003), 819.

[104] Sun, H.-B., Takada, K., and Kawata, S. Elastic force analysis of functional polymer submicron oscillators. *Applied Physics Letters*, **79** (2001), 3173.

[105] Taylor, B., Zhulin, I., and Johnson, M. Aerotaxis and other energy-sensing behavior in bacteria. *Annual Review of Microbiology*, **53** (1999), 103.

[106] Tipping, M. J., Steel, B. C., Delalez, N. J., Berry, R. M., and Armitage, J. P. Quantification of flagellar motor stator dynamics through in vivo proton-motive force control. *Molecular Microbiology*, **87** (2013), 338.

[107] Tottori, S., Zhang, L., Qiu, F., Krawczyk, K. K., Franco-Obregón, A., and Nelson, B. J. Magnetic helical micromachines: Fabrication, controlled swimming, and cargo transport. *Advanced Materials*, **24** (2012), 811.

[108] van der Horst, M. A. and Hellingwerf, K. J. Photoreceptor proteins, "star actors of modern times": A review of the functional dynamics in the structure of representative members of six different photoreceptor families. *Accounts of Chemical Research*, **37** (2004), 13.

[109] van der Horst, M. A., Key, J., and Hellingwerf, K. Photosensing in chemotrophic, non-phototrophic bacteria: let there be light sensing too. *Trends in Microbiology*, **15** (2007), 554.

[110] van Loosdrecht, M. C., Lyklema, J., Norde, W., and Zehnder, A. J. Influence of interfaces on microbial activity. *Microbiological Reviews*, **54** (1990), 75.

[111] Vigeant, M. A. and Ford, R. M. Interactions between motile escherichia coli and glass in media with various ionic strengths, as observed with a three-dimensional-tracking microscope. *Applied and Environmental Microbiology*, **63** (1990), 3474.

[112] Vigeant, M. A., Ford, R. M., Wagner, M., and Tamm, L. K. Reversible and irreversible adhesion of motile escherichia coli cells analyzed by total internal reflection aqueous fluorescence microscopy. *Applied and Environmental Microbiology*, **68** (2002), 2794.

[113] Vizsnyiczai, G., Frangipane, G., Maggi, C., Saglimbeni, F., Bianchi, S., and Di Leonardo, R. Light controlled 3d micromotors powered by bacteria. *Nature Communications*, **8** (2017), 15974.

[114] Vizsnyiczai, G., Kelemen, L., and Ormos, P. Holographic multi-focus 3d two-photon polymerization with real-time calculated holograms. *Opt. Express*, **22** (2014), 24217.

[115] Walter, J. M., Greenfield, D., Bustamante, C., and Liphardt, J. Light-powering escherichia coli with proteorhodopsin. *Proceedings of the National Academy of Sciences*, **104** (2007), 2408.

[116] Webre, D. J., Wolanin, P. M., and Stock, J. B. Bacterial chemotaxis. *Current Biology*, **13** (2003), R47.

[117] Williams, H. *Photophysical And Photochemical Factors Affecting Multi-photon Direct Laser Writing Using The Cross-linkable Epoxide Su-8*. Ph.D. thesis, University of Central Florida, Electronic Theses and Dissertations, 2004-2019. 2834. (2013).

[118] Wolfe, A. J., Conley, M. P., Kramer, T. J., and Berg, H. C. Reconstitution of signaling in bacterial chemotaxis. *Journal of Bacteriology*, **169** (1987), 1878.

[119] Xue, R., Ma, Q., Baker, M. A. B., and Bai, F. A delicate nanoscale motor made by nature-the bacterial flagellar motor. *Advanced Science (Weinheim, Baden-Wurttemberg, Germany)*, **2** (2015), 1500129.

[120] Yamazaki, A., Sendoh, M., Ishiyama, K., Ichi Arai, K., Kato, R., Nakano, M., and Fukunaga, H. Wireless micro swimming machine with magnetic thin film. *Journal of Magnetism and Magnetic Materials*, **272-276** (2004), E1741. Proceedings of the International Conference on Magnetism (ICM 2003).

[121] Yan, X., et al. Multifunctional biohybrid magnetite microrobots for imaging-guided therapy. *Science Robotics*, **2** (2017), eaaq1155.

[122] Young, E. and Alper, H. Synthetic biology: Tools to design, build, and optimize cellular processes. *Journal of Biomedicine & Biotechnology*, **2010** (2010), 130781.

[123] Zeeshan, M. A., et al. Hybrid helical magnetic microrobots obtained by 3d template-assisted electrodeposition. *Small*, **10** (2014), 1284.